Gas Flows and Feedback in Star forming Galaxies

Melaku S. Tafere

February 19 2018

A project submitted in partial fulfilment of the requirements for the degree M.Sc. in the Department of Astronomy, as part of the National Astrophysics and Space Science Programme
UNIVERSITY OF CAPE TOWN

Department of Astronomy
Supervisor: Dr. Petri Väisänen [1]
Cosupervisor: Dr. Kurt van der Heyden [2]

University of Cape Town

[1]South African Astronomical Observatory (SAAO)
[2]University of Cape Town (UCT)

The copyright of this thesis vests in the author. No quotation from it or information derived from it is to be published without full acknowledgement of the source. The thesis is to be used for private study or non-commercial research purposes only.

Published by the University of Cape Town (UCT) in terms of the non-exclusive license granted to UCT by the author.

University of Cape Town

Abstract

In this MSc thesis, I investigated the kinematics of H emission from the hot ionized and NaD absorption from cool neutral gas in a sample of 40 nearby Luminous Infrared Galaxies (LIRGs: $LIR \geq 10^{11} L\odot$) from Supernovae and starbursts in the infrared, SUNBIRD survey imaged with the Southern African Large Telescope (SALT). This project can be seen in two major areas. The first is analyzing the emission and absorption spectra, in this case from the hot ionized gas and cool gas respectively.

Two routines were used for the profile fitting, to get the centroid wavelength of both the emission and absorption lines; Gaussian and Gaussian-Hermite functions were used. The fitting result provides an indication of the origin of an outflowing gas; nuclear or disk driven?.

Secondly, I plotted and compared the velocities of hot ionized and cool neutral gas. Three different methods were used to estimate the systemic velocity V sys for the accurate estimationof outflowing velocity. For instance, an outflowing NaD upto 380 kms 1 and inflowing gas up to -100 kms 1 relative to H is seen at the optical nucleus of the NGC6240[PA=45] and NGC1204[PA=253] galaxies respectively.

I tested if there was a relation between star formation rate (SFR) and an outflowing gas and also whether the inflowing gas triggering new nuclear SF. I find the gas of two of our targets escaping the potential well of the host galaxy. There was also an expectation that the out flowing velocity would correlate with SFR, unfortunately I do not see any correlation, though it needs further investigation of all offset velocities of the gas with respect to stellar absorption lines and it also requires detail analysis of the of projection or orientation effect on the galaxy.

Melaku S. Tafere

Acknowledgements

First of all, I would like to thank God for helping me to get the chance to study at the University of Capetown. I would like to express my deepest gratitude to my supervisor, Dr Petri Väisänen, for his support and guidance throughout the research. Mostly, his patience, kindness, friendly nature and especially his encouragement when things got worse and though. I also thank Mina Petri's wife for her motherly love and treatment during stress time.
I would like to express my appreciation to my UCT supervisor Dr Kurt van der Heyden, he helped me a lot for two years of my stay. I'm thankful for his instant response to all my queries from course work to the end of my thesis.

Rajin Ramphul Petri's PhD student, my good friend and mentor, words are not enough to thank you! He has helped me a lot from the start of my thesis to the end and imparted me python and Latex. In addition to academic, I have learned so many things from you.You mean a lot to me! Can I have more lessons on IRAF?

Dr Moses Mogotsi, I'm thankful for your patience in correcting my English and teaching me how to write a good thesis. Without your consistent help and patient guidance, I could never accomplish my thesis. He always has time for me! I'm so lucky and blessed to have you as a mentor during my study.

Dr Amare Abebe, I always remember you when I see myself as part of NASSP. Heartfelt thank for providing information about NASSP scholarship, for writing recommendation letter and especially, suggesting the right supervisor.

Desalegn Tekle for your encouragement and writing a recommendation letter for the scholarship. I also thank Dr Getnet Feleke for your good friendship and sharing experience about NASSP. All Entoto comunity, Yikdem, Tsegaye, Nigist, Tade, Eshetu and Seblu you guys are special!

Thank you to the UCT Astronomy Department, NASSP Masters 2016 group, especially Temba

thank you for your help and best friendship since 2016 and for your help during the course work. Wathella and Abubakir thanks for your true friendship; with you guys I feel home.

I am eternally grateful to Tezera Dagnew, Zeray G|Egziabher, Tilahun Biyadgie, Abere Mesfin, Getnet Worku, Birtukan Sisay, Alebachew Teka, Animut Biyadgie and the rest of my families, thank you for your financial support.

I am also very thankful to all SAAO community, especially finance department Linda and Valensia for your instant reponse when I had bank issues.
Finally, I would like to acknowledge NASSP for funding my study and the financial support from the SAAO.

Declaration

I, Melaku Tafere, know the meaning of plagiarism and declare that all of the work in the thesis is my own work, the sources I have used have been indicated and referred.

Dedicated to my families and friends

List of Abbreviations

AGN	Active Galactic Nuclei
HST	Hubble Space Telescope
IRAS	Infrared Astronomical Satellite
IGM	Inter Galactic Medium
ISM	Interstellar Medium
LIRG	Luminous Infrared Galaxies
LF	Luminosity Function
NED	NASA/IPAC Extragalactic Database
RBGS	Revised Bright Galaxy Sample
SFR	Star Formation Rate
sSFR	specific Star Formation Rate
SUNBIRD	SUperNovae and starBursts in the InfraReD
ULIRG	Ultraluminous Infrared Galaxy

Contents

List of Figures

List of Tables

Chapter 1

Introduction

1.1 Overview

Understanding the formation and evolution of galaxies requires an understanding of their composition of dust, gas, and stars (Santini et al., 2014). The authors also added dust is composed of metals which will be expelled to the interstellar medium (ISM) through stellar winds and supernovae explosions. Interstellar dust can be used to regulate the star formation, because hydrogen ionizing photons which make up HII is controlled by dust properties as Kimm and Cen (2014). The Hubble (1926) classification of galaxies shows an increase in the gas, dust and star formation from early-type elliptical (with no gas, dust and also no young stars) to star forming regions to late-type spirals (Sc) and irregular galaxies. Elliptical galaxies are gas poor and composed of old and low mass stars, unlike spiral galaxies, which have gas and dust dominated disks that enable them to undergo further star formation.

Stars are born from dense, cold gas either in disks or in shock compressed gas (in mergers). Formation of new stars causes the properties of galaxies to evolve with time, and thus they determine many of the properties that galaxies are presently observed to have. The formation of massive stars is closely associated with the formation of clusters and associations, (eg. Larsen 2010, Mas-Hesse et al. 2008).

This project concentrates on gas inflow/outflows and the interplay and feedback due to star formation (SF) and nuclear activity in interactions. The intention of this project is also mainly the to study the origin and location of the outflowing gas(nuclear or disk dr) and its connection to star formation rate of the galaxies.

1.2 Starburst Galaxies

As galaxies interact with each other, a large amount of gas flows to their central regions which can lead to increased intense star formation called a starburst Weedman et al. (1981). Starbursts show rapid star formation that can be induced by gravitational interaction or collision with another galaxy. Newly formed massive stars in the starburst galaxy heat up gas in the interstellar medium and create strong and narrow emission lines, (eg. Messier 82, Veilleux et al. 2005).

Starburst galaxies are key to studying star formation and its effect on interstellar medium (ISM). Stellar winds from the newly formed stars which followed by supernovae; heating up the gas in the disk and driving it into the ISM. Starburst galaxies combine large central gas concentrations and high ionizing radiation fields; i.e bright molecular, neutral and ionized gas emission lines. For instance Figure 1.1 shows M82, a typical nearby starburst galaxy with intense star formation. In a starburst, galactic scale wind (also called superwind) have been detected up to distances of 10 kpc above the plane of the galaxy Lehnert (1999). These winds begin when the star formation is high enough to create a region with hot gas. This hot gas has much higher pressure than the surrounding ISM, pressure which enables it to drive the ISM perpendicular to the disk of the host galaxy (i.e. along the minor axis), for more detail see (Veilleux et al., 2005).

1.3 Active Galactic Nuclei (AGNs)

It is believed that AGN have a great influence on the evolution of their host galaxies through powerful winds and outflows. Active Galactic Nuclei are highly energetic and luminous objects at the centers of galaxies. AGNs are thought to radiate due to accretion onto a super-massive black hole (Ishibashi and Fabian, 2012). Studies show that once the central black hole reaches a certain critical mass, the radiation or feedback begins to expel most of the gas out of the host galaxy (Zubovas and King, 2014). This leads to the quenching of star formation. On the other hand, Fabian (2012) reported as the radiation pushes the “gas out of the galaxy, then the gas may end up trapped in the halo”. The rotation and compression of cold and dense molecular gas during the ejection process triggers star formation. Black holes consume the gas and dust which surrounds them forming structures known as an accretion disk. When these gas and dust fall into the black hole, it causes the accretion disk starts to heat up due to gravitational and frictional forces leads to infrared emission.

Figure 1.1: A famous starburst galaxy, M82, showing a strong outflow in the Hα (magenta) from the central source in the nucleus along the minor axis. Image is taken from Veilleux et al. (2005).

1.4 The Infrared Astronomy Satellite Galaxies

The significance of the study of star forming galaxies in the infrared region of the spectrum has been studied over the decades since the discovery of IRAS galaxies. This region is known in uncovering gas and dust. Infrared Astronomy Satellite Galaxies (IRAS) provided an unbiased all-sky survey at mid and far-infrared wavelengths that provided us with the infrared emission properties of galaxies in the local universe (Neugebauer et al., 1984). After the launch of IRAS, the awareness of galaxy evolution dramatically increased. The result of observation of IR galaxies in four bands centered at 12, 25, 60, and 100μm helps for the diskovery of many extragalactic objects which were not cataloged in the optical but emit most of their bolometric luminosity in the IR (Soifer et al., 1987). The IRAS bright galaxy (IRASBG) survey which contains a complete sample of 324 far- infrared emitting extragalactic objects detected at 60μm in the all-sky IRAS survey Soifer et al. (1987) and they found far-infrared emission as a dominant luminosity component in the local universe which is emitted by a thermal emission that was absorbed by dust. Figure 1.2 shows the comparison of luminosity function of IRAS Revised Bright galaxy Samples (RBGS) with normal optically selected galaxies Sanders and Ishida (2004). The RBGS show excess tail at the bright end above infrared luminosity $10^{11}L_{\odot}$ which, best described by a power-law of Schechter (1976).

1.5 Luminous Infrared Galaxies

Galaxies with infrared luminosities $10^{11}L_{\odot}$ - $10^{11.99}L_{\odot}$, which emit most of their energy in the infrared region, and are known as luminous infrared galaxies (LIRGs), Ultra-luminous infrared galaxies (ULIRGs have $10^{12}L_{\odot} \leq L_{IR} < 10^{13}L_{\odot}$ and Hyper luminous infrared galaxies (HyLIRG, L_{IR} >$10^{13}L_{\odot}$. LIRGs and ULIRGs are powered by intense star formation, AGN, or combination of both processes.They have a large role in the star formation history of the Universe. Nearby LIRGs are typically “merging galaxies intermediate mass ellipticals or spiral galaxies undergoing mergers and interactions, and have high star formation” (Wang et al., 2006).

LIRGs are good laboratories to test the star formation history in the universe. They might appear faint at optical wavelengths because they emit most of their energy in the infrared portion of the spectrum. The reason these galaxies are so luminous is believed to be due to their merging or interacting properties. The gas-rich spirals in the interactions produce very high star formation, sometimes called starbursts.
These mergers may drive gas to the central black hole. The investigation of LIRGs at different stages of interactions shows star formation, AGN activity, as well as morphological evolution of these galaxies. eg. (Lonsdale et al., 1984). Prototypical LIRGs formed by pairs of colliding gas-rich spiral galaxies are believed to transform within a few hundred Myr to a very

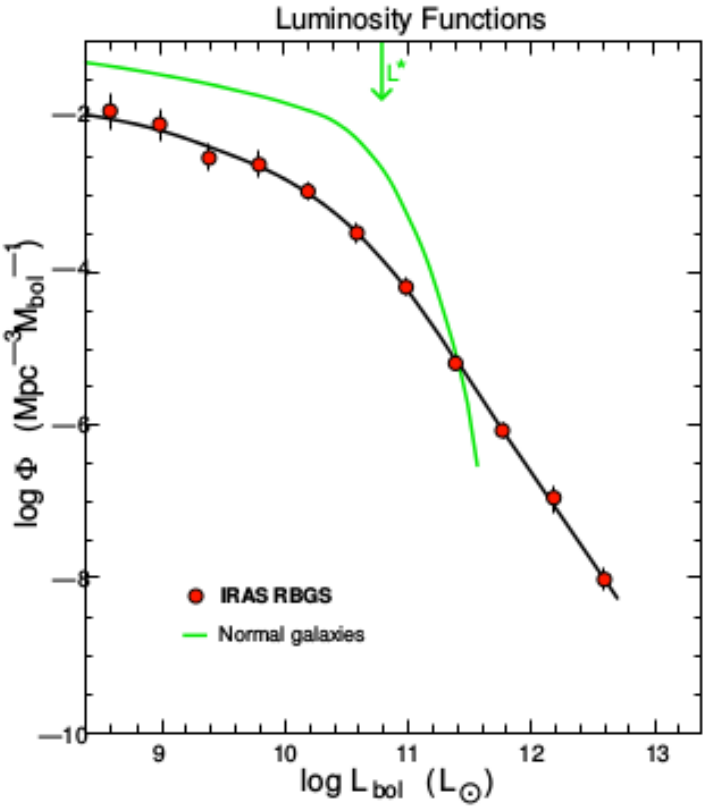

Figure 1.2: The comparison between luminosity function (LF) of normal galaxies and IRAS Revised Bright galaxy Samples (RBGS). The thick the solid line and filled circles represent the local LF of galaxies as determined in the IRAS RBGS Sanders et al. (2003) and the thin line indicates normal local galaxies

bright IR merging galaxy as a result of the strong dynamical interactions. According to Pizagno et al. (2008) after passing through several stages these merging galaxies change into early-type elliptical galaxies. Figure 1.3 shows the evolutionary process of merging galaxies.

Several have studies shown that LIRGs are mergers of gas-rich disk galaxies. The IR luminosity is directly correlated to strong interaction or mergers Veilleux et al. (1995). Wang et al. (2006) studied the morphology and star formation properties of 159 local LIRGs and they classified 77($\sim$ 48%) as interacting /merging galaxies, 19(12%) as isolated compact, and the rest 63(40%) as normal spiral galaxies. They finally concluded that most local LIRGs are either major mergers or "massive disk galaxies" undergoing star formation bursts, which are controlled by bars.

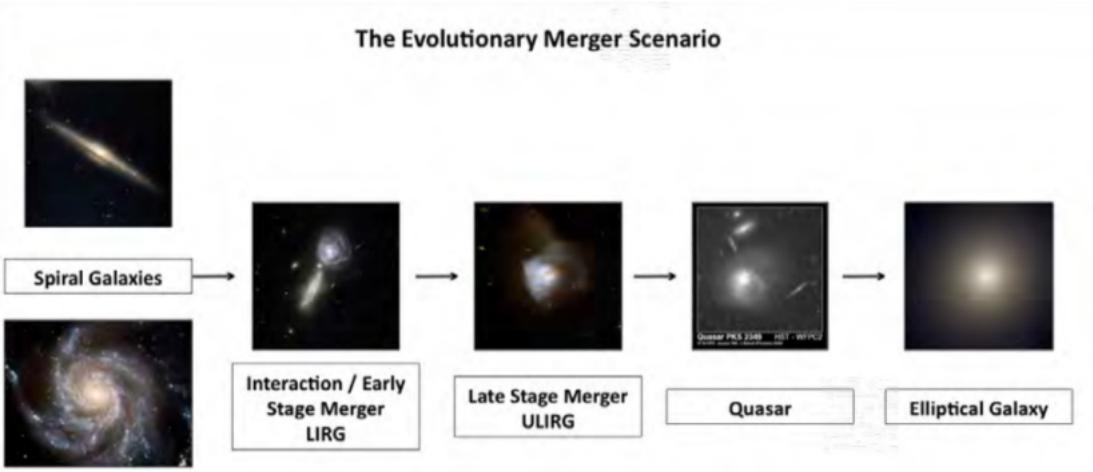

Figure 1.3: Evolutionary merger scenario proposed by Sanders and Mirabel (1996).The merging of two gas rich spiral galaxies forms a luminous infrared galaxy that evolves to a ULRG,then to Quasar and finally to Elliptical galaxy.

1.6 Star formation rates (SFRs)

SFR is the rate at which the molecular gas changes to stars which depends on the density of the gas as Gao and Solomon (2004). Young (age $\leq 10^8$ yr) massive stars ($\sim 8M_{\odot}$), which are the source of Ultra-Violet (UV) photons, plays significant role to estimate SFR. The most direct method to measure the SFR is the UV continuum from young, massive stars. The IR luminosity of a star-burst galaxy is due to UV emission these stars absorbed by dust and re-emitted in the IR region of the spectrum. since strongly star-forming galaxies are often dusty, and uv light is absorbed, it is difficult to use the observed uv continuum. In contrast, MIR and FIR are easier to use in cases like this, since it is not extinct, while it (more or less) results from that same UV radiation. The L_{IR} values I used in this thesis are retrived from RBGS survey of a paper by Sanders et al. (2003) , see in Section 1.4 . Total IR flux, from mid infrared to far infrared (8-1000μm) is calculated using the formula given by Sanders and Mirabel (1996).

$$F_{\rm IR} = 1.8 \times 10^{-14}\{13.48f_{12} + 5.16f_{25} + 2.58f_{60} + f_{100}\} \tag{1.1}$$

where f_{12}, f_{25}, f_{60} and f_{100} are flux densities centered at IRAS bands 12, 25, 60 and 100μm. An attempt was made to compare the newly calculated D_L with the existing one, there was no difference, no wonder the reshift was the same. After evaluating the luminosity distance D_L from redshift(z) following (Bennett et al., 2014), the infrared luminosity can be calculated as:

$$L_{\rm IR} = 4\pi {D_{\rm L}}^2 F_{\rm IR}[L_{\odot}] \tag{1.2}$$

Once the L_{IR} calculated, SFR can be estimated using a formula given by Kennicutt (1998)

$$SFR(M_{\odot}yr^{-1}) = 4.5 \times 10^{-44} \left[\frac{L_{\rm IR}}{ergs}\right] \tag{1.3}$$

Using conversion factor $L_{\odot} = 3.85 \times 10^{-33} \frac{erg}{s}$, equation 1.3 can be written as

$$SFR(M_{\odot}yr^{-1}) = 1.7 \times 10^{-10} L_{\rm IR}[L_{\odot}] \tag{1.4}$$

1.7 Galactic Winds

What are they? What is their socrce of energy? Are they nuclear or disk driven? Galactic winds are ubiquitous in most rapidly star forming galaxies in both the local and high redshift universe (Heckman, 2000, Veilleux et al., 2005). They are believed to play central role in the evolution of galaxies by ejecting and depositing energy and matter into the in tergalactic medium (IGM). It then feeds back(affect) the host galaxy, see Section 1.9 for more detail.

Galactic winds affect the evolution of galaxies and the inter galactic medium (IGM) via gas accretion and star formation (Heckman and Thompson, 2017). The author also added galactic winds which are powered by the momentum and energy injected by massive stars in the form of supernovae, stellar winds, and radiation which also may help to regulate star formation within the galaxies. In other words galactic outflow is a combination of the momentum and kinetic energy supplied by the winds of massive stars and the ejecta of core collapse supernovae. Line and continuum emission from hot gas (plasma) have played a major role in identifying Galactic winds (GWs). Winds are driven by the heating of the interstellar medium (ISM) by supernovae (SNe) or by the radiation pressure from stars. If the galactic wind has blown all of the gas out of the galaxy, star formation will cease. In galaxies with high rates of star formation, galactic winds also play a role by driving gas and dust out of the galaxy disk.

Studies of Na I D interstellar absorption lines ($\lambda 5890, \lambda 5896$) have shown that galactic winds occur in most galaxies with high infrared luminosities (Heckman, 2000, Rupke and Veilleux, 2005). According to Croston et al. (2008), outflows heat and enrich intergalactic medium with metals. Many key observables need gas flows in models explaining them in the cosmological build-up of the galaxy population seen today Hopkins et al. (2012).

1.8 Interstellar Medium

Interstellar Medium (ISM) is everything found between stars, such as dust (solid particles), radiation and gas (ionized, neutral and molecular). Those heavy elements also depend on the gas content of galaxies. The star formation rate (the rate at which gas changes to stars) depends on the gas content. Most of the interstellar medium is composed of interstellar gas, mostly Hydrogen, while Helium is the second most abundant element.

The interstellar gas has two categories: cold clouds of neutral atomic or molecular hydrogen is the place where the new stars are born due to gravitational collapse, and hot ionized hydrogen near hot young stars (O and B-type stars). Ultraviolet light from these young hot stars ionizes the surrounding hydrogen gas i.e the electrons recombine with the protons this is known as an HII region, they emit light which can be detectable in visible spectrum most notably in the Balmer series of Hydrogen, e.g. the Hα line at a wavelength of 6563 angstroms.

1.9 Feedback Process

Feedback is a process which regulates the growth of galaxies. Star formation (SF) feeds energy and other materials back into the ISM. Feedback also controls the galactic star formation rate (SFR). Feedback can also be seen as the impact of young massive stars to their interstellar medium (ISM), galactic halo, or to the general intergalactic medium (IGM) (Martin, 2003). It can be seen when massive stars heat the surrounding ISM and impact the surroundings. Feedback from supernovae (SNe) and supermassive black holes (BHs) plays a significant role in star formation rates (SFRs), shaping the properties of galaxies and formation of massive galaxies McCarthy et al. (2010). Feedback and star formation are not separate entities, instead they show a cyclic process. Star formation will generate certain properties of feedback and this feedback will generate an outflow or turbulence in the stellar medium and in the intergalactic medium (IGM) which in turn influences star formation. Figure 1.4 shows this cyclic process.

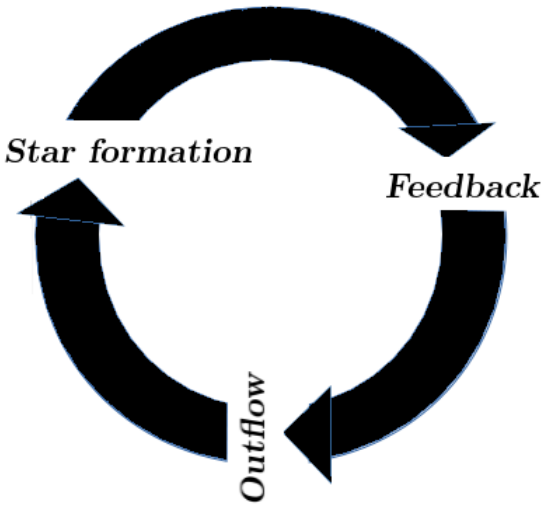

Figure 1.4: A cyclic diagram shows the relation between star formation, feedback and outflow or turbulence. The Figure is based on Agertz and Kravtsov (2015).

1.9.1 Starburst/Active galactic nuclei Feedback

Active galactic nuclei (AGN) at the centers of galaxies have a significant effect on the evolution of galaxies. AGN is thought to regulate the growth of supermassive black holes (SMBHs). AGN wind from the pressure inside an accretion disk, which is accelerated by radiation pressure, shock against the surrounding ISM and drives an outflow in the AGN of the host galaxy (Zubovas and King, 2014). These authors pointed out, that at the center close to the central black hole the shocked wind cools rapidly via Compton effect and the velocity of the gas starts to slow and finally fall back. This will happen till the black hole reaches its critical mass, $M_\sigma \simeq 3.67 * 10^8 \sigma_{200}^4 M_\odot$. Once it reaches this mass the wind is capable of removing the ISM and start to power the outflow. Figure 1.5 shows the impact of AGN wind to the surrounding ISM.

1.9.2 Supernova Feedback

When the core of young massive stars collapse, tremendous amounts of energy and momentum are injected into the ISM. Supernova feedback is another feedback process which plays a significant role in galaxy evolution. It is considered to be an influential element which gives *negative feedback* through star formation in disk galaxies. i.e supernova explosions (SNe), can suppress SF by evaporating dense, star-forming clouds, by turbulence and powerful outflows

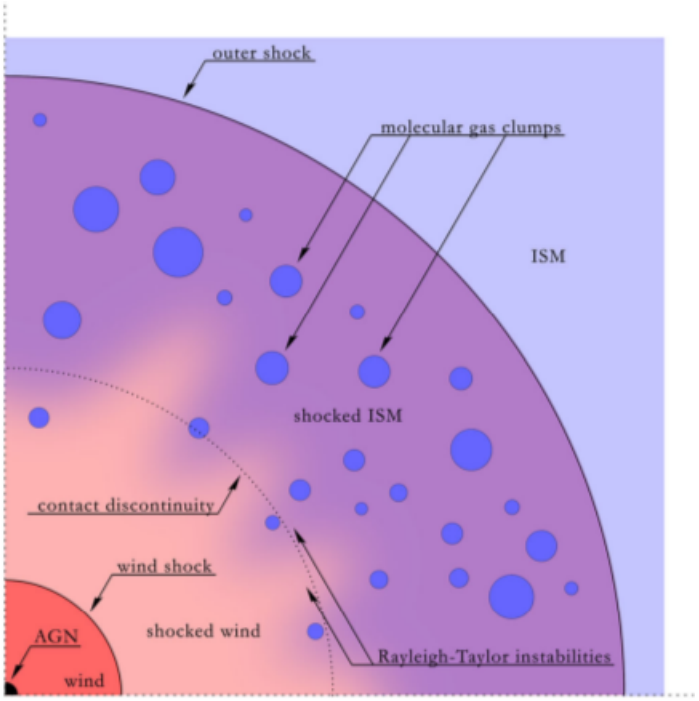

Figure 1.5: As AGN drives a powerful wind from its accretion disk which shock outside the Compton cooling radius. The shocked wind sweeps up and drives an outer shock into the hot ISM. Image is taken from Zubovas and King (2014).

that eject gas. SN feedback controls how much gas is able to condense into galaxies and form stars. As Booth and Schaye (2013) also reported SNe are effective in suppressing SF in low-mass ($m_{200} < 10^{12} M_{\odot}$) than high mass objects.

1.9.3 Stellar wind Feedback

Stellar wind feedback is another feedback mechanism that affects the interstellar medium and plays an central role in the formation of galaxies. Stellar winds are fast moving flowing materials (heavy metals) ejected from stars, mainly from hot young massive stars. The strength of the wind depends on the mass of the star; massive stars can produce stronger winds.

1.10 Objectives

The aim of this project is to analyze both the emission and absorption spectra of Star forming galaxies (SF). Ultimately the goal is to calculate the masses and energies involved in the gas ouflows and/or inflows process. But in this thesis I will be adressing the origin of the outflow and what drives the gas flows:

- Nuclear or disk driven?
- How are the outflows connected to SFR?
- Can the outflows escape the gravitational wells and enrich the intergalactic medium?

The outline of the thesis is as follows. In Chapter 2 I describe our sample which is from SUNBIRD survey, in Chapter 3 I discuss how I perform the profile fitting of emission and absorption, and calculate the kinematics of our targets. I present our main results in Chapter 4 and finish with conclusions in Chapter 5. The appendices images used to checked the results in Chapter 3 and support the diskussion in Chapter 4. Throughout the thesis I assume a spatially flat cosmology following Väisänen et al. (2008a) with: $H_0 = 73$ km s^{-1} Mpc $^{-1}$, $\Omega_\Lambda = 1$ and Ω_m=0.27.

Chapter 2

The Sample

The ongoing survey "SUperNovae and starBursts in the InfraReD" (SUNBIRD) studies nearby LIRGs with IR luminosities $10^{11}L_{\odot} \leq L_{IR} < 10^{12}L_{\odot}$. Väisänen et al. (2014) and Kankare et al. (2012) used adaptive optics, AO (used to correct blurring of light due to atmospheric perturbation), and NIR imaging with VLT and Gemini to search dust obscured core-collapse SNe and study the LIRG hosts of these SNe. The instruments delivered images with a spatial resolution perfectly complementing existing Hubble Space Telescope (HST) optical data. A sample of 40 LIRGs were selected from SUNBIRD. The SUNBIRD are IRAS galaxies from the RBGS (Sanders et al., 2003), the targets are listed on Table 2.1.

To study the evolution of the host-galaxies further, the targets were then observed with optical spectroscopy at Southern African Large Telescope, SALT, using the RSS instrument. The data were acquired over a span of 3 years, from late 2011 to 2014. The PG1800 grating was used, a medium resolution Volume Phase Holographic (VPH) grating at R ∼3000. The rest frame wavelength coverage was rest frame region of 5600 - 6930$\mathring{A}$ and the physical size of the slit during observations was $1''$ width and $8'$ long.

The targets are at various stages of interactions and mergers of gas-rich spirals (Sanders et al., 2009). These galaxies are in the local universe at distances ranging from $30 \leq D_L \leq 205$ Mpc. I estimated the luminosity distance D_L from the redshift calculated using the observations. The exposure times range from 900s to 3000.6s, though the majority of our targets have exposure time of 1800s. Most of the photometry of our sample of galaxies is studied and presented by Randriamanakoto et al. (2013).

Our SALT spectra always show very strong Hα emission from the warm ionized gas, sometimes extending far outside the visible galaxy with velocities indicating expanding bubbles. To estimate SFR, Hβ and the higher order Balmer emission lines could be used but they are weak

and more sensitive to stellar absorption than Hα. There is also a strong neutral Na D absorption due to the cool interstellar material which is often blue or red shifted from the galaxy's systemic velocity, indicating cool gas outflows and/or inflows.

The data reduction was done by Vaisanen, Tekola and Ramphul (priv. communication). For the reduction and calibration, they developed pipeline using Python. The standard reduction procedures can be summarised as: bias correction, flat fielding, cosmic ray removal, wavelength calibration, background subtraction, spectrum extraction and flux calibration was done. Figure 2.1 shows the process for data reduction procedure used by Ramphul(priv. communication) which is also used in this thesis.

Table 2.1 lists the basic properties of the galaxies in our sample. Figure 2.2 shows the distri-

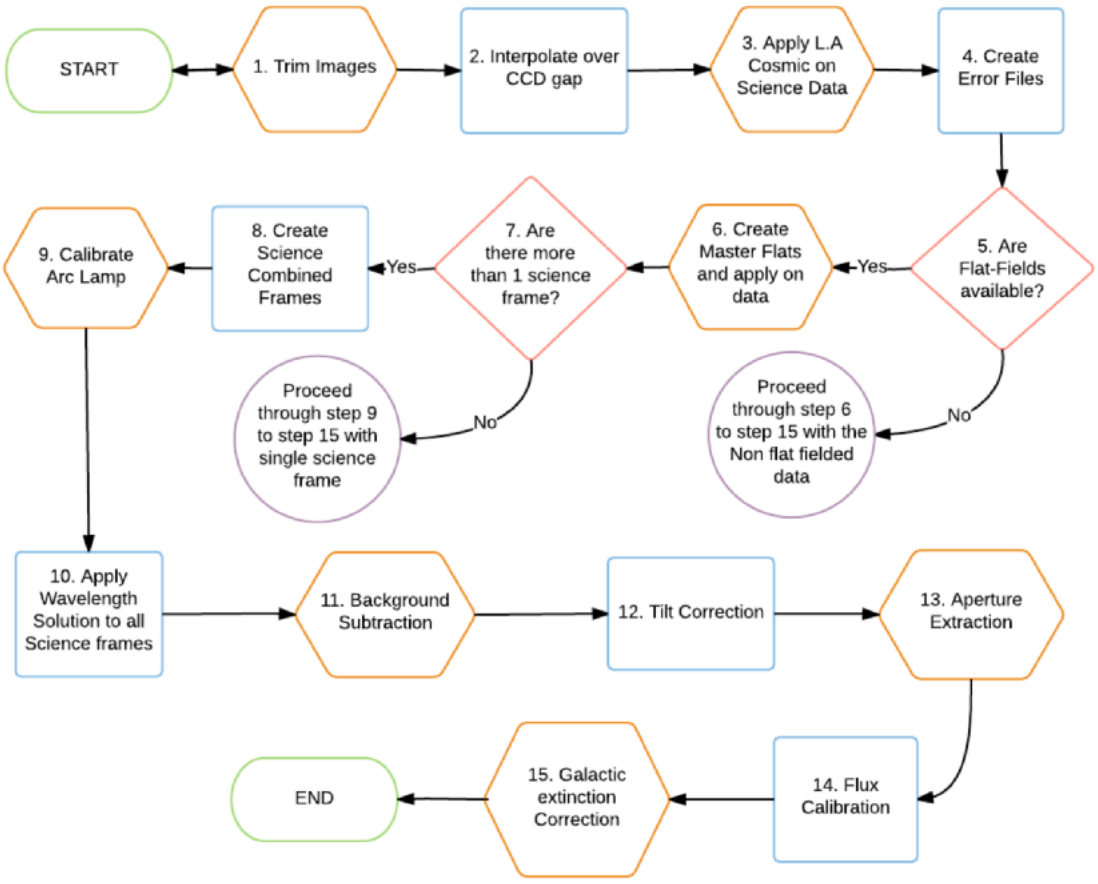

Figure 2.1: showing the procedure of the data reduction process, taken from Ramphul (priv. communication)

bution of our targets in IRASBGs Sanders et al. (2003) for galaxies up to z $\sim$ 0.05 as they are listted in Table 2.1.

Some of our targets were observed two or three times in different position angles (position of

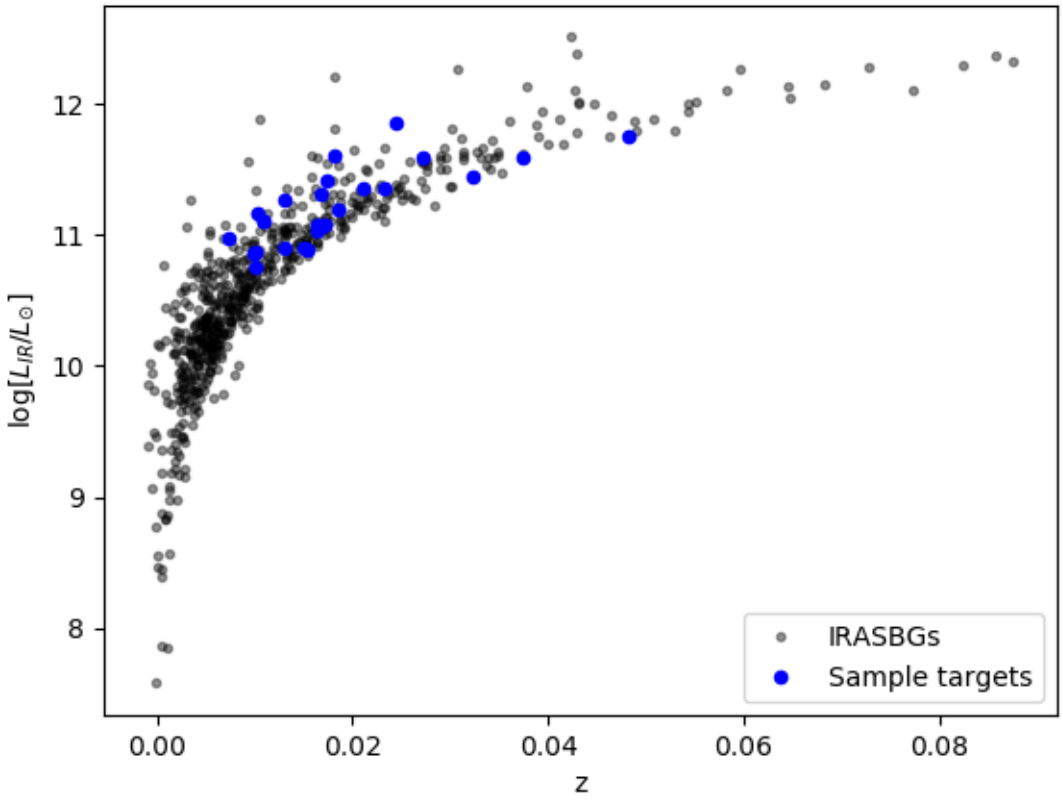

Figure 2.2: Distribution of our targets from the SUNBIRD sample shown in blue circles with the IRASBGs (Sanders et al., 2003) shown in black points.

the slit relative to North) to get sufficient information about the targets. Table 2.1 shows list of our targets, coordinates of observations, number of observations in position angles and their type, see the categories in Section 3.3.

Table 2.1 arranged based on L_{IR} which are taken from Sanders et al. (2003). It contains 40 galaxies from our sample. There are repeated obeservation up to three in different slit position. I used the position angle (PA) in the bracket to idetify the repeated galaxies. The coordinates are taken from NASA/IPAC Extragalactic Database (NED). Most of the redshifts are taken from NED and I estimated few of them. Those I estimated are indicated in bold on Table 2.1. The luminosity distance D_L was calculated from the redshift.
The target's type is also taken from Simbad and identified as;
G (Galaxy), HIIG (HIIgalaxy), GIG (Galaxy in Group of Galaxies), EmG (Emission line Galaxy), GIC (Galaxy in clusters), Sy2 (Syfert2), IG (Interacting Galaxy) and Gpair (Galaxy

pair).

Table 2.1: Properties of the sample

Object Name	RA (J2000)	DEC (J2000)	z	PA	LIR	DL	Object Type
(1)	(2)	(3)	(4)	(5)	(6)	(7)	(8)
ESO428-G023	07h22m09.4s	−29d14m08s	0.010	261	10.76	85	G
ESO440-IG058(PA=245)	12h06m51.7s	−31d56m46s	0.023	245.5	10.79	95	Gpair
ESO491-G020	07h09m48.1s	−27d34m15s	0.010	257	10.86	10	GIG
NGC4433	12h27m38.6s	−08d16m42s	0.010	187.7	10.87	5	EmG
NGC1204(PA=173)	03h04m39.9s	−12d20m29s	0.015	73	10.88	70	Sy2
NGC1204(PA=253)	03h04m39.9s	−12d20m29s	0.015	253	10.88	70	Sy2
MCG-02-33-098	13h02m20.4s	−15d46m00s	0.016	246	10.89	65	G
NGC1819(PA=125)	05h11m46.1s	+05d12m02s	0.015	125	10.9	120	GIC
ESO154-G010	02h45m08.7s	-55d44m26s	0.0185	24.5	-	30	G
NGC1819 (PA=225)	05h11m46.1s	+05d12m02s	0.015	225	10.9	120	GIC
NGC3508	11h02m59.7s	−16d17m22s	0.013	14.5	10.90	20	EmG
NGC6000	15h49m49.5s	−29d23m13s	0.010	174	10.97	155	AGN
ESO550-IG025(PA=242)	04h21m20.1s	−18d48m57s	0.032	242	11.03	55	IG
ESO319-G022	11h27m54.1s	−41d36m52s	0.016	295	11.04	85	G
ESO264-G057	10h59m01.8s	−43d26m26s	0.017	96.6	11.08	105	G
IC4280	13h32m53.4s	-24d12m26s	0.016	29	11.08	60	G
ESO320-G030(PA=90)	11h53m11.7s	−39d07m49s	0.0102	90	11.10	145	HIIG
ESO320-G030(PA=135)	11h53m11.7s	−39d07m49s	0.0102	135	11.10	145	HIIG
NGC2369 (PA=250)	07h16m37.7s	-62d20m37s	0.011	250	11.10	5	GIG
NGC2369(PA=350)	07h16m37.7s	-62d20m37s	0.011	350	11.10	5	GIG
ESO221-IG010	13h50m56.9s	−49d03m20s	0.010	150	11.17	20	GIG
ESO267-G030	12h14m12.9s	−47d13m42s	0.018	135	11.19	110	G
ESO440-IG058(PA=57.8)	12h06m51.9s	−31d56m58s	0.023	57.8	11.22	70	Gpair
ESO550-IG025 (PA=219)	04h21m20.0s	−18d48m39s	0.034	219	11.24	155	IG
CGCG049-057(PA=199)	15h13m13.1s	+07d13m3	0.013	199	11.27	20	G
CGCG049-057(PA=0)	15h13m13.1s	+07d13m3	0.013	0	11.27	20	G
NGC3110(PA=43.7)	10h04m02.1s	−06d28m29s	0.017	43.7	11.31	145	HIIG
NGC3110 (PA=111)	10h04m02.1s	−06d28m29s	0.017	111	11.31	145	HIIG
NGC3110(PA=185)	10h04m02.1s	−06d28m29s	0.017	185	11.31	145	HIIG
ESO264-G036	10h43m07.7s	−46d12m45s	0.021	294	11.35	130	GIG
IRASF17138-1017	17h16m35.8s	-10d20m39s	0.017	0	11.42	0	-
IRASF06076-2139	06h09m45.8s	-21d40m24s	0.037	61	11.59	25	-
IRAS12116-5615	12h14m22.1s	-56d32m33s	0.027	231	11.59	150	G
IRASF01364-1042	01h38m52.9s	-10d27m11s	0.048	42	11.76	35	-
IRASF08520-6850(PA=50)	08h52m29.9s	-69d01m58s	0.045	50	11.76	75	-
IRASF08520-6850(PA=108)	08h52m29.9s	-69d01m58s	0.045	108	11.76	75	-
IRASF18293-3413(PA=55)	18h32m41.1s	-34d11m27s	0.018	55	11.81	120	Gpair
IRAS18293-3413(PA=128)	18h32m41.1s	-34d11m27s	0.0182	128	11.81	120	Gpair
NGC6240 (PA=45)	16h52m58.9s	+02d24m03s	0.0245	45	11.85	25	Sy2
NGC6240(PA=90)	16h52m58.9s	+02d24m03s	0.0245	90	11.85	25	Sy2

Note. Col(4): redshift, Col(5): slit position, Col(6): bolometric IR luminosity($\log(L_{IR}/L_{\odot})$), Col(7) luminosity distance (D_L)

Chapter 3

Data analysis

3.1 Fitting Hα emission line profiles

To get the centroid wavelength of the three emission lines NII [λ6548 & λ6583] and Hα[λ6563], two python packages with two corresponding functions were used. A Gaussian function was fitted using a Levenberg-Marquardt fitting (LMfit) routine in Python/Scipy and the Gauss-Hermite function fitted using a nonlinear least squares kmpfit package from the Kapteyn Python module (mainly for data with huge wings or skewed distribution), see Equation 3.1.

Following Van Eymeren et al. (2010), I fitted line profiles. The latter function is also an ideal to fit asymmetric profiles. Thus, I have used this function to fit some of our asymmetric line profiles since most of our targets are asymmetric. The region i.e the wavelength range used for the fit containing emission lines NII [λ6548 & λ6583] and Hα was isolated, eg. see the integrated spectra of one of our target IRAS18293-3413 on Figure 3.1. Since our window (of selected region) depends on the size of continuum and redshift change, it varies object to object. The resaon for having a varing window is due too short continuum, eg. IRAS12116-5615, NGC6240 are some of them.

Depending on the spectra of target the width of the window varies from minimum λ6550 to maximum λ6934. A first order polynomial was fitted to the continuum of each spectrum by taking the lower and upper limits of the selected regions and then subtracted. Once the continuum fitted, I used constraints Flux [N II]λ6583 /3=Flux [N II]λ6548 by following Schnorr-Müller et al. (2014), also their relative distance was fixed. I fitted all the three emission lines simultaneously both for Gaussian and Gauss-Hermite function cases, see Figure 3.2.

$$f(x) = Ae^{-\frac{g^2}{2}}\left[1 + h_3\left(-\sqrt{3}g + \frac{2}{\sqrt{3}}g^3\right) + h_4\left(\frac{\sqrt{6}}{4} - \sqrt{6}g^2 + \frac{\sqrt{6}}{3}g^4\right)\right] \tag{3.1}$$

where

$$g = \left(\frac{x - x_c}{\sigma} \right) \tag{3.2}$$

where A is the amplitude, x_c center and σ is the width. Equation 3.1 is a pure Gaussian when h_3=h_4=0.

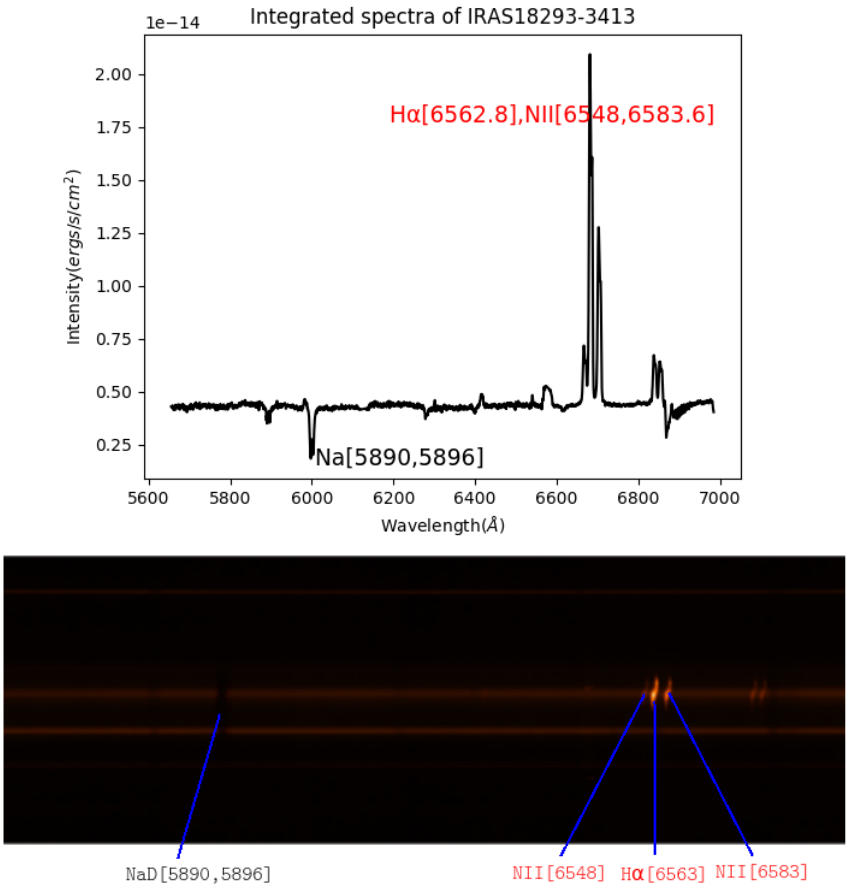

Figure 3.1: The upper panel shows the integrated spectra which contains Na D doublets (shown in strong absorption lines to the left) from the cool neutral gas and Hα (shown in strong emission lines to the right) from hot ionized gas. The lower panel shows the 2D spectral image of IRAS18293-3413. Na D shown in black doublets (left) where as Hα and NII[6548, 6583.6] (right) shown as bright emission lines

3.2 Fitting Na D absorption line profiles

The same approach as Hα emission line fitting has been used to select the region Na I D absorption doublet, as well as to include the neighboring HeI λ5876 emission line and continuum fitting.

The width of the window goes from min λ5888 to maximum λ6223. Na D absorption lines are either from interstellar gas or from cool stars, whereas the HeI line presumably originates in HII regions behind the Na D absorbing gas. Here since HeI line is also from the HII regions it used as a consistency check of Halpha fit of the narrow line (Hα) profile fit, although the values of the fit are not published in this work. The initial parameter of NaD was estimated using the rest wavelength and the redshift and keep the distance between the doublets 6 Angestrom.

The Gaussian fitting method is effective to find the centroid wavelength but is not effective for spectra with large wings (skewed to the blue or red wards relative to systemic) which is an unambiguous indicator of outflowing and infall of gas respectively. Thus, to fit those skewed wings I used Gauss-Hermite function by fixing the kurtosis to zero. The h_3 parameter is affected by the wings and to reduce the number of free parameters of the fit I used a Gauss-Hermite by fixing the kurtosis, and the skewness parameter helps to fit the wings, see Figure 3.2. Most of the Na D-absorption features of our target shows unblended line profiles, i.e they were modeled with a single kinematic component. However very few of them showed asymmetrical and complex profiles that indicate the presence of an additional secondary component, and therefore they require two Gaussian pairs for the fit which I did not go through. The presence of blended components is expected as the Na D absorption feature may have originated in the neutral gas clouds of the ISM as well as in the stars.

Figure 3.2 shows a profile for IC4280 unfitted outflow in the Gaussian case which is not problematic in **Gauss-Hermite routine**. I fitted the two the two absorption lines and He I emission line simultaneously both for Gaussian and Gauss-Hermite function cases.

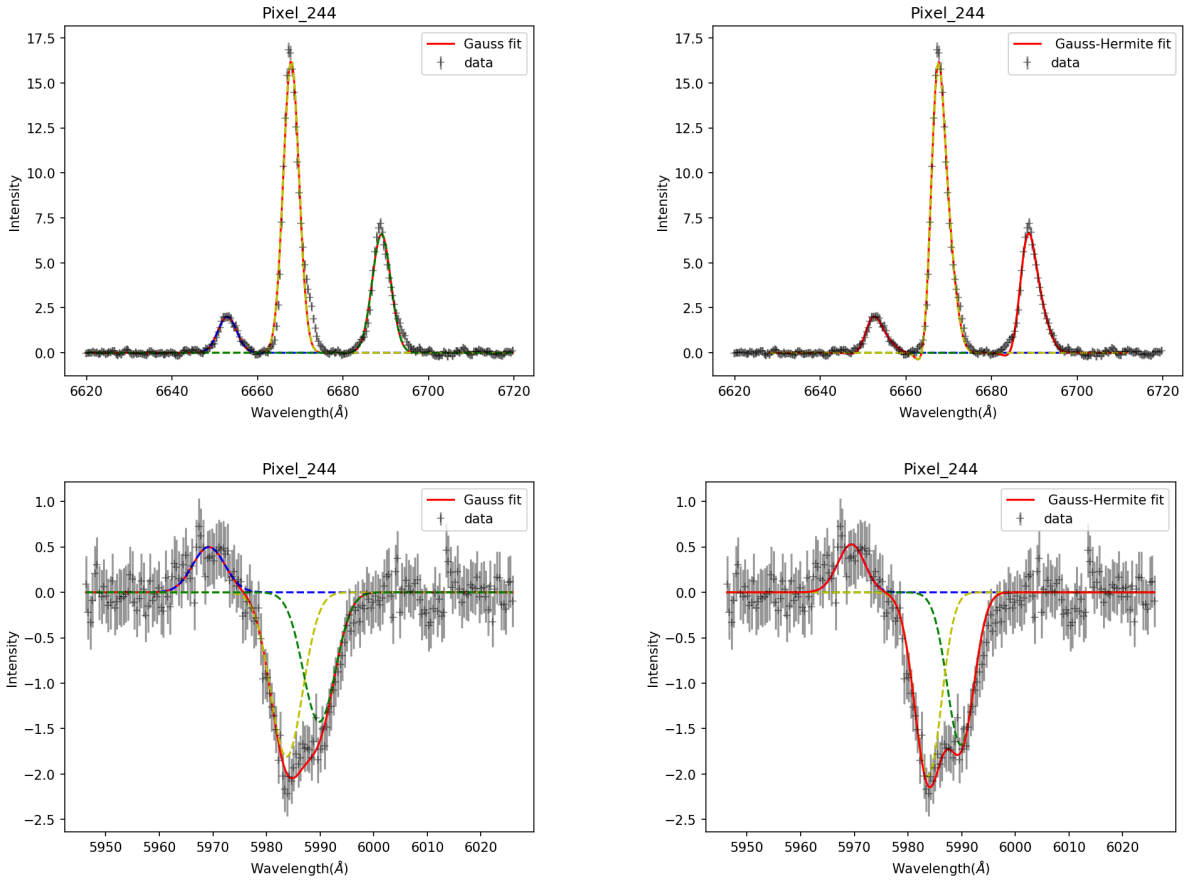

Figure 3.2: A single Gaussian fit for both H_α-[NII] (top left) and He I-Na D (bottom left) and **Gauss-Hermite fit** (right). In all cases, red solid line is the total fit of dotted individual fits.

3.3 Rotation curves

Once fitting was done, velocities for emission and absorption lines were calculated from the Doppler shift (from profile fits) as:

$$\frac{\Delta\lambda}{\lambda_e} = \frac{v}{c} \tag{3.3}$$

where $\Delta\lambda$ is the difference between oberved wavelength and rest wavelength λ_e and v is the velocity calculated from the fit and c is the speed of light.
I used average velocities of the two NII $[\lambda6548, \lambda6583]$ and H$\alpha[\lambda6563]$ which are from the hot ionized gas. The uncertainties summed in quadrature.The line profiles with afitted amplitude less than three sigma were ejected. By using visual inspection the data and then select more profiles which visually looked like real emission.

$$SNR = (SNR1 + SNR2 + SNR3)/weight \tag{3.4}$$

where

- $SNR1 = \frac{A1}{A1err}$
- $SNR2 = \frac{A2}{A2err}$
- $SNR3 = \frac{A3}{A3err}$
- $weight = \frac{1}{A1err^2} + \frac{1}{A2err^2} + \frac{1}{A3err^2}$

Note: SNR1, SNR2 and SNR3 are for NII[6548], Hα and NII[6583] repectively. Also A1, A2, A3, A1err, A2err, A3err are amplitudes and their error. The same procedure followed for NaD. But the SNR for NaD is only the average of the two velocities i.e. NaD[5890,5896]. Then I plotted velocity in km s^{-1} vs distance from the galactic center with error bars. I plotted distance in arc-seconds x-axis (top) plotted and bottom in kiloparsec (kpc). Pixel to parsec and pixel to arcsec conversion values are taken from Ramphul (priv, communication). Only two of our targets, CGCG049-057(PA=0) and IRAS12116-5615 had a sapatial selection bins of 4, the rest are bin 2. And except the two objects CGCG049-057(PA=0) and IRAS12116-5615, all others are 1 pixel wide.

To plot Na D rotation curve, I used the average of the doublets and the same procedure as

plotting for emission that I used above. I plotted the rotation of the ionized and the cool neutral gas together in one plot to study the feedback.

Three approaches were compared to estimate the systemic velocity, V_{sys}. The first method, method I, the V_{sysI} was estimated at the maximum location of peak continuum. The location of the peak continuum is defined by the spatial axis location of maximum counts after collapsing the 2D spectral image in the spectral dispersion direction. For method II, the spatial coordinate where the rotation curve starts to flatten (i.e. where the gradient rapidly becomes shallower or even changes sign) is chosen on both sides of the galaxy. The corresponding velocities at maximum and minimum define the full range, and the V_{sysII} is determined as the value exactly at the middle of these. And the third, method III, V_{sysIII} is determined the mid point between the maximum and minimum velocities from the rotation curve. For all the three methods the systemic V_{sys}, offset velocity ΔV, maximum velocity V_{max} and escape velocity V_{esc} calculated and also each methods was compared . V_{sysI} and ΔV_I was preferred from method I for further analysis. I preferred V_{sysI} than others because in all cases mehtod I has both NaD and Hα which ideal to estimate V_{sys}. Then ΔV_I was calculated from V_{sys}, see Section 4.2. Method II has limitations in caseses where the rotation curve does not flatten off or when the rotation curve is complex such as interacting cases for not flattening rotation curves and interacting cases. Method III was used for V_{max} since it is less subjective than method II. V_{max} from method III was estimated directly from the rotation curve. In this method(III) there are cases where the nearest values used; for cases where NaD does not extend as far as Hα. Through out the thesis notations I, II and III used for method one, method two, and method three respectively.
Method I was used as a plotting axis due to the reason that contains(touch) both NaD and Hα. And the V_{sys} of Method II and Method III V_{sysI} plotted over method I axis. In some cases there only one or two lines might be seen when each method overlap each other, i.e in cases when there are the same value of V_{sys} between each of the three methods.
The targets' rotation curve grouped in to two different categories based on:

- i, The angle between the slit and the major axis of rotation, which I refer hereafter as position angle, θ and
- ii,offset velocity, ΔV_I.

The first group(i) subdivided as θ below and above 45°, for more detail see Section 3.4. The second group(ii) also subgrouped into three, which is based on the offset velocity values; small offset (up to 30 kms^{-1}), medium offset (30-100 kms^{-1}) and big offset (>100 kms^{-1}). Refer Section 3.5.

3.4 Based on Position angle

In this thesis the angle between the major axis and the slit position will be referred as position angle θ. I grouped rotation curves into cases where the slit was less than 45° from the major axis or over 45° from the major axis. This is done since I expect conical outflows to be along the minor axis. In this case where slit is more than 45° from the major axis is the ones I expect to see conical outflows. But for simplicity through out this thesis I will refer θ less than 45° as major axis and the groups where θ above 45° as minor axis.
Table 3.1 provides list of measurements about this group. The Table contains both groups. From the table 1 to 28 is groupI where ($\theta < 45°$) from the major axis. And from 28 to 40 is groupII where θ was greater than 45° from the major axis. Since maximum V_{max} of the rotation velocity associated with PA it is included here.
In the first catagory or major axis group, except a few cases, almost all show a corotation of Hα and NaD. Most of the gas seems originating from the disk. While the second, minor axis group shows very large offset (from the systemic which might indicate that the gas is originating from the nuclear region), some are intermediate, i.e nucear and disk, and some of the targets show unusal rotation curves which is difficult to group.For more detail see Figures 3.3 and 3.4. Horizontal line is used to identify each of the sub groups. In Table 3.1 the specific star formation rate, sSFR and SFR are taken from Ramphul (priv. communication) and the rest of the measurements are evaluated by the author.
The origin of the gas was studied based on the shape of rotation curve of neutral NaD relative to ionised Hα and also considering the offset velocity values ΔV. The origin of the gas catagorised as nuclear and disk driven. The first group which are identified as nuclear driven gas, the shape of NaD curve realtive to Hα which seems coming from the center of the galaxy. And the second group which are identified as disk driven gas, the roation of NaD shows following the rotation of Hα which is an indicator of disk driven gas. For detail refer Section 4.3 and Tables 4.1 and 4.2

Table 3.1: Major ($\theta < 45°$) and Minor ($\theta > 45°$)

Name of target	PAgal	θ	SFR	sSFR	M	VmaxI	VmaxII	VmaxIII	Type
(1)	(2)	(3)	(4)	(5)	(6)	(7)	(8)	(9)	(10)
IRASF17138-1017	72.2	0	1.65	-9.26	10.8	161.73	152.12	148.80	s.burst
MCG-02-33-098	66.2	1	1.18	-9.30	10.15	172.55	102.92	159.54	s.busrt
CGCG049-057(PA=199)	53.9	1	1.5	-9.99	9.74	61.04	97.23	97.23	s.burst
NGC4433	38.6	2.7	1.1	-9.33	9.85	215.60	176.90	205.25	s.busrt
NGC1204(PA=173)	63.9	3	1.11	-10.16	10.34	263.30	213.02	190.43	s.burst
NGC1204(PA=253)	63.9	3	1.11	-10.16	10.34	251.12	181.47	181.47	s.burst
ESO428-G023	41.8	4	0.99	-9.74	10.39	195.13	215.16	166.75	s.burst
NGC1819(PA=125)	61.9	5	1.13	-9.79	10.59	42.84	42.85	33.63	SBO
ESO154-G010	42.8	5.5	-	-	10.2	50.53	34.23	33.73	-
NGC3508	54.0	5.5	1.13	-9.46	10.22	212.18	182.84	185.37	s.burst
ESO550-IG025(PA=242)	134.2	7	1.26	-	10.49	204.17	243.15	236.53	pair/triple
IRASF01364-1042	205.5	7	1.99	-	10.13	178.61	96.53	100.27	s.burst
IRAS18293-3413(PA=128)	75.7	8	2.04	-11.25	10.63	269.57	185.90	185.90	s.burst
ESO264-G057	71.6	8.4	1.31	-9.45	10.41	126.37	105.74	109.58	s.burst
ESO320-G030(PA=135)	42.4	10	1.33	-9.59	10.32	158.78	209.52	209.52	s.burst
ESO440-IG058(PA=57.8)	97.0	12	1.51	-	10.34	245.17	143.93	170.33	s.burst
ESO264-G036	85.3	16	1.58	-9.97	10.77	248.05	287.22	263.66	s.burst
NGC6000	30.2	19	1.2	-9.54	-	223.11	210.52	200.53	s.burst
CGCG049-057(PA=0)	53.9	20	1.5	-9.99	9.74	61.59	109.04	109.04	s.burst
NGC6240 (PA=45)	99.4	20	2.08	-	-	428.74	294.14	309.83	s.burst
ESO267-G030	77.0	25	1.42	-9.56	10.56	258.53	230.33	260.18	s.burst
IRASF08520-6850(PA=50)	191.7	25	1.99	-	-	248.61	241.88	147.75	
ESO440-IG058(PA=245)	97.4	29.5	0.82	-10.28	9.76	12.22	7.46	24.49	s.burst
ESO319-G022	68.0	30	1.27	-9.85	10.2	0.15	27.28	25.21	s.burst
IC4280	67.8	31	1.31	-	-	310.43	348.20	314.91	s.burst
IRASF08520-6850(PA=108)	191.7	33	1.99	-	-	63.12	155.15	152.41	-
NGC3110 (PA=111)	70.1	34	1.5	-9.39	10.57	124.95	139.28	132.24	s.busrt
IRASF06076-2139	158.2	36	1.8	-9.86	10.45	419.52	286.48	263.88	s.burst
ESO320-G030(PA=90)	44.6	55	1.33	-9.59	10.32	279.50	242.30	242.30	s.burst
IRASF18293-3413(PA=55)	75.7	65	2.04	-11.23	10.63	293.53	256.74	270.68	s.burst
NGC6240(PA=90)	99.4	65	2.08	-	-	441.83	431.80	603.37	s.burst
NGC2369 (PA=250)	44.8	65	1.33	-	-	61.45	72.56	205.89	-
ESO491-G020	41.1	67	1.0	-9.46	10.08	569.67	343.21	327.99	s.burst
NGC1819 (PA=225)	61.9	75	1.13	-9.79	10.59	998.91	902.37	756.07	SBO
IRAS12116-5615	113.6	99	1.82	-	10.4	431.69	419.36	454.41	s.burst
NGC3110(PA=43.7)	70.1	101	1.54	-9.39	10.57	1169.81	1005.40	1005.40	s.burst
ESO550-IG025 (PA=219)	134.2	116	1.47	-	10.58	335.45	216.20	224.64	pair/triple
ESO221-IG010	42.8	130	1.4	-9.26	10.28	111.86	110.59	94.72	s.burst
NGC3110(PA=185)	70.1	140	1.54	-9.39	10.57	320.98	312.55	304.79	s.burst
NGC2369(PA=350)	44.8	165	1.33	-	-	324.46	253.05	301.13	-

Notes. Col(1): Name of galaxies, Col(2): θ(in degree),Col(3): position angle of galaxy Col(4): Log(SFR($M_\odot$/yr)) Col(5): Log(sSFR(yr^{-1})), Col(6): Log(st. mass($M_\odot$)), Col(7): V_{maxI}(kms^{-1}), Col(8): V_{maxII}(kms^{-1}), Col(9): V_{maxIII}(kms^{-1}), Col(10): type of object. Note: the table contains both the major and minor axis groups. And the middle double horizontal line is used to identify each of the sub groups

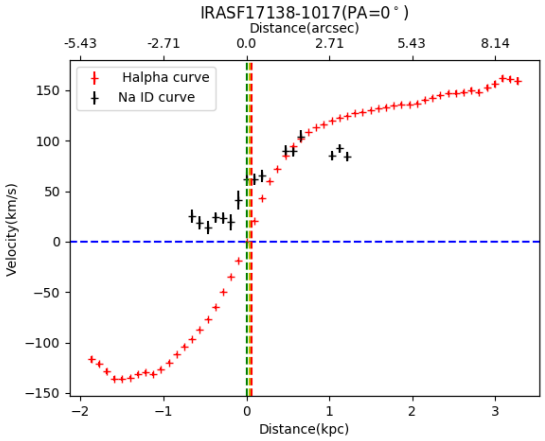

(3.4.1) IRASF171381017[PA=0°]

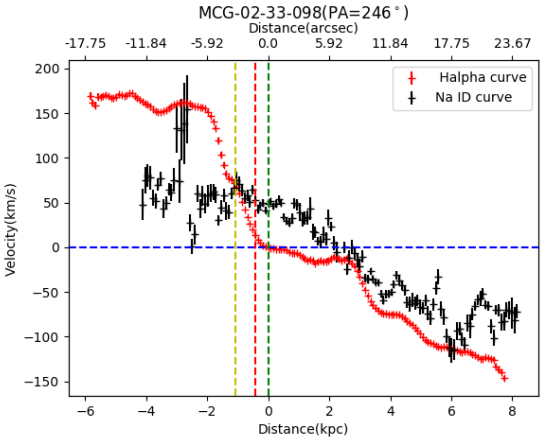

(3.4.2) MCG0233098[PA=246°]

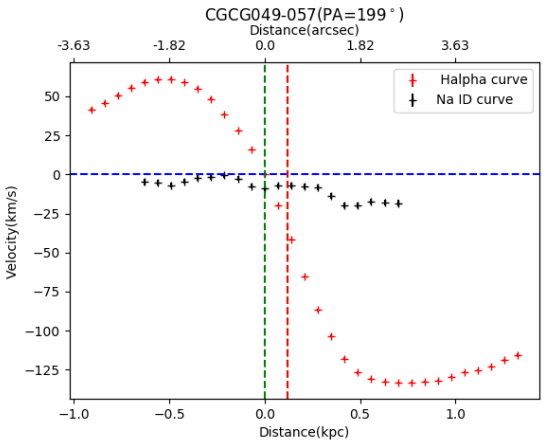

(3.4.3) CGCG049-057[PA=199°]

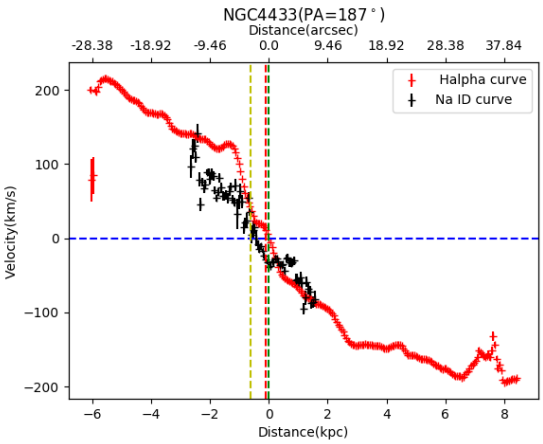

(3.4.4) NGC4433[PA=187°]

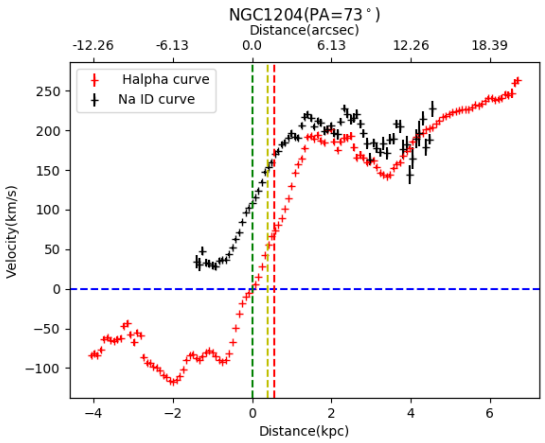

(3.4.5) NGC1204[PA=73°]

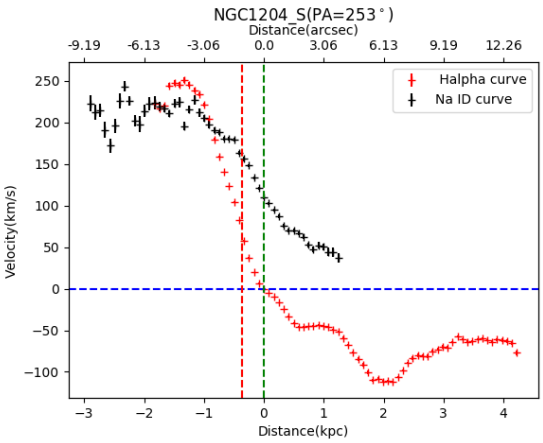

(3.4.6) NGC1204[PA=253°]

Figure 3.3: Major axis observations $\theta < 45$. The red and black with error bars show Hα and NaD respectively. The error bars show the uncertanities of the profile fitting. The green, yellow and red dashed lines indicate the x-position(in arecsec/kpc) of V_{sysI},V_{sysII} and V_{sysIII} respectively plotted on method I axis. Blue line shows the V_{sysI}.

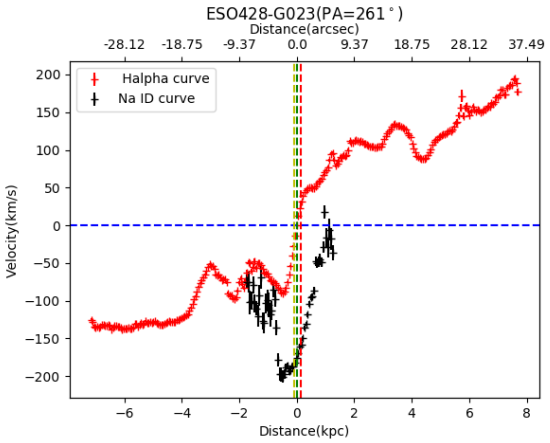

(3.4.7) ESO428G023[PA=261°]

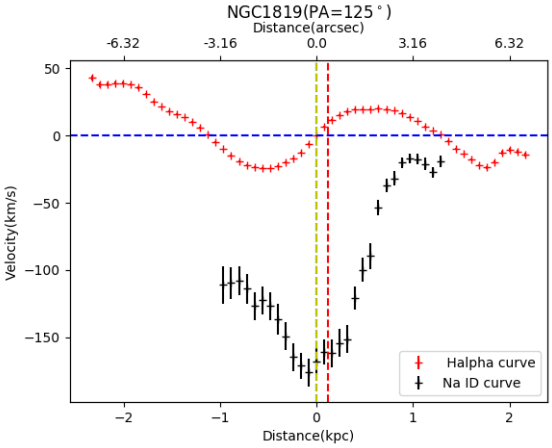

(3.4.8) NGC1819[PA=125°]

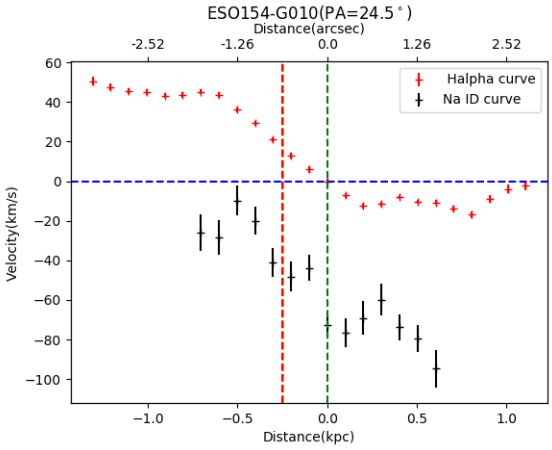

(3.4.9) ESO154G010[PA=24.5°]

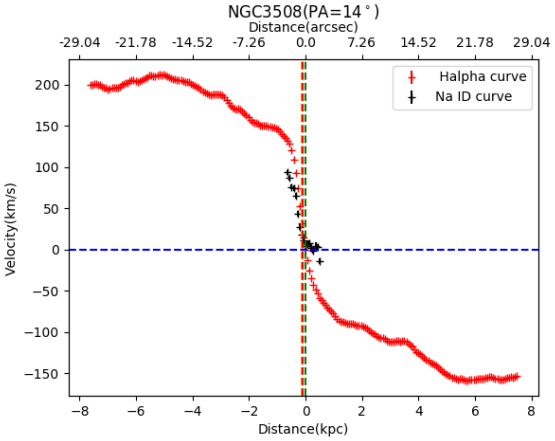

(3.4.10) NGC3508[PA=14°]

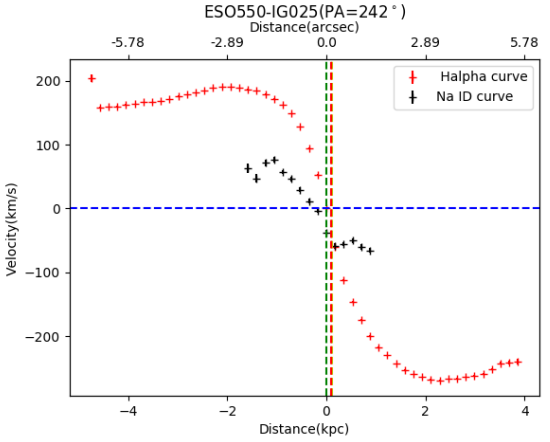

(3.4.11) ESO550-IG025[PA=242°]

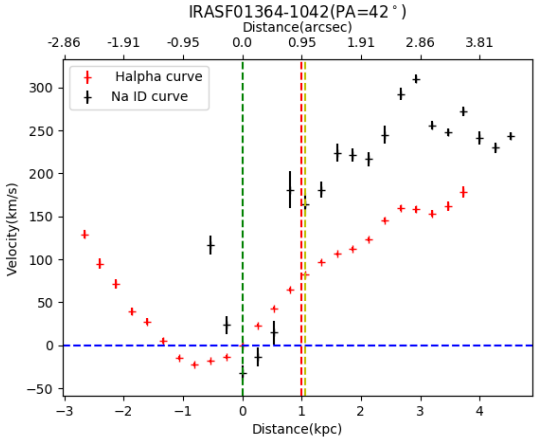

(3.4.12) IRASF013641042[PA=42°]

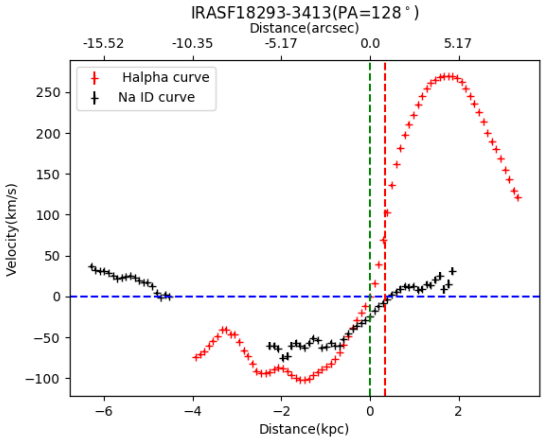

(3.4.13) IRASF18293-3413[PA=128°]

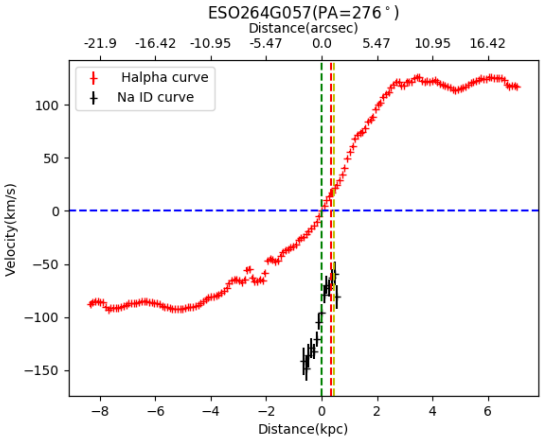

(3.4.14) ESO264G057[PA=276°]

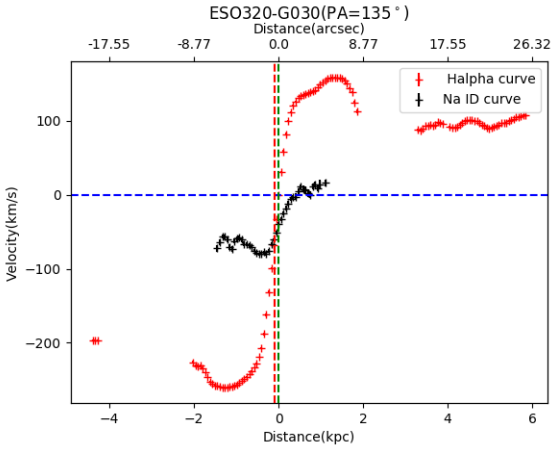

(3.4.15) ESO320-G030[PA=135°]

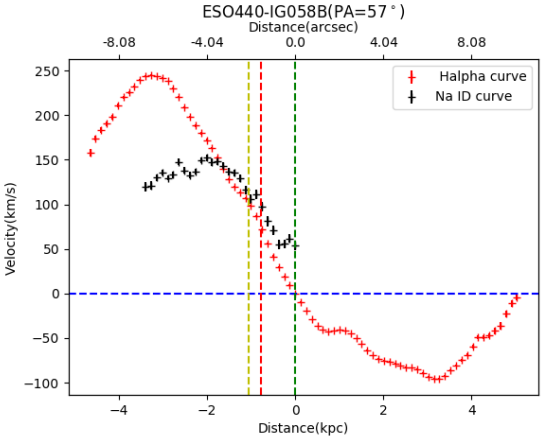

(3.4.16) ESO440-IG058B[PA=57°]

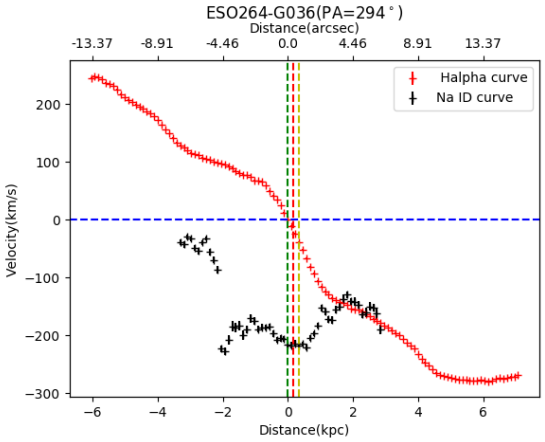

(3.4.17) ESO264G036[PA=294°]

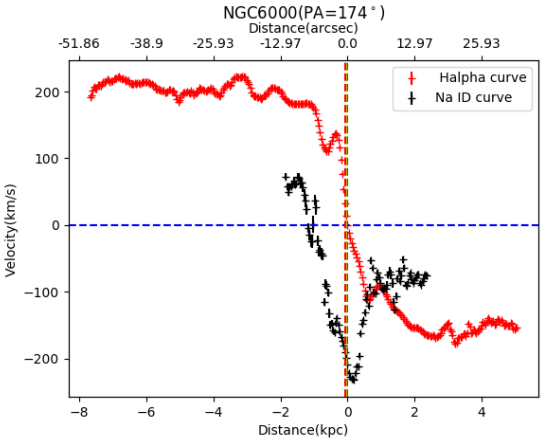

(3.4.18) NGC6000[PA=174°]

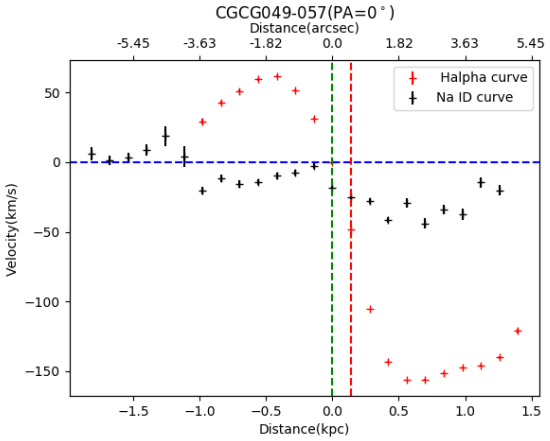

(3.4.19) CGCG049-057[PA=0°]

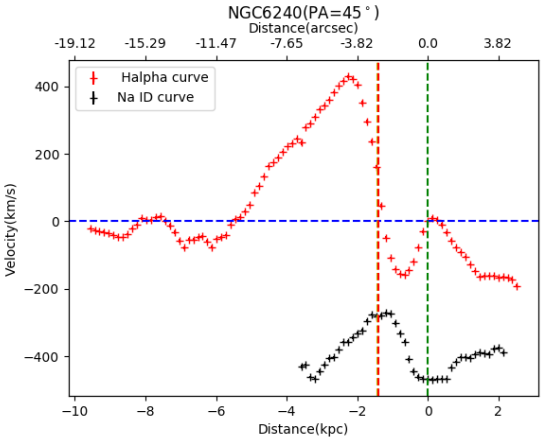

(3.4.20) NGC6240[PA=45°]

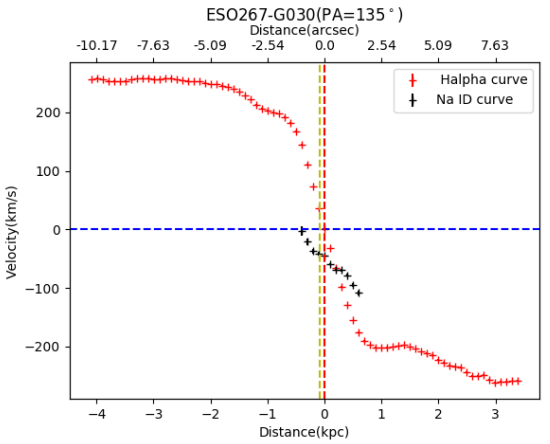

(3.4.21) ESO267-G030[PA=135°]

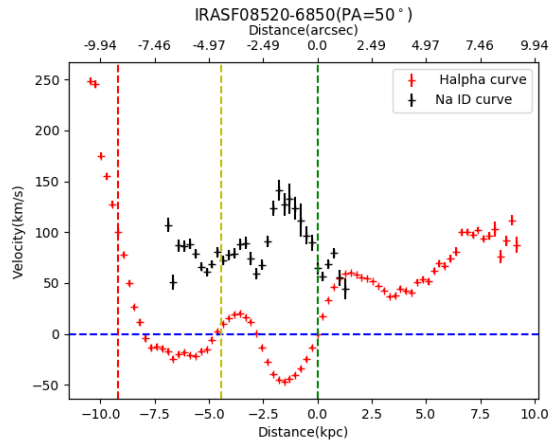

(3.4.22) IRASF085206850[PA=50°]

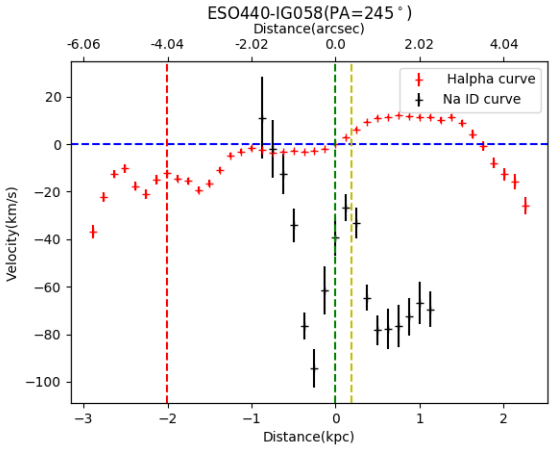

(3.4.23) ESO440IG058[PA=245°]

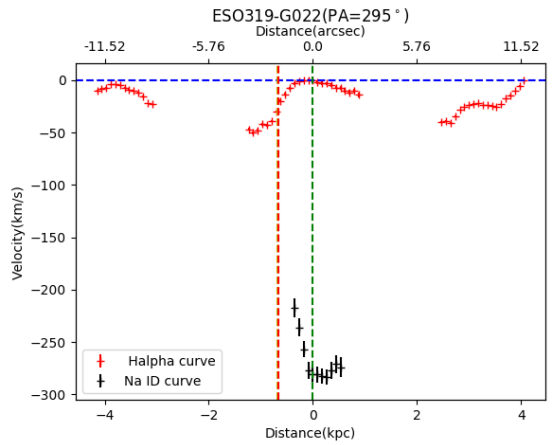

(3.4.24) ESO319-G022[PA=295°]

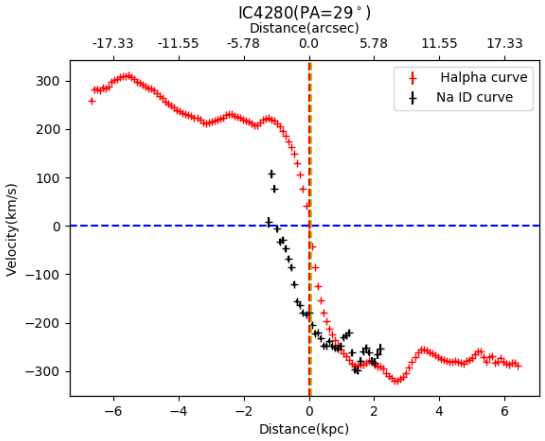

(3.4.25) IC4280[PA=29°]

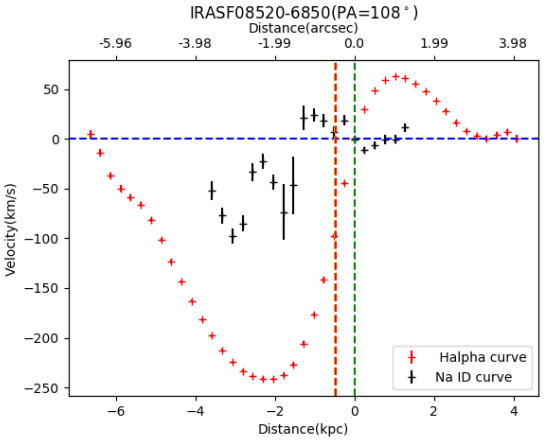

(3.4.26) IRASF085206850[PA=108°]

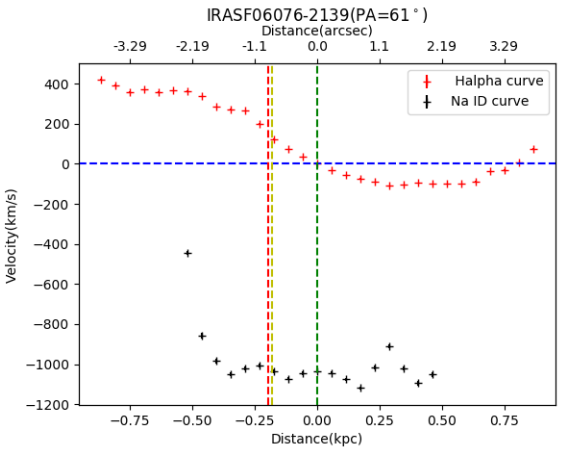

(3.4.27) IRASF060762139[PA=61°]

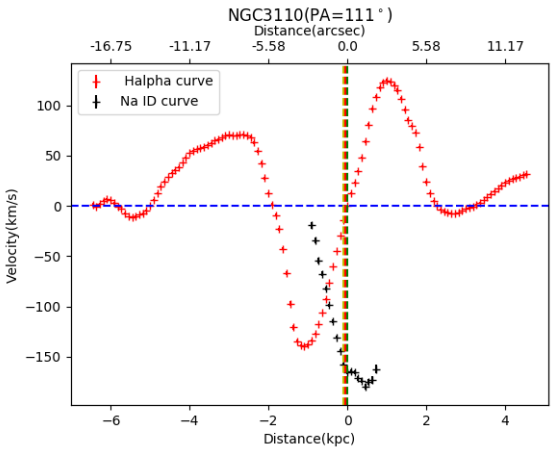

(3.4.28) NGC3110[PA=111°]

Figure 3.3: Continued. Major axis observations $\theta < 45$. The red and black with error bars show Hα and NaD respectively. The error bars show the uncertanities of the profile fitting. The green, yellow and red dashed lines indicate the x-position(in arecsec/kpc) of V_{sysI},V_{sysII} and V_{sysIII} respectively plotted on method I axis. Blue line shows the V_{sysI}.

Figure 3.4: Minor axis observations $\theta > 45$. Note: The green, blue, yellow and red lines have the same meaning as Section 3.3.

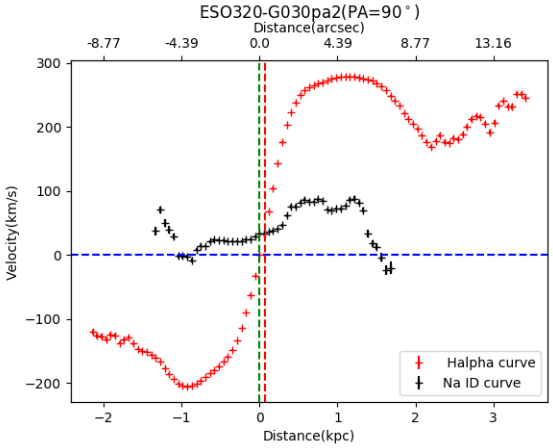

(3.4.1) ESO320-G030[PA=90°]

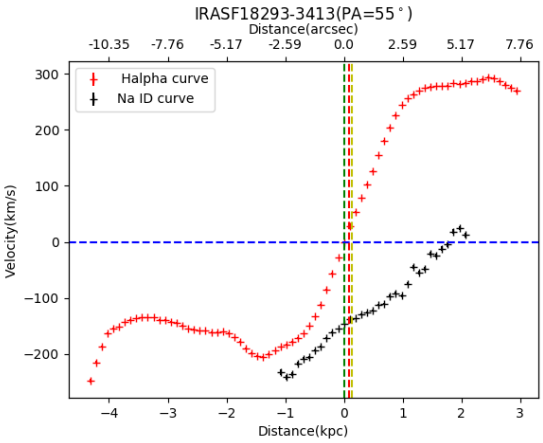

(3.4.2) IRASF18293-3413[PA=55°]

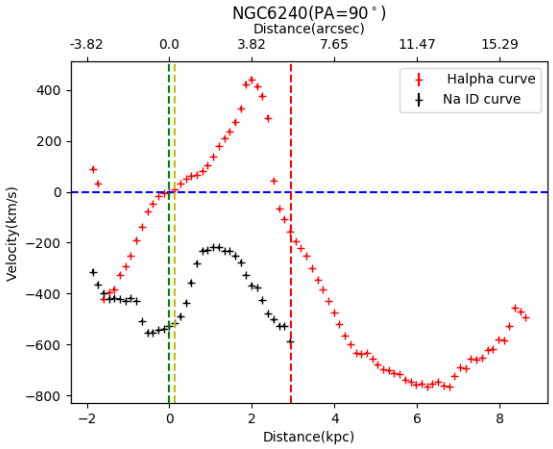

(3.4.3) NGC6240[PA=90°]

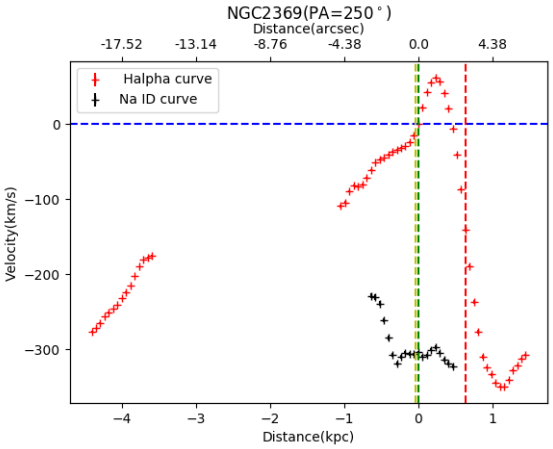

(3.4.4) NGC2369[PA=250°]

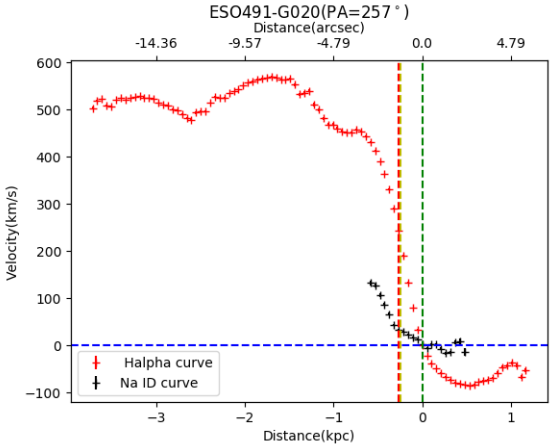

(3.4.5) ESO491-G020[PA=257°]

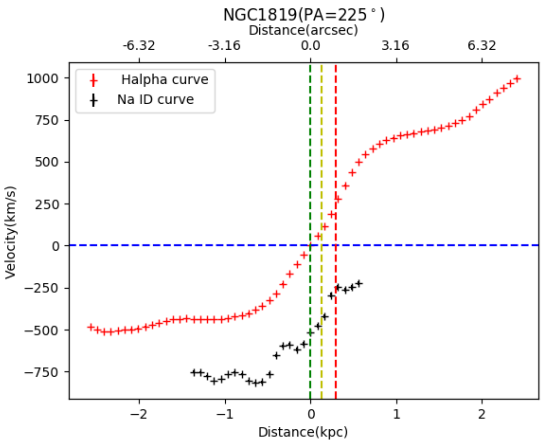

(3.4.6) NGC1819[PA=225°]

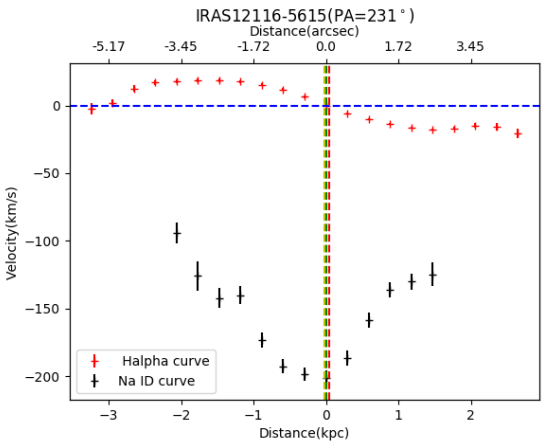

(3.4.7) IRAS121165615[PA=231°]

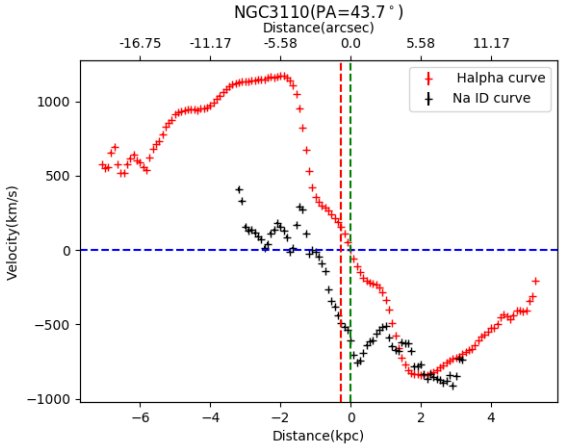

(3.4.8) NGC3110[PA=43.7°]

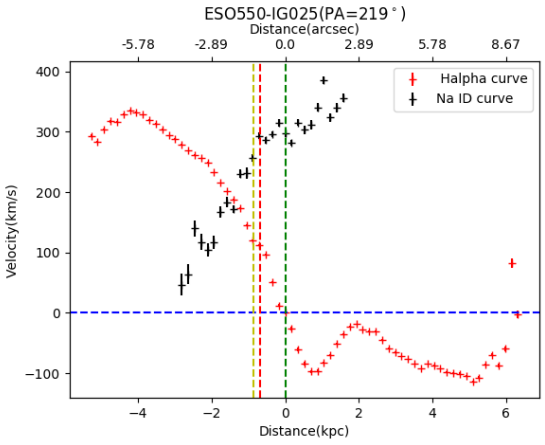

(3.4.9) ESO550IG025[PA=219°]

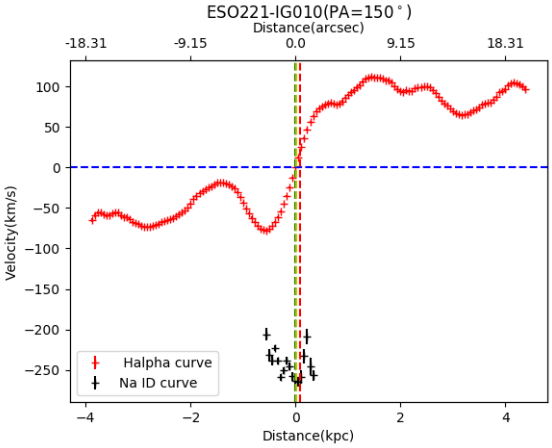

(3.4.10) ESO221IG010[PA=150°]

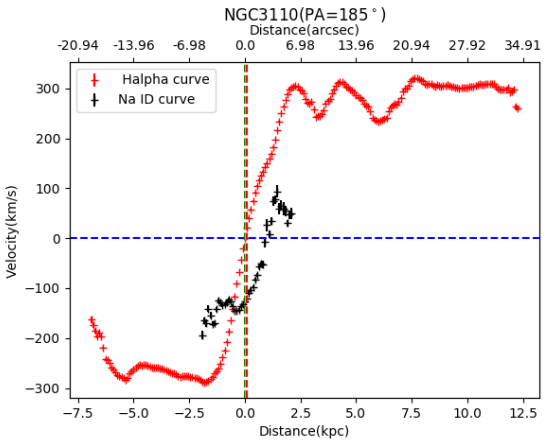

(3.4.11) NGC3110[PA=185°]

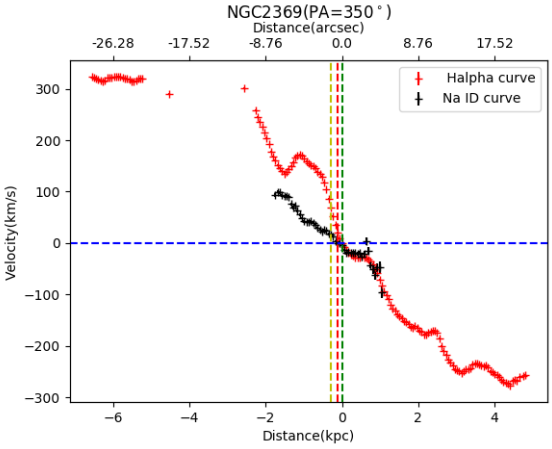

(3.4.12) NGC2369[PA=350°]

Figure 3.4: Continued. Minor axis observations $\theta > 45$. Note: The green, blue, yellow and red lines have the same meaning as Section 3.3.

3.5 Based on Offset Velocity

This is the second grouping of the rotation curve of our samples. NaD offset velocity from method one is used for the grouping, see Section 4.2 for the estimation of NaD offset veocity. I preferred method one since the systemic velocity contains both NaD and Hα where method two and method three do not do. Based on the value of NaD offset velocity relative to Hα curve, I grouped the rotation curves into three categories. Small offset; up to 30 km s^{-1}, medium offset; 30 to 100 km s^{-1} and large offset more than 100 km s^{-1}.

3.5.1 Small offset(up to 30 km s^{-1})

In this group almost all of the targets show Hα rotation except IRASF08520-6850(PA=108) and IRASF013641042. There is an offset velocity of NaD relative to Hα upto 30 km s^{-1} and it has been also seen offset of Hα up to 83 km s^{-1}.

3.5.2 Medium Offset Velocity(30-100 km s^{-1})

This group also shows a clear rotation of both Hα and NaD, though there are a few cases which shows unclear rotation. The redshifted velocity which is interpreted as an infall gas reaches $\sim$100 km s^{-1}. It has also very large V_{max} reaching 1005 km s^{-1}.

3.5.3 Large Offset Velocity (100-380 km s^{-1})

In this group the largest offset of NaD is seen up to 380km s^{-1}. There are two cases that I used the nearest value since there is no NaD which extend as far as Hα. Eg. NGC2369 [PA=250] and ESO319-G022.
Table 3.2 shows all the three subgroups based on offset.

Table 3.2: Group based on offset

Object Name	V_{sysI}	V_{sysII}	V_{sysIII}	ΔV_I	ΔV_{II}	ΔV_{III}	$H\alpha_{II}$	$H\alpha_{III}$	V_{escI}	V_{escII}	V_{escIII}
	(km/s)	(km/s)	(km/s)	(km/s)	(km/s)	(km/s)	(km/s)	(km/s)	(km/s)	(km/s)	(km/s)
(1)	(2)	(3)	(4)	(5)	(6)	(7)	(8)	(9)	(10)	(11)	(12)
ESO491-G020	2953.86	3032.41	3037.69	-0.46	67.82	72.73	78.56	83.84	1464.08	882.08	842.95
IRASF08520-6850(108)	13543.82	13483.00	13484.81	0.67	-66.16	-64.75	-60.82	-59.01	162.22	398.75	391.70
NGC2369 (350)	3197.17	3258.35	3217.16	2.98	46.61	19.19	61.19	20.00	833.89	650.35	773.91
NGC3508	3856.33	3880.54	3878.45	-3.81	9.97	8.75	24.21	22.12	545.32	469.91	476.42
CGCG049-057(199)	3895.70	3864.78	3864.78	7.79	-24.63	-24.63	-30.92	-30.92	156.87	249.89	249.89
CGCG049-057(0)	3890.54	3852.45	3852.45	15.00	-18.20	-18.20	-38.10	-38.10	158.29	280.24	280.24
ESO320-G030(90)	3065.62	3084.28	3084.28	-16.96	1.96	1.96	18.66	18.66	718.33	622.73	622.73
IRASF01364-1042	14431.78	14476.00	14473.99	17.35	-44.77	-48.65	44.22	42.20	459.05	248.09	257.71
IRAS18293-3413(128)	5459.09	5526.54	5526.54	19.30	72.51	72.51	67.45	67.45	692.82	477.78	477.78
ESO550-IG025(242)	9776.39	9745.91	9751.09	29.35	9.60	12.96	-30.48	-25.30	524.74	624.90	607.88
ESO440-IG058(245)	6993.34	6997.00	6983.91	30.07	26.85	-18.00	3.66	-9.43	31.41	19.17	62.95
ESO267-G030	5469.12	5488.70	5467.98	31.16	48.85	30.53	19.58	-1.14	664.45	591.97	668.67
ESO320-G030(135)	3123.33	3079.62	3079.62	34.50	4.52	4.52	-43.70	-43.70	408.07	538.47	538.47
NGC4433	2969.94	3006.00	2979.58	35.86	19.62	36.37	36.06	9.64	554.10	454.64	527.51
IRASF08520-6850(50)	13476.38	13481.19	13548.42	-46.03	-49.07	-4.33	4.81	72.04	638.95	621.65	379.72
MCG-02-33-098	4796.38	4864.22	4809.05	-46.91	-1.62	-37.97	67.83	12.67	443.46	264.51	410.04
ESO 154-G010	5549.23	5560.08	5560.42	48.27	40.92	40.97	10.85	11.19	129.86	87.98	86.69
IRASF17138-1017	5190.52	5198.09	5200.70	-48.87	-41.28	-38.66	7.57	10.19	415.65	390.96	382.43
ESO440-IG058(57.8)	6812.59	6905.93	6881.60	-49.53	-7.42	-22.87	93.35	69.01	630.11	369.91	437.75
IRASF18293-3413(55)	5481.67	5494.33	5489.53	50.13	59.86	55.58	12.66	7.86	754.40	659.84	695.66
ESO264-G057	5099.36	5115.00	5112.09	72.28	60.94	61.72	15.64	12.72	324.78	271.75	281.62
NGC3110(185)	5067.73	5072.99	5077.83	79.14	82.73	86.04	5.26	10.10	824.94	803.27	783.32
ESO550-IG025(219)	9604.58	9636.77	9634.49	-80.31	-38.27	-48.94	32.19	29.91	862.13	555.64	577.33
IC4280	4893.57	4875.00	4891.37	88.37	80.55	87.44	-18.57	-2.20	797.82	894.90	809.34
NGC3110(43.7)	5066.42	5091.96	5091.96	94.73	100.04	100.04	25.54	25.54	3006.48	2583.92	2583.92
NGC1204(73)	4463.41	4509.45	4530.14	-99.57	-92.43	-88.24	46.05	66.73	676.69	547.47	489.42
NGC1204(253)	4429.38	4493.17	4493.17	-100.82	-82.51	-82.51	63.78	63.78	645.39	466.40	466.40
NGC1819(225)	4400.29	4421.00	4452.39	111.17	115.22	109.07	20.71	52.11	2567.25	2319.14	1943.13
NGC3110(111)	5098.67	5089.00	5093.75	111.53	96.50	103.90	-9.67	-4.92	321.13	357.95	339.86
NGC2369 (250)	3316.21	3312.04	3262.06	113.86	110.49	66.90	-4.17	-54.15	157.92	186.50	529.15
ESO 221-IG010	3148.34	3148.96	3156.78	129.86	130.54	137.79	0.63	8.44	287.47	284.21	243.43
NGC1819(125)	4439.76	4439.75	4447.36	138.68	138.68	140.93	-0.01	7.61	110.10	110.12	86.43
NGC6000	2170.97	2179.48	2186.22	141.02	143.61	146.87	8.50	15.25	573.39	541.05	515.38
ESO428-G023	2987.77	2970.03	3012.91	155.40	145.73	166.10	-17.74	25.14	501.50	552.98	428.56
IRASF06076-2139	11238.00	11259.46	11263.11	166.80	188.03	190.30	21.46	25.10	1078.18	736.26	678.18
ESO264-G036	6154.21	6123.00	6141.78	171.89	141.74	159.38	-31.21	-12.44	637.50	738.17	677.62
ESO319-G022	4875.37	4857.38	4858.75	185.89	126.30	127.67	-18.00	-16.63	0.40	70.11	64.80
NGC6240(90)	7285.19	7288.86	7226.07	192.14	191.51	155.87	3.67	-59.12	1135.53	1109.75	1550.69
IRAS12116-5615	8146.13	8146.66	8145.15	201.04	201.38	197.62	0.53	-0.98	1109.47	1077.78	1167.87
NGC6240(45)	7451.41	7560.95	7548.18	380.37	337.34	324.30	109.54	96.77	1101.88	755.95	796.27

Notes. Col(1): Name of targets, Col(2, 3 and 4): systemic velocity V_{sys} of the galaxy for the three methods, method I, method II and method III, Col(5, 6 and 7): offset velocities ΔV, Col(8 and 9): Hα offset velocities (method II and III), Col(10, 11 and 12): escape velocities V_{sysI}, V_{sysII} and V_{sysIII}. Note: I, II and III indicates the three methods, method I, method II and method III rspectively. Horizontal line is used to identify each of the sub groups.

Chapter 4

Discussion

4.1 Relation between the three methods

As I mentioned above in Section 3.3 three methods were used to estimate the systemic velocity V_{sys}. Unfortunately, apart from the V_{rot} errors, I don't have errors for the V_{sys} and V_{max} and ΔV. Note that due to the complicated morphology of the galaxies, the systematic effects resulting from the definitions and methods of determination of these values actually dominate the formal fitting errors. Hence, the best indication of uncertainties in the said velocity parameters come from comparing the three independent methods of arriving at these values. To compare the consistency of the three methods, I plot the difference between methods I and methods II versus method III and method II both for V_{sys} and V_{max}. Refer Figure 4.1 which shows this relation for V_{sys}(left panel) and V_{max}(right panel) respectively. In most of the cases the values of V_{sys}, ΔV and V_{max} show an agreement mostly in method II and method III since both are estimated from the roation curve as already mentioned in Section 3.3.
I calculated the dispersion (σ) for both V_{sys} and V_{max} cases. And I find σ of 28.6 and 22 km s^{-1} for (left panel of Figure 4.1) which is V_{sysI}-V_{sysII} versus V_{sysIII}-V_{sysII} respectively. And also the I found dispersion for (right panel of Figure 4.1) which is V_{maxI}-V_{maxII} versus V_{maxIII}-V_{maxII} is 44 and 54.8 km s^{-1} respectively. The reason the two approaches(method II and method III) differ from method I might be due to:
a), the galaxy may be very disturbed or;
b), dust extinction; infrared images might help in this regard.

Since method I is estimated from the maximum location of the peak continuum, as defined earlier in Section 3.3, here I do not see a close consistency as method II and III do, refer to Figure 4.1. Method II and III are close together, though they show some of the points scattered is mostly due to several outliers, i.e targets with unusual shape of rotation curve. Eg. ESO319-G022(PA=295°), IRASF08520-6850(PA=50°),ESO440-IG058(PA=245°) and NGC2369[PA=250°],

see Figures 3.3 and 3.4. Also for these Four targets the ΔVIII was estimated using the nearest(NaD data point) values for calculation, since the is no NaD data point at V_{sys}III. But note that ΔVIII and V_{sys}III are not used for further analysis as mentioned in Section 3.3.

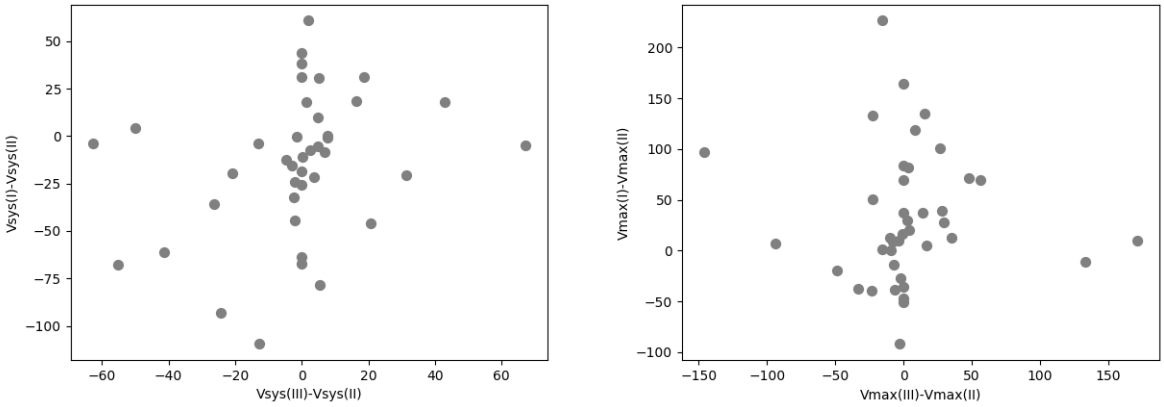

Figure 4.1: Relation between systemic velocities of the three methods left panel and relation between maximum velocities of the three method right panel

4.2 Relation between SFR with Offset and Rotational velocities

Once I determine the V_{sys}, I already have the line of sight velocity V_{LOS} that is also calculated from the Doppler equation (calculated from the line profile fits using python, as mentioned in Section 3.3). The V_{LOS} tells us how fast the gas is moving directly towards or away from us. However, what is needed here is to know is how fast the gas is rotating around the galaxy center; thus, I get the pure rotational speed using the equation

$$V_{\rm rot} = V_{\rm LOS} - V_{\rm sys} \tag{4.1}$$

for all of our targets I have done inclination correction (which tells how the intrinsic rotation velocities of the galaxy are projected to the observed line-of-sight velocities).

$$V_{\rm rot} = \frac{V_{\rm LOS} - V_{\rm sys}}{cos(\theta)sin(i)} \tag{4.2}$$

where θ is is the angle between the slit and the major axis of rotation, and i inclination of the galaxy. Note that: the author used major and minor axis values to calculate inclination and position angle of the galaxy all are taken from Two Micron All-Sky Survey (2MASS). The offset velocity, ΔV estimated from the centroid V_{LOS} of the emission and the centroid V_{LOS} of the

absorption lines respectively.

$$\Delta V = V_{\rm ems} - V_{\rm abs} \tag{4.3}$$

where V_{ems} and V_{abs} are centroid line of sight velocity of the emission and centroid line of sight velocity of the absorption lines respectively. In otherwords V_{ems} and V_{abs} are already calculated from the fit as described in Section 3.1 and Section 3.2. The calculated ΔV values for all our targets are listed in section 3.5, see Table 3.2. Once ΔV calculated, one need to see if there is a correlation between outflowing material and SFR of the galaxy. The second grouping method, method II was used since it is based on offset. There is an expectation that the outflow would correlate with SFR (Rupke and Veilleux, 2005). But our way of estimating V_{sys} is different from theirs, so that one can not do a one to one correlation.
Figure 4.2 shows the log-log plot of NaD offset velocity, ΔV versus SFR (left panel) and also ΔV vs specific star formation rate, sSFR (right panel). There is no correlation seen between the outflow velocity and sSFR as well. Martin (2005) see a positive correlation between outflow velocity and SFR, though they estimated the V_{sys} from NaD line ratios which is different from our method. A recent study by Sugahara et al., 2017 also checked. The authors used two methods to calculate the outflowing velocity; the bulk outflow and the maximum ouflow velocities. And they found a correlation with the maximum velocity of the outflow and no correlation with the bulk outflow. Again I can not compare our result with those studies because their way of estimation of the V_{sys} is absorption line based. where in our case it is based on Hα. Another reason might be the position angels taken from 2MASS are for the total galaxy so the major axis based on 2MASS could be minor axis from the inside of the galaxy and vice versa, eg NGC1819. There are also other cases the internal part of the galaxy is disturbed and different from the outside. Eg. ESO428-G023, ESO319-G022, ESO428-G023 and NGC3110.

Before I compare V_{max} with SFR, I checked the same galaxies with different slit position(PA) observation along the major and minor axis, see Figure 4.3. It is shown that minor axis observations appear to have high velocity compared to the major axis observations. I need also to see if there is a correlation between circular velocity of the host-galaxy V_{max} and SFR. Figure 4.4 shows V_{max} vs SFR for targets in group based on offset velocity, for more detail refer Section 3.4. Figure 4.4 (left panel) shows the first subgroup based on θ which is (θ <45) from the major axis, also see Figure 3.3. Figure 4.4 (right panel) shows the second subgroup based on θ which is (θ >45) from the major axis, also see Figure 3.4. There is no correlation seen between V_{max} and SFR. Although there is no correlation seen, our data seems consistent with Arribas et al. (2014). The Arribas et al. (2014) samples are LIRGs and ULIRGs, since our targets are LIRGs they are consistent with LIRGs, see Figure 4.4(left panel). The right panel of Figure 4.4 shows big discrepancies those are not maximum rotational velocities from the galaxy that is rather an

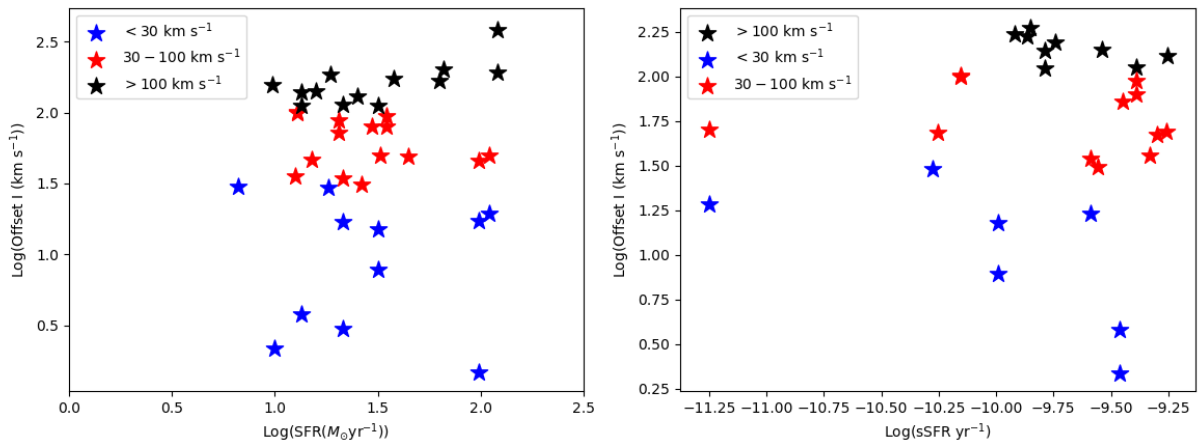

Figure 4.2: ΔV vs SFR (left panel), and ΔV vs sSFR (right panel). The blue, red and black stars indicate the out flow velocities in three subgroups < 30 km s^{-1}, $30 - 100$ km s^{-1} and $100 < 30$ km s^{-1} respectively. Note: The plot is from the group based on offset velocity. For more detail refer Section 3.5.

indication of major outflow as indicated in Figure 4.3 which is a typical indicator of these major outflow.

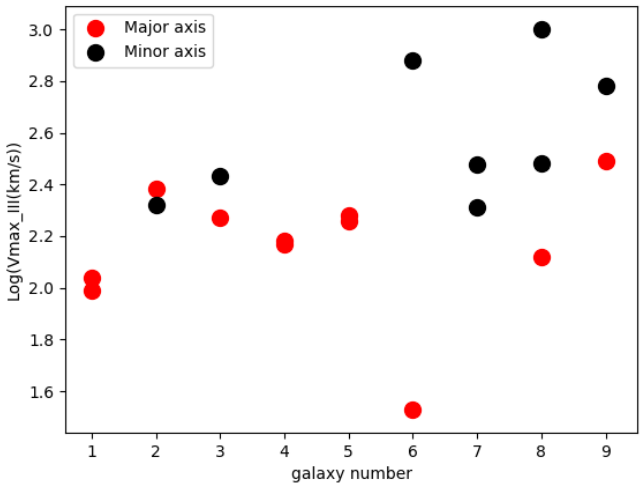

Figure 4.3: V_{max} of major and minor axis observation of the same galaxy with different slit position(PA) vs galaxy number.

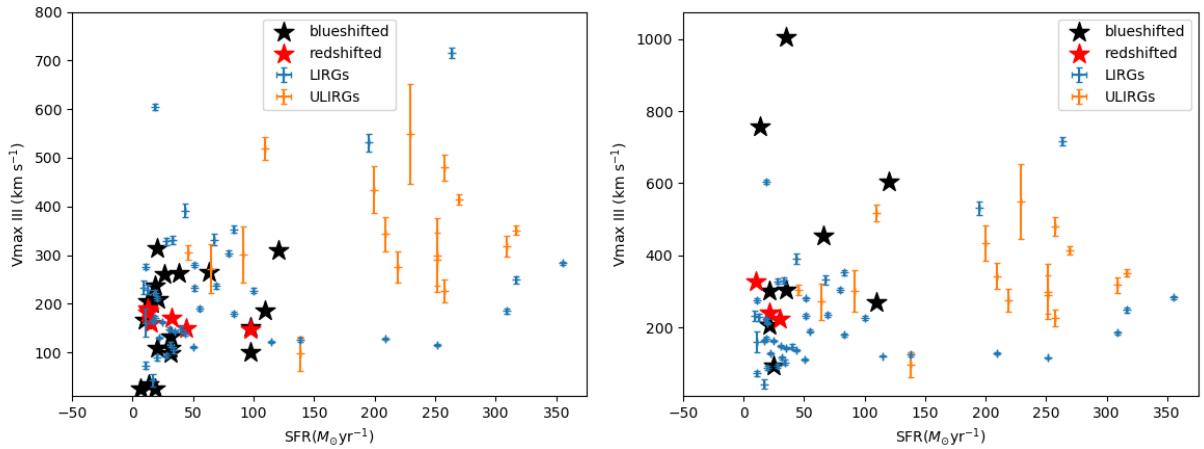

Figure 4.4: Maximum velocity V_{max} vs SFR. The blue and and orange points with their corresponding error bars from Arribas et al. (2014). Note: The plot is from the group based on position angle(θ). Section 3.4

4.3 Nuclear or Disk Driven Gas?

Based on the shape of rotation curve(curve of neutral NaD and ionised Hα) and also considering the offset velocity values ΔV, the origin of the gas is catagorised as nuclear and disk driven. The first group which are identified as nuclear driven gas are based on the shape of NaD curve realtive to Hα which seems coming from the center of the galaxy. The group contains targets NGC1819[PA=125], NGC6240[PA=45], ESO319-G022, IRASF06076-2139, NGC2369[PA=250], NGC1819[PA=225], IRAS12116-5615 and ESO 221-IG0, for more see Section 3.3 and 3.4. For this group(first) the target's offset velocity ΔV are above 100 km s^{-1} was selected.

Where as the second group which are identified as disk driven gas the rotation curve of NaD shows following Hα which is an indicator of the disk driven gas. The group contains targets IRASF17138-1017, MCG-02-33-098, NGC4433, NGC1204[PA=73], NGC1204[PA=253], NGC3508, IRAS18293-3413[PA=128], ESO320-G030[PA=135], ESO440-IG058[PA=57.8], ESO267-G030, IRASF08520-6850[PA=50], IC4280, ESO320-G030[PA=90], IRAS18293-3413[PA=55], for more see Section 3.3 and 3.4. In both cases the shape of the rotation curve also was taken into account. There are also targets which identified as intermediate nuclear driven gas NGC6000, ESO264G036, NGC3110[PA=111], NGC6240[PA=90]. And targets with intermediate disk driven gas ESO154G010, ESO428G023, ESO440IG058[PA=24.5], CGCG049-057[PA=199]. For more detail see Tables 4.1 and 4.2.

Disk (1)	Nuclear (2)
IRASF17138-1017	NGC1819[PA=125]
MCG-02-33-098	NGC6240[PA=45]
NGC4433	ESO319-G022
NGC1204[PA=73]	IRASF06076-2139
NGC1204[PA=253]	NGC2369[PA=250]
NGC3508	NGC1819[PA=225]
IRAS18293-3413[PA=128]	IRAS12116-5615
ESO320-G030[PA=135]	ESO 221-IG0
ESO440-IG058[PA=57.8]	
ESO267-G030	
IRASF08520-6850[PA=50]	
IC4280	
ESO320-G030[PA=90]	
IRAS18293-3413[PA=55]	

Table 4.1: Targets showing Disk and Nuclear driven gas

Intermediate Disk (1)	Intermediate Nuclear (2)
ESO154G010	NGC6000
ESO428G023	ESO264G036
ESO440IG058[PA=24.5]	NGC3110[PA=111]
CGCG049-057[PA=199]	NGC6240[PA=90]

Table 4.2: Targets showing intermediate Disk and intermediate Nuclear driven gas

4.4 Escape Velocities

To study if there is feedback from our sample galaxies, I assume a singular isothermal sphere potential. I derived the V_{esc} from V_{max}, see equation 4.4.

Once I get the V_{max} evaluated, It is possible to address the question,"can the outflows escape the gravitational wells and enrich the intergalactic medium?" To answer the question one can follow Rupke et al. (2002) and Väisänen et al. (2008a), assuming a singular isothermal sphere truncated at r_{max}, the escape velocity V_{esc} at a radius r is related with V_{max} by

$$V_{esc}(r) = \sqrt{2} V_{\max} \left[1 + ln(r_{\max}/r)\right]^{1/2} \tag{4.4}$$

The author choose the $r_{max}/r = 10$ which is the lower value for V_{esc} since it is not sensitive to the choice of r_{max}/r although r_{max}/r can extend to ∼100. Figure 4.5 shows the relation between ΔV and estimated escape velocity of host galaxy. I get two of the targets (ESO319-G022 and NGC1819(PA=125) escaping out of the potential well. For instance for ESO319-G022 even if I choose $r_{max}/r = 100$, V_{esc} becomes 83.7 km s^{-1} which is still less than ΔV (185.9 km s^{-1}). For this target the major axis from 2MASS is 85°, see (2MASS. 2003 vol. p.) but according to "The ESO/Uppsala Survey of the ESO(B) Atlas" Lauberts, A.(1982) the PA is 45 °. As I mentioned above I used 2MASS PA's, so one can expect that its due to this the V_{esc} is less than ΔV. Indeed the rotation curve NaD shows a big offset but has a small V_{max} and the shape of rotation curve looks unusual.

The second target which escapes the potential well is NGC1819(PA=125 °). For the choice $r_{max}/r = 100$ the V_{esc} becomes 112.5 km s^{-1} still less than ΔV (141 km s^{-1}). This target also has different major-minor from inside and outside. In addition, the disk of NGC1819 is surrounded by super star cluster which I expect be a cause for the feedback, see the image of the galaxy A.82.

Thus, I have seen the gas from two of our targets escaping the potential well and enrich the

intergalactic medium (IGM). The rest of our targets have high escape velocities, V_{esc}, see Figure 4.5.

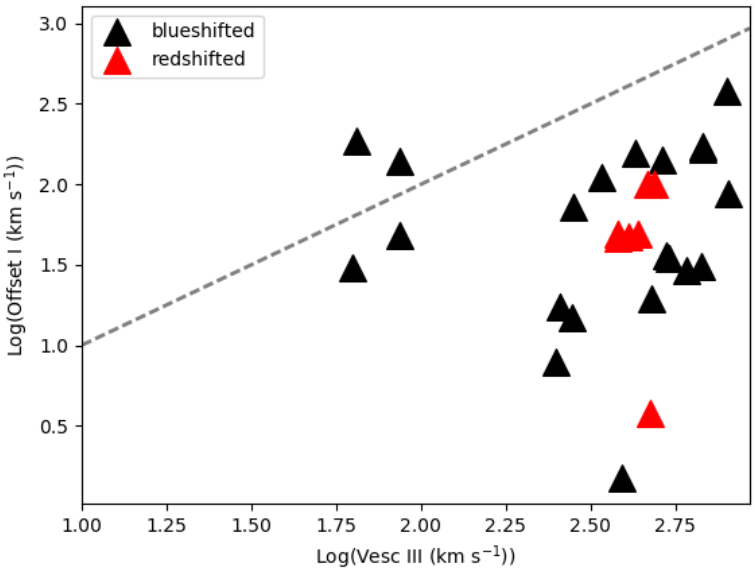

Figure 4.5: Figure : Offset velocity ΔV vs estimated escape velocity of host galaxy V_{esc}. The dash line indicates the one to one line at ΔV=V_{esc}.

Chapter 5

Conclusion and future work

This thesis has focused on 40 LIRGs that are from a SUNBIRD survey. There was an expectation of outflowing correlation with SFR, I compared the results with previous works however the methods I used are different from the others. The reason of not correlation I expect, might be due to;

- uncertainties involved during systemic velocity calculation.
- It might be also due to the major outflow.
- Orientation effect,(due to over correction I found the minor axis observations even greater than major axis ones'.)

I find 8 of our targets as nuclear driven and 14 of them are disk driven outflows, as mentioned in Section 4.3. And also four intermediate nuclear and four intermediate disk driven gas was identified. However the rest of the samples are mixed between nuclear and disk diven, so they are difficult to disentangle. I also find the gas from the two of the targets escape out of the host potential well and enrich the surrounding IGM, though still needs a more detail analysis to make sure it is not due to orientation effect or projection effect on the galaxy. So to the study of conical outflow, a better job would be done if one can use the stellar absorption lines to estimate the systemic velocity.

In this thesis I have analyzed the outflowing velocity of the gas based on Hα rotation curve systemic velocity. The fitted profiles with their uncertainties was used to plot and compare NaD and Hα, though I do not see a correlation with star formation. The future work will be:

- Calculating the mass and energy involved in the outflow process.

- Study the conical outflow using stellar absorption lines to get the intrinsic systemic velocity. The data, P900 exists but it was not part of our thesis.

Appendix A

Comments on individual targets

- **ESO491-G020** is almost a face on galaxy in group of a galaxies (GIG). It has an IR of $\log(L_{IR}/L_{\odot}$=10.86) at a D_L∼41 Mpc. The slit was aligned along the major axis at (PA=257°). As it can be seen there is a rotation of Hα reaching a V_{max} of 328 km s^{-1}. NaD line doesn't extend as far as Hα, see rotation curve 3.4.5. Hα is highly skewed to the blue side which indicates an outflow. It has a small NaD offset velocity ΔV ∼-0.5 km s^{-1} and Hα ΔV of ∼83.8 km s^{-1}.

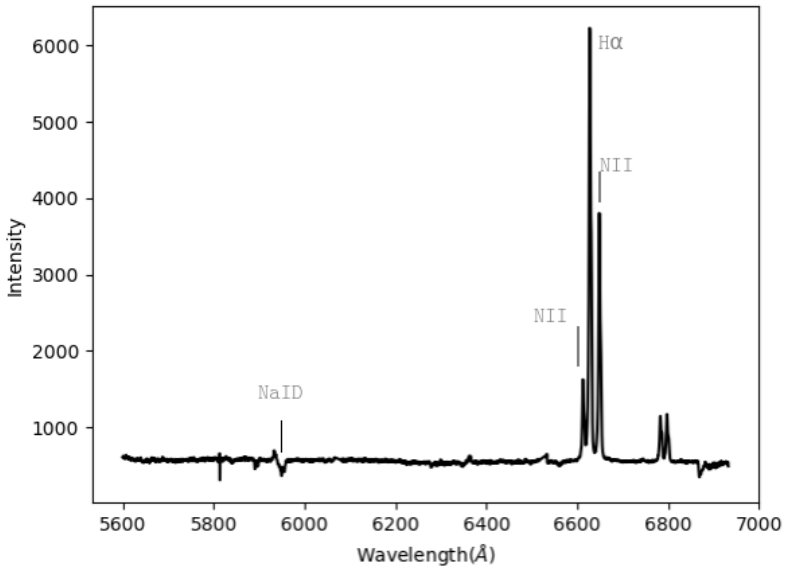

Figure A.1: integrated spectra of ESO491-G020

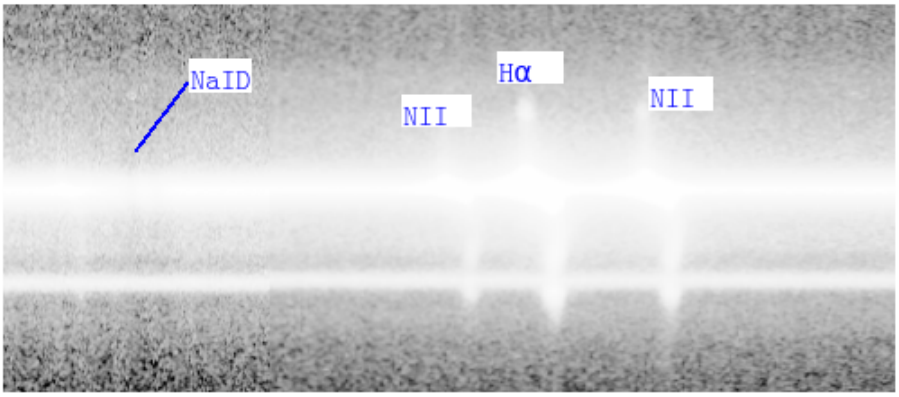

Figure A.2: 2D spectra of ESO491-G020

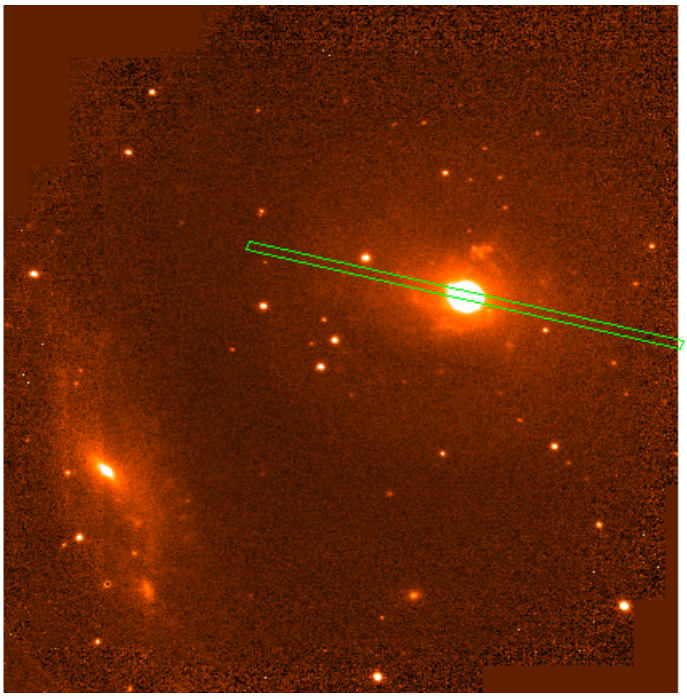

Figure A.3: ESO491G020[PA=257]

- **IRASF08520-6850** is a galaxy pair which has a IR luminosity of $\log(L_{IR}/L_{\odot}$=11.76) at a D_L∼191.7 Mpc. Neither of the two observations (PA=50°) and (PA=108°) are along the major axis, that is why I do not see clear rotation of either Hα or NaD, see A.8 also rotation curves 3.4.22 and 3.4.26. Gauss-Hermite fitting routine shows us large wings (skewed to the blue relative to systemic) as a result of outflowing gas. The (PA=50°) observation shows a red shifted of NaD with ΔV of -46 km s^{-1} relative to the systemic velocity and has Hα ΔV of 72 km s^{-1} and its maximum veocity reaches up to 147.8 km s^{-1}, here for the third method since there is NaD to Hα data point I used the nearest value. For the (PA=108°) observation there is a little rotation of Hα but not NaD. An offset ΔV of -60.8 for Hα from the center and 0.6 km s^{-1} offset of NaD relative to Hα measured. V_{max} of Hα reaches to 152 km s^{-1}.

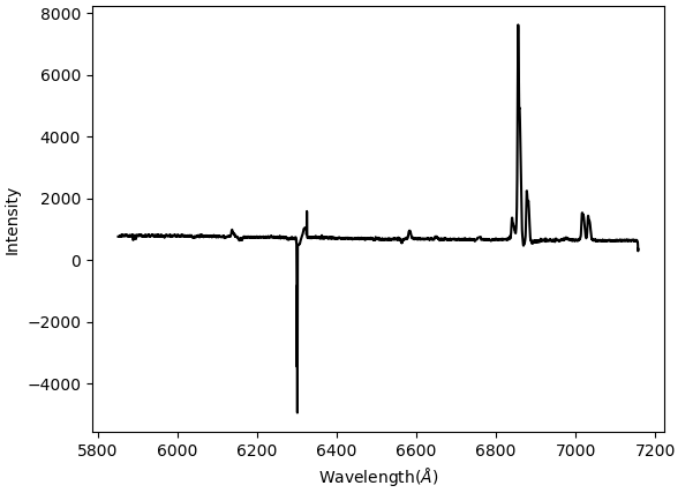

Figure A.4: integrated spectra of IRASF08520-6850[PA=108]

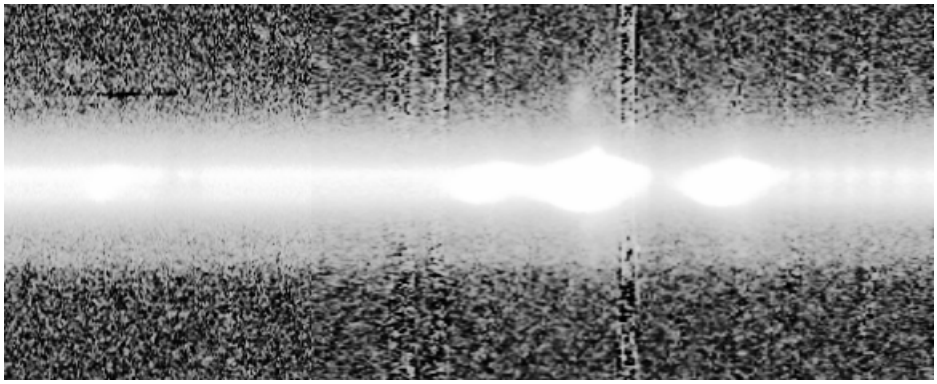

Figure A.5: 2D spectra of IRASF08520-6850[PA=108]

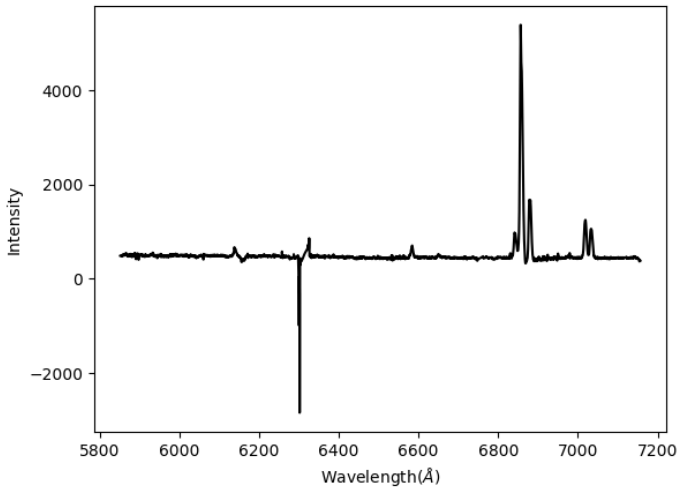

Figure A.6: integrated spectra of IRASF08520-6850[PA=50]

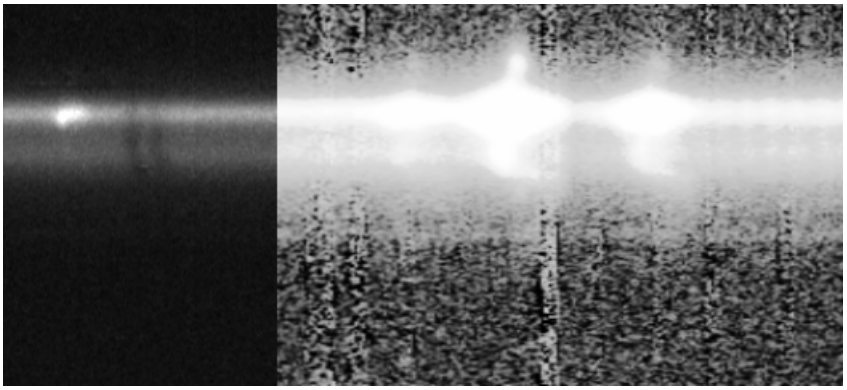

Figure A.7: 2D spectra of IRASF08520-6850[PA=50]. Note: different color brighness used to have visible NaID lines.

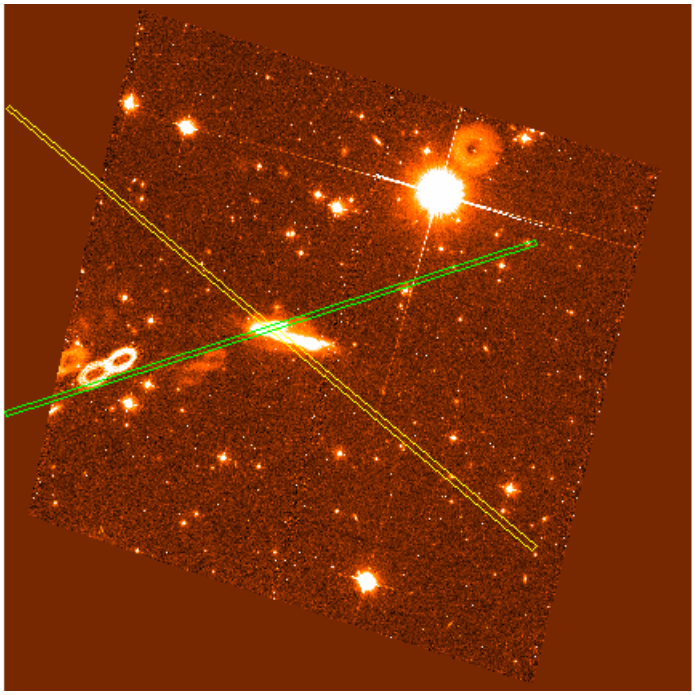

Figure A.8: IRASF08520-6850[PA=50](yellow) and [PA=108](green)

- **NGC2369** is a galaxy in a group of galaxies with IR luminosity $\log(L_{IR}/L_{\odot}=11)$ at $D_L\sim$45 Mpc. The slits were positioned at (PA=350°) along the major axis and (PA=250°) along the minor axis respectively, see A.13. The major axis observation shows a rotation with ΔV of NaD $\sim$3 km s^{-1} and V_{max} of Hα 301 km s^{-1}, see rotation curve 3.4.12. The minor axis measurement has an offset of 114 km s^{-1} and its Hα V_{max} reaches 206 km s^{-1}, see rotation curve 3.4.4.

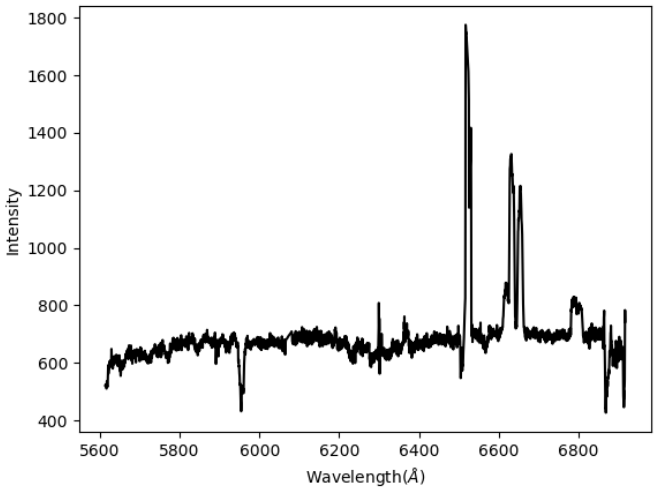

Figure A.9: integrated spectra of NGC2369[PA=350]

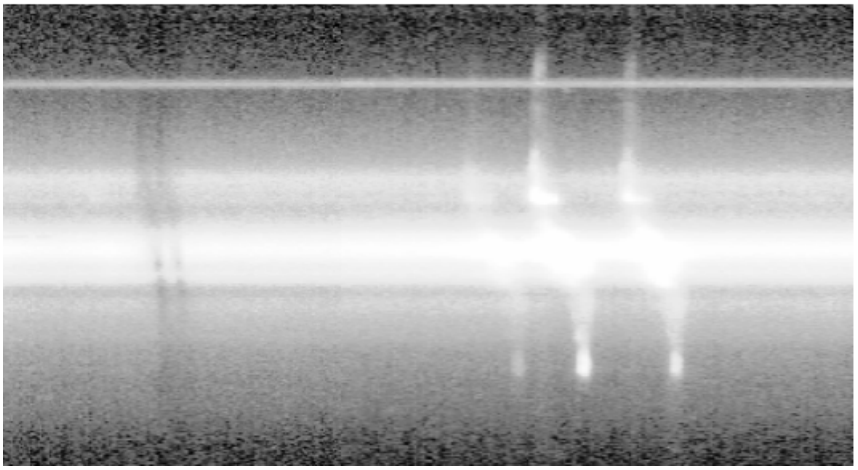

Figure A.10: 2D spectra of NGC2369[PA=350]

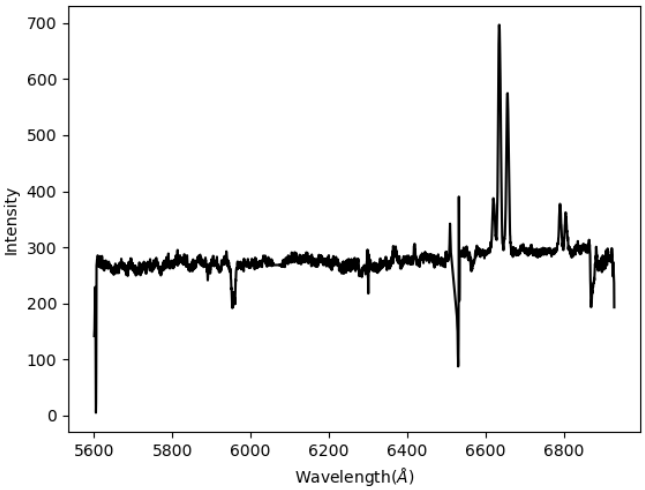

Figure A.11: integrated spectra of NGC2369[PA=250]

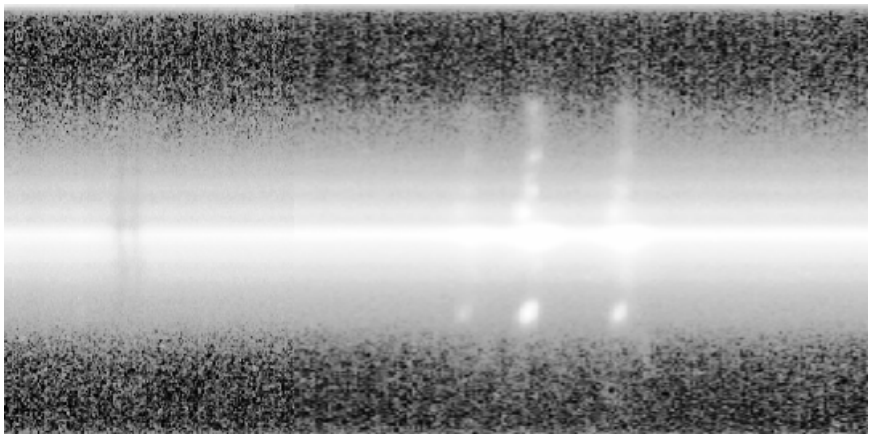

Figure A.12: 2D spectra of NGC2369[PA=250]

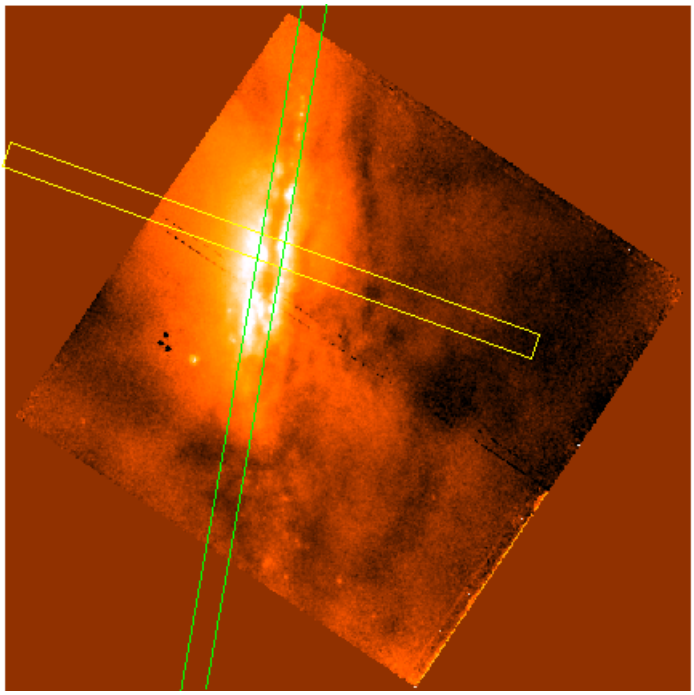

Figure A.13: NGC2369[PA=350](green) and NGC2369[PA=250](yellow)

- **NGC3508** is an Emission line galaxy (EMG) with IR luminosity $\log(L_{IR}/L_{\odot}=10.9)$ at a luminosity distance of D_L∼54Mpc. It is a major axis observation as shown on A.16, where a clear Hα seen and followed by short(∼1 Kpc) NaD compared to Hα which extends up to 29 Kpc. NaD offset from Hα by ∼-4 km s^{-1} and Hα offset from the center by 22 km s^{-1}. The V_{max} of H_{α} reaches up to 185 km s^{-1}, see rotation curve 3.4.10.

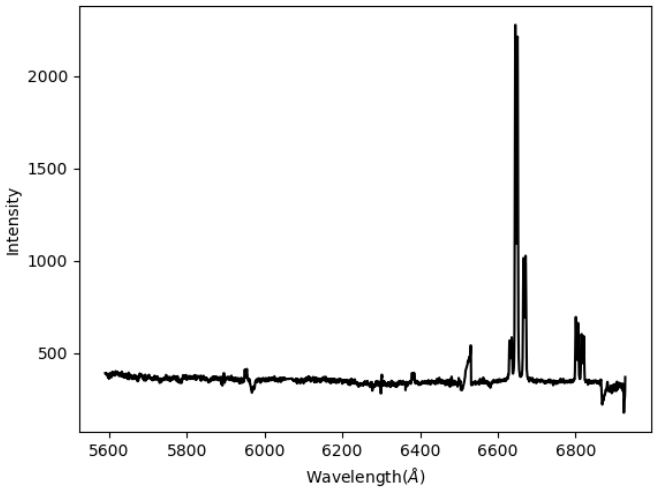

Figure A.14: integrated spectra of NGC3508

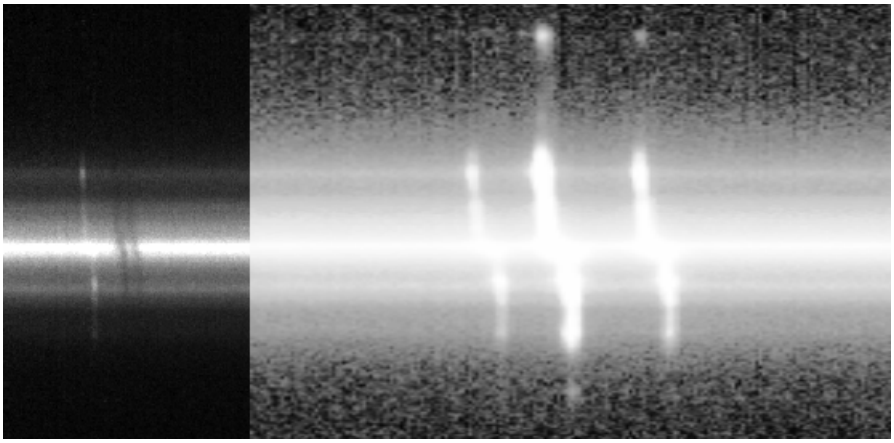

Figure A.15: 2D spectra of NGC3508. Note: different color brighness used to have visible NaID lines.

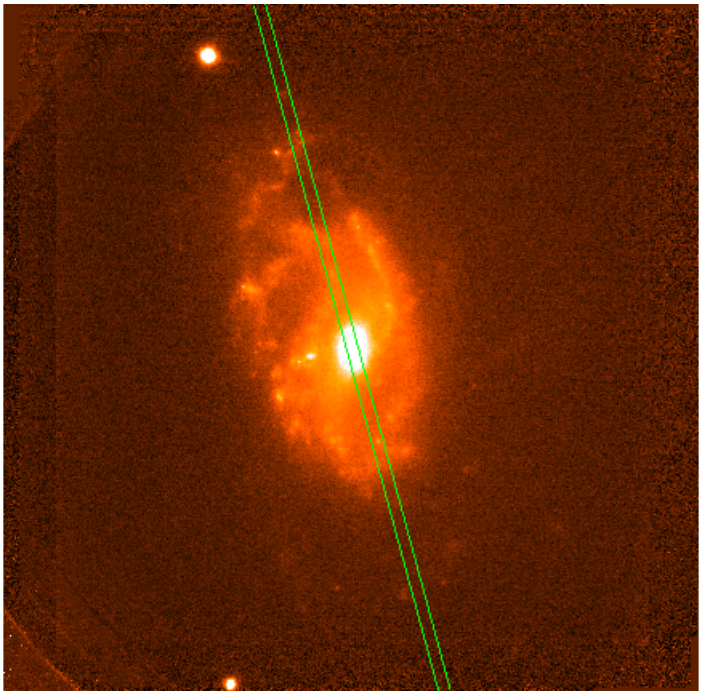

Figure A.16: NGC3508[PA=15]

- **CGCG049-057** is a LIRG with IR luminosity $\log(L_{IR}/L_{\odot}=11)$ at luminosity distance $D_L \sim 54$ Mpc. It has two observations where the slits positioned at (PA=0°) close to minor and (PA=199°) close to major axis positions. In both observations Hα shows a clear rotation. The minor axis observation (PA=0°) shows rotation of NaD but (PA=199°) is not clear, see the rotation curve 3.4.19 and 3.4.3. When one see the rotation curve, NaD is located close to the systemic velocity, this might indicate about the origin of the cool gas, here one can expect from nuclear region. The minor and major axis observations have NaD offset ΔV of 8 and 15 km s^{-1} respectively. Hα is also offset by 38 km from the systemic velocity. The V_{max} of Hα reaches

109 km s^{-1}.

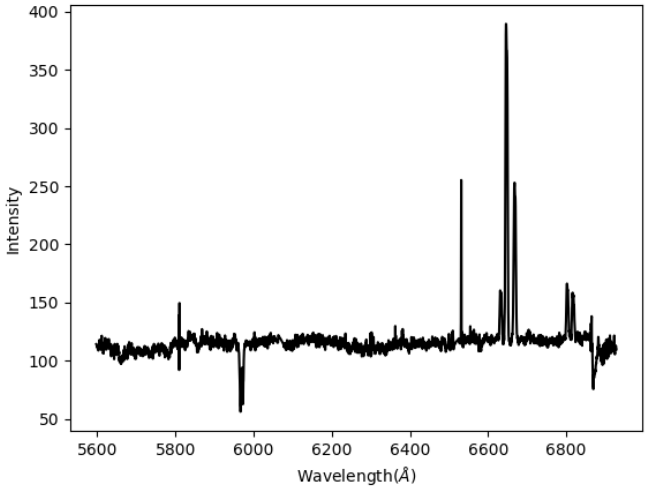

Figure A.17: integrated spectra of CGCG049-057[PA=0]

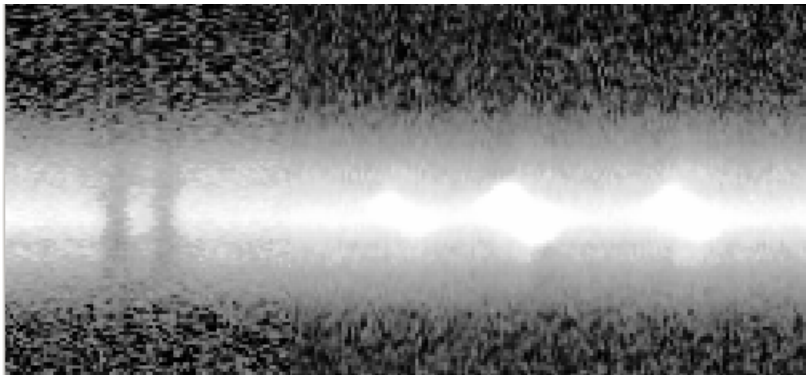

Figure A.18: 2D spectra of CGCG049-057[PA=0]

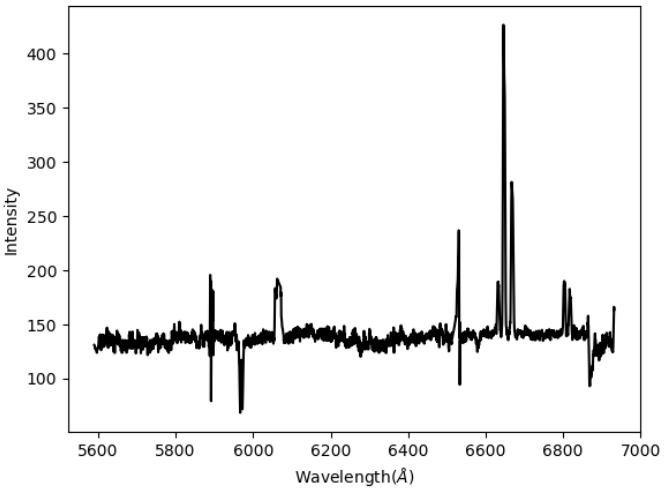

Figure A.19: integrated spectra of CGCG049-057[PA=199]

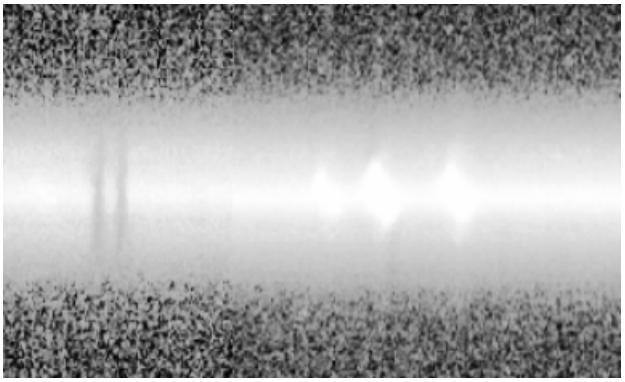

Figure A.20: 2D spectra of CGCG049-057[PA=199]

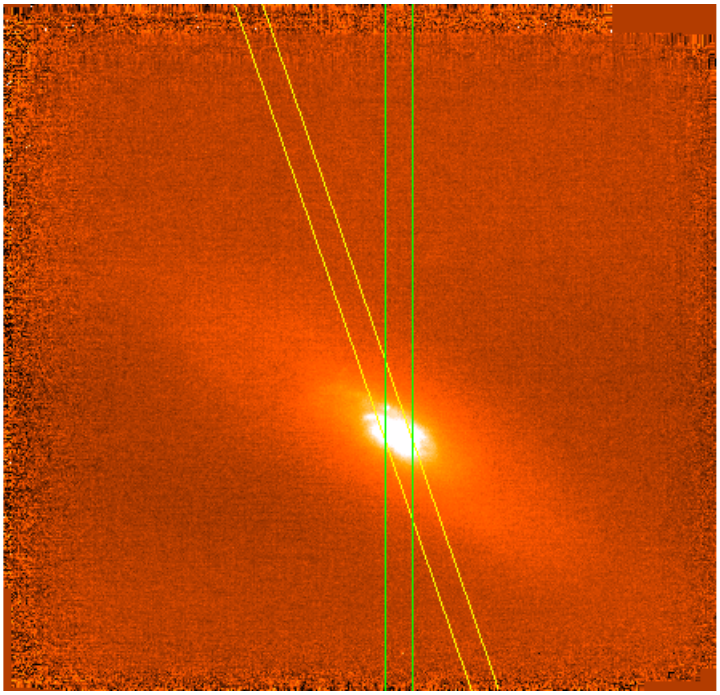

Figure A.21: CGCG49-057[PA=0](Green) and CGCG49-057[PA=199(yellow)]

- **ESO320-G030** is an isolated LIRG with HII regions as reported by Alonso-Herrero et al. (2006). The slits were aligned at (PA=135°) along the major axis and at (PA=90°) along the minor axis, see A.26. Also see the 1D and 2d spectra A.22 and A.23. In both observations, the rotation of both Na and Hα can be seen. Here NaD following Hα the origin of the outflow is from the disk. NaD follows with the shape of Hα, where Hα also offset by 43.7 km s^{-1} from the center of the galaxy. The major and minor axis observation has offset velocities -17 and 36 km s^{-1} respectively. And Hα has a V_{max} reaches up to 242 and 209 for the minor and major axis observations respectively, see rotation curve 3.4.1 and 3.4.15.

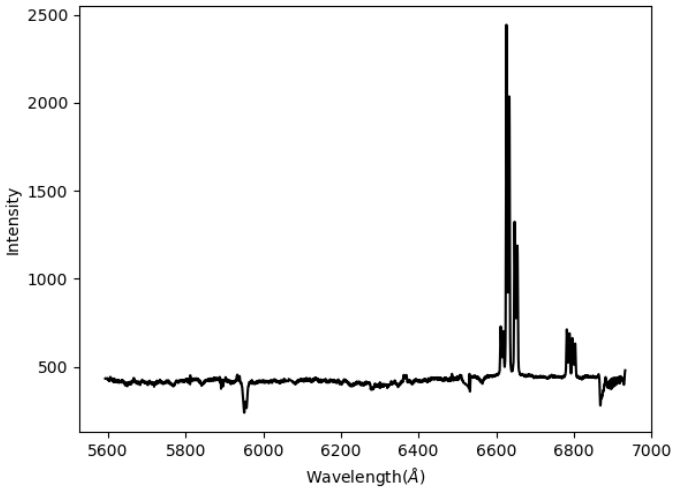

Figure A.22: integrated spectra of ESO320-G030[PA=135]

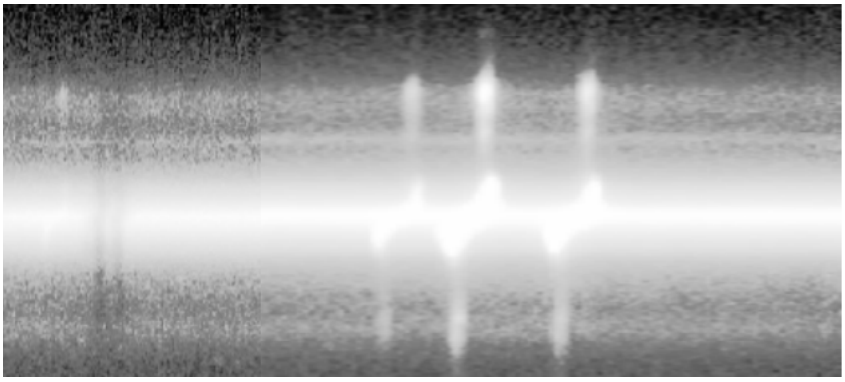

Figure A.23: 2D spectra of ESO320-G030[PA=135]

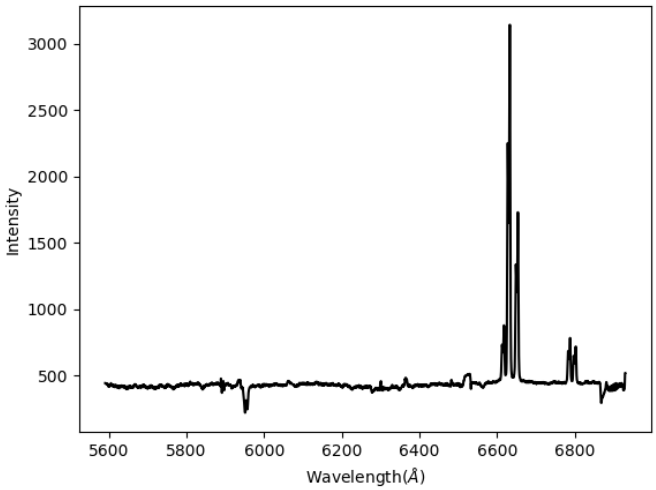

Figure A.24: integrated spectra of ESO320-G030[PA=90]

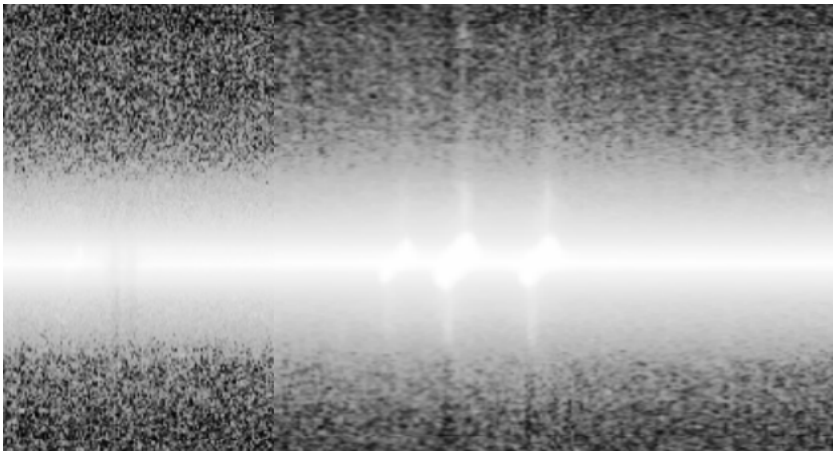

Figure A.25: 2D spectra of ESO320-G030[PA=90]

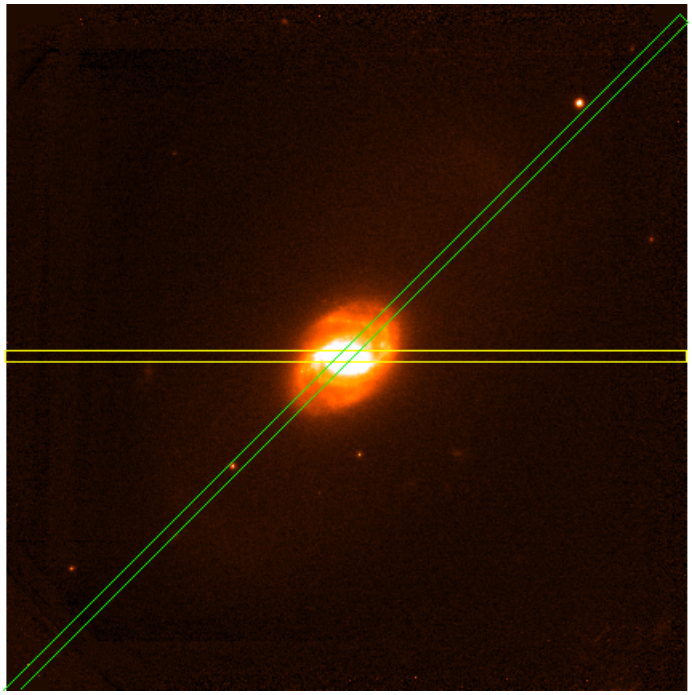

Figure A.26: ESO320-G030[PA=90](yellow) and ESO320-G030[PA=135](green)

- **IRASF01364-1042** is a LINER type Active Galaxy Nucleus (AGN) galaxy with IR luminosity $\log(L_{IR}/L_{\odot}$=11.76) at a luminosity distance of D_L∼205.5 Mpc. It is nearly an edge on galaxy. The slit is aligned along the major axis at (PA=42°), see A.29 although there is no rotation of both Hα and NaD, see rotation curve 3.4.12. NaD is offset by 17 km s^{-1} relative to Hα. Hα also offset by 42 km s^{-1} from the center, and its V_{max} reaches up to 100 km s^{-1}.

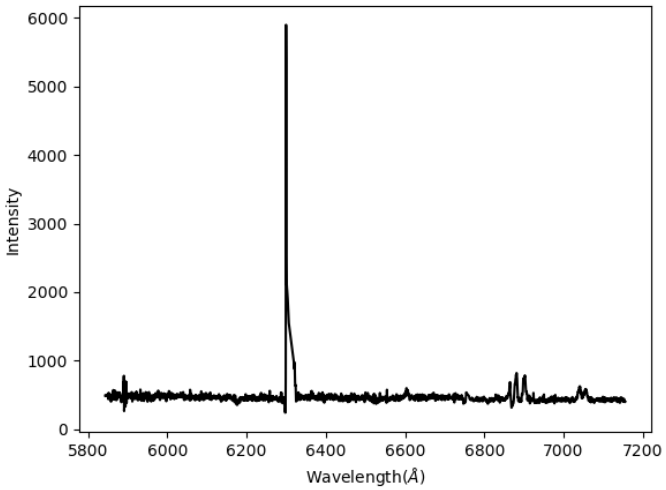

Figure A.27: integrated spectra of IRASF01364-1042

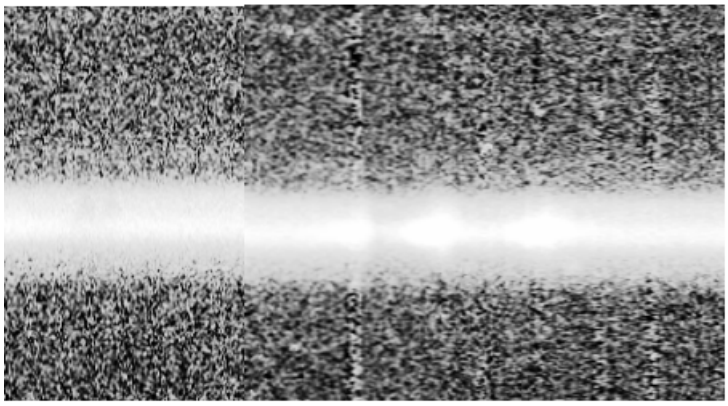

Figure A.28: 2D spectra of IRASF01364-1042

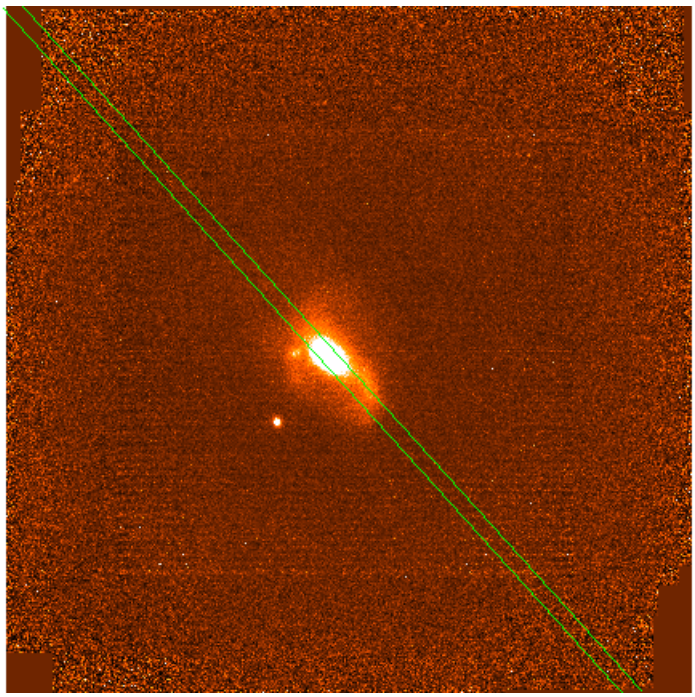

Figure A.29: IRASF01364-1042[PA=42]

- **IRAS 18293−3413** is a gas-rich spiral with an IR luminosity $\log(L_{IR}/L_{\odot}$=11.75) at a luminosity distance of D_L∼75Mpc. This galaxy is studied by Väisänen et al. (2008b) using AO imaging with the Very Large Telescope and long-slit NIR spectroscopy which was aimed to find dust-obscured core-collapse supernovae in the inner regions of LIRGs and to study star formation. It has two observations along the major axis (PA=128°) and the minor axis (PA=55°). The former is a major axis observation, see rotation curve 3.4.13, as it can be seen from the 2d image, both the cool neutral and ionized gas are in roatation. The V_{max} of Hα reaches up to 186 km s^{-1} and offset velocity of 19 km s^{-1} relative to the systemic velocity. There

is also a rotation of Hα for (PA=55°) observation which has a V_{max} of 217 km s^{-1} and has Na offset velocity of 50 km s^{-1}. There is an indication NaD seems following Hα, see rotation curve 3.4.2. Also from ∼10.5" - 12" the Hα emission disappeared. In this region strong absorption is observed, which shows the emission from Hα eaten by old cool stars.

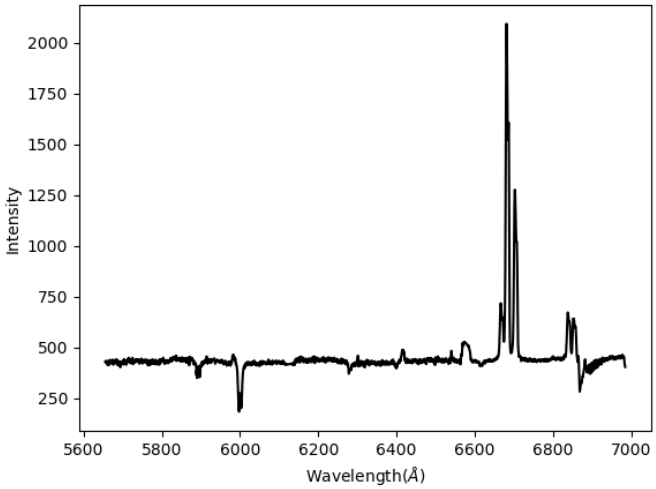

Figure A.30: integrated spectra of IRAS18293-3413[PA=128]

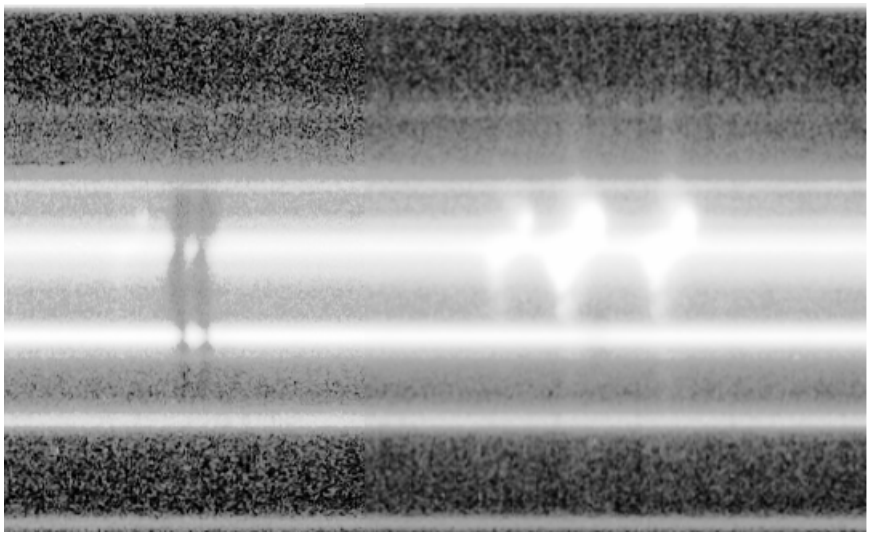

Figure A.31: 2D spectra of IRAS18293-3413[PA=128]

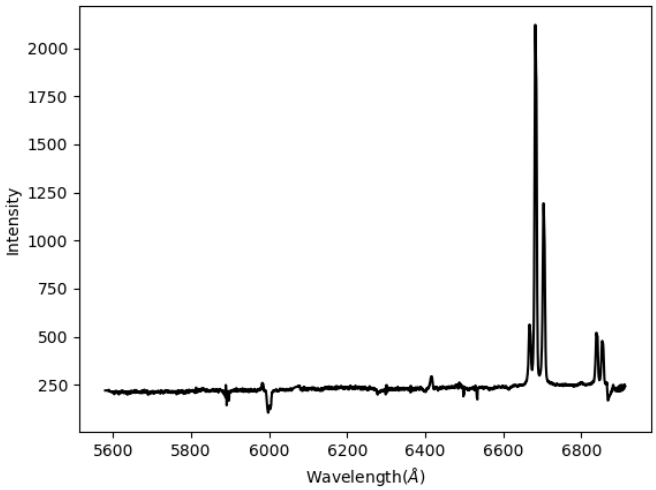

Figure A.32: integrated spectra of IRAS18293-3413[PA=55]

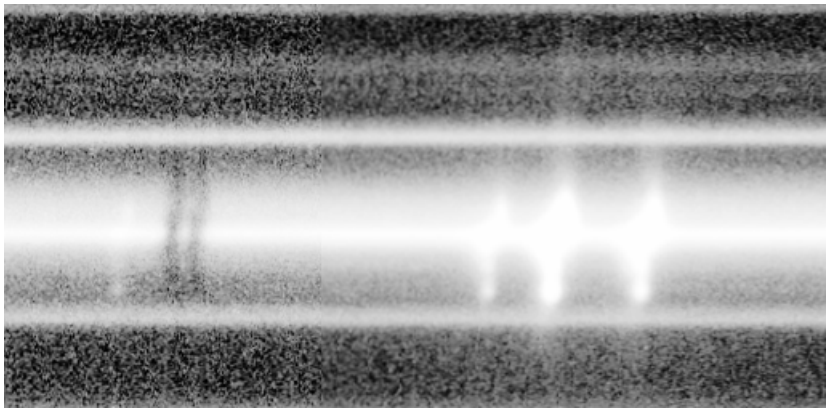

Figure A.33: 2D spectra of IRAS18293-3413[PA=55]

- **ESO550-IG025** is a pair of galaxies with IR luminosities $\log(L_{IR}/L_{\odot}=11.42)$, the bigger companion and $\log(L_{IR}/L_{\odot}=11.03)$, the smaller companion. The Northern companion (PA=219°) has a unusual Na rotation curve red-shifted from the systemic by -80 km s^{-1} as shown on the rotation curve 3.4.9. A normal line profile for both Hα and Na is seen, except broader line for Na. The redshift of Na is an unambiguous indicator of

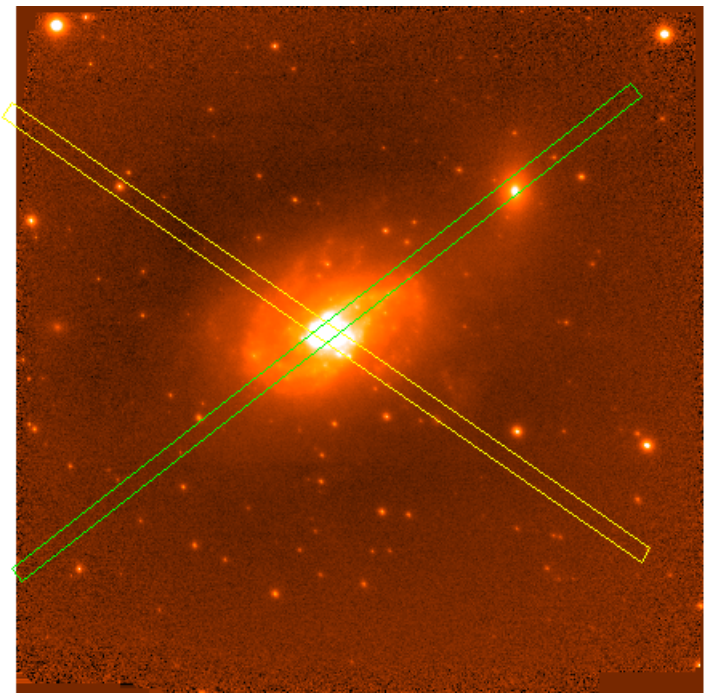

Figure A.34: IRAS18293-3413[PA=55](yellow) and [PA=128](green)

gas in-fall. The Southern companion (PA=242°) shows some rotation of both the cool and neutral gas reaching a V_{max} of Hα 236.5 km s^{-1} and also has an offset velocity 29 km s^{-1}, see the rotation curve 3.4.11. The position of the slits also shown on A.39.

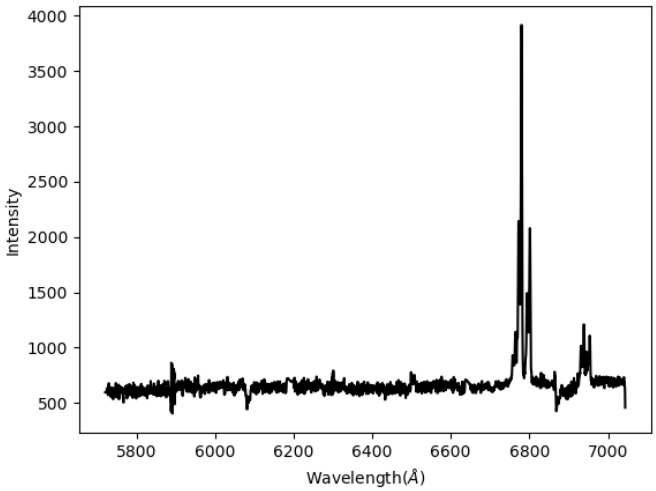

Figure A.35: integrated spectra of ESO550-IG025[PA=242]

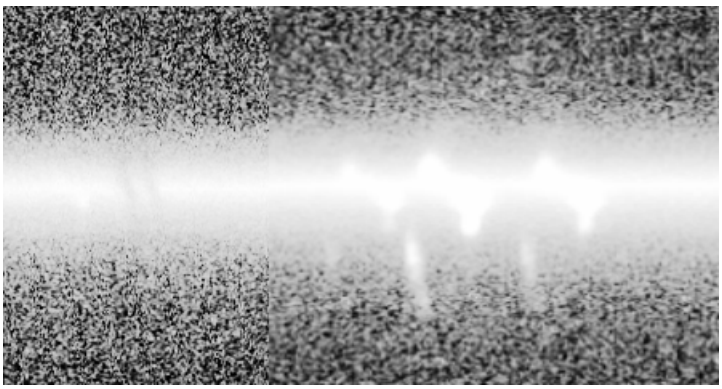

Figure A.36: 2D spectra of ESO550-IG025[PA=242]

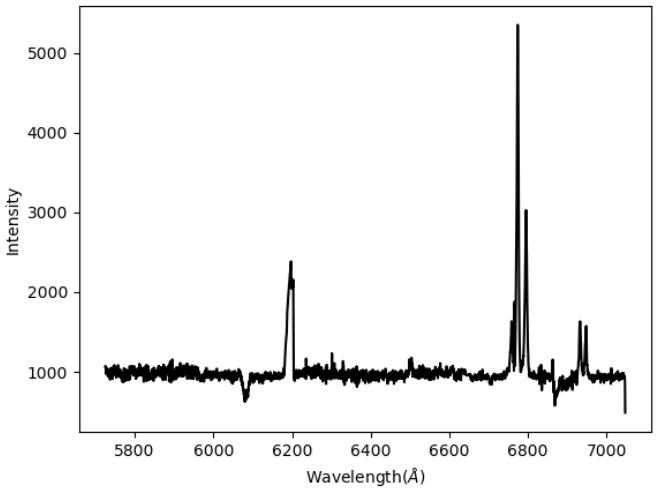

Figure A.37: integrated spectra of ESO550-IG025[PA=219]

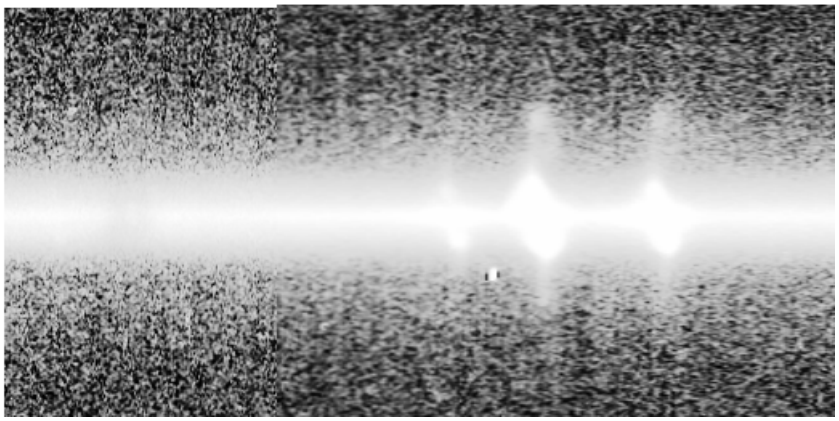

Figure A.38: 2D spectra of ESO550-IG025[PA=219]

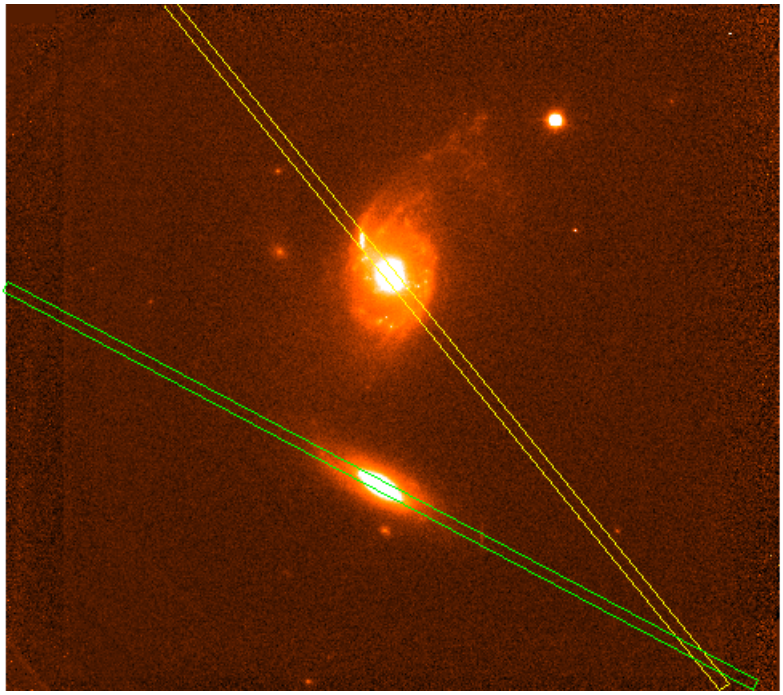

Figure A.39: ESO550-IG025[PA=242](green) and [PA=219](yellow)

- **ESO440-IG058** is a pair of LIRGs with IR luminosities $\log(L_{IR}/L_{\odot}=11)$ the Southern component bigger companion - observed along the major axis at (PA=57°) and Northern small component with $\log(L_{IR}/L_{\odot}=10.79)$ along the minor axis at (PA=245°), see A.44. The major axis observation although the slit does not cover the central region(offset from the center) shows rotation with red shifted Na relative to the systemic velocity and has an offset velocity -49.5 km s^{-1}, see rotation curve 3.4.16. The maximum velocity calculated from the systemic velocity is 226 km s^{-1}.The minor axis observation has a very weak Na D with an offset velocity 30 km s^{-1}, of course no rotation observed as shown on the rotation curve 3.4.23.

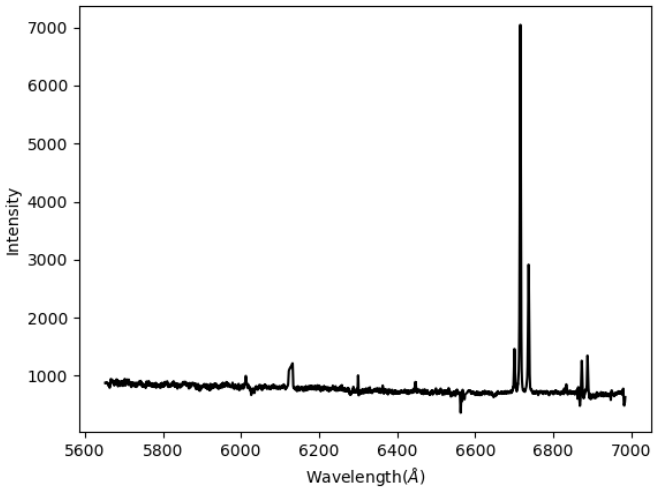

Figure A.40: integrated spectra of ESO440-IG058[PA=245]

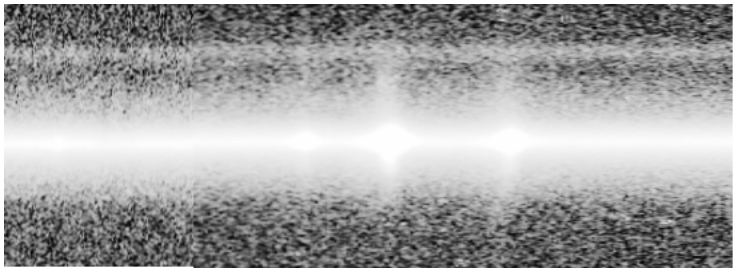

Figure A.41: 2D spectra of ESO440-IG058[PA=245]

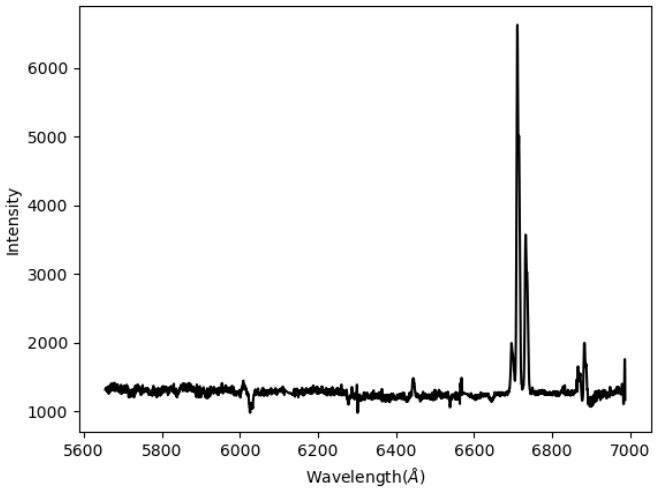

Figure A.42: integrated spectra of ESO440-IG058[PA=57]

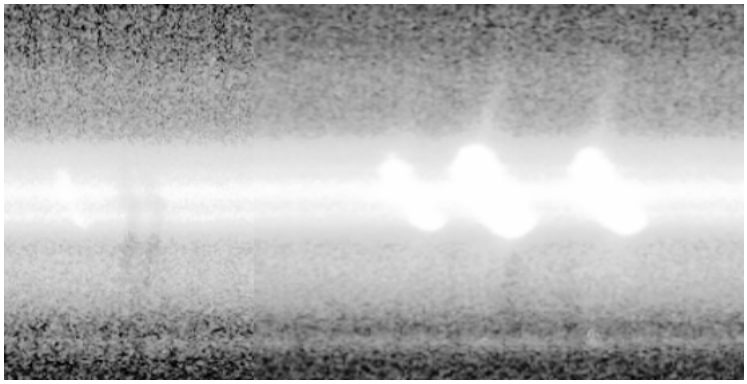

Figure A.43: 2D spectra of ESO440-IG058[PA=57]

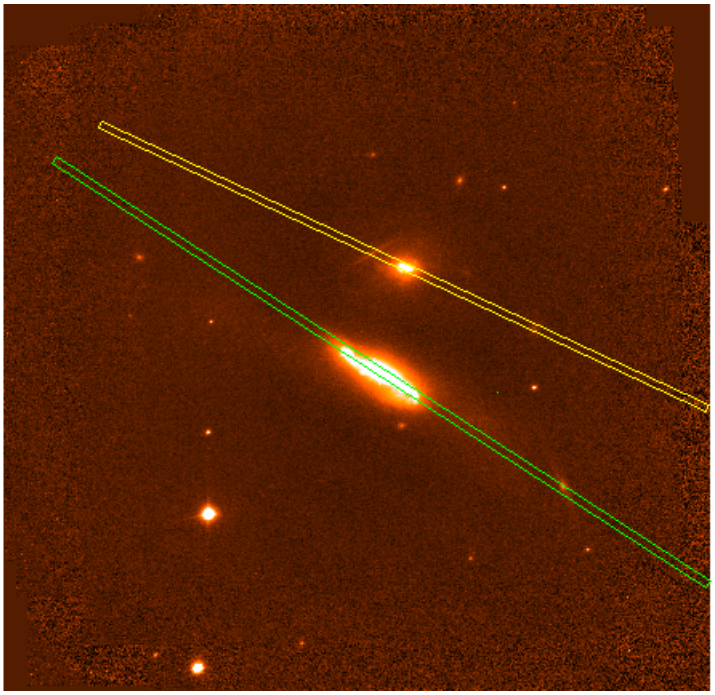

Figure A.44: ESO440-IG058[PA=245](yellow) and ESO440-IG058[57](green)

- **ESO267-G030** is a starburst galaxy with IR luminosity of $\log(L_{IR}/L_{\odot}$=11.2) at a luminosity distance of D_L∼77 Mpc. The observation is nearly along the major axis at (PA=135°), see A.47. The short Na line is due to very weak absorption.There is a clear rotation of Hα, Na seems following it but since the absorption line of Na is too short,so it seems difficult to be sure as shown on the rotation curve 3.4.21. The Na offset and maximum velocity of Hα are 31 km s^{-1} and 179.5 km s^{-1} respectively.

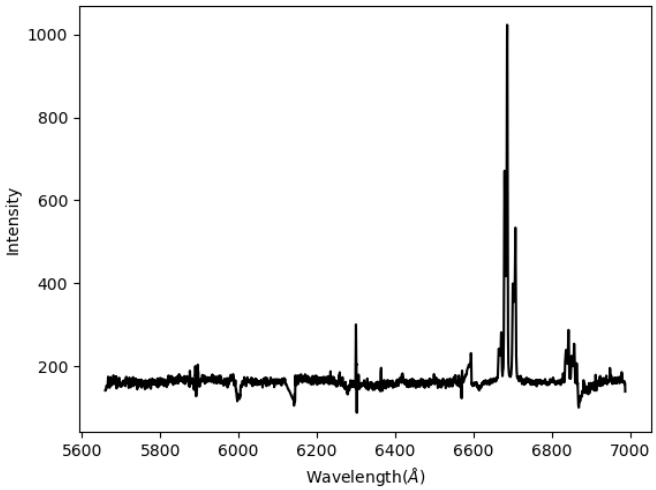

Figure A.45: integrated spectra of ESO267-G030

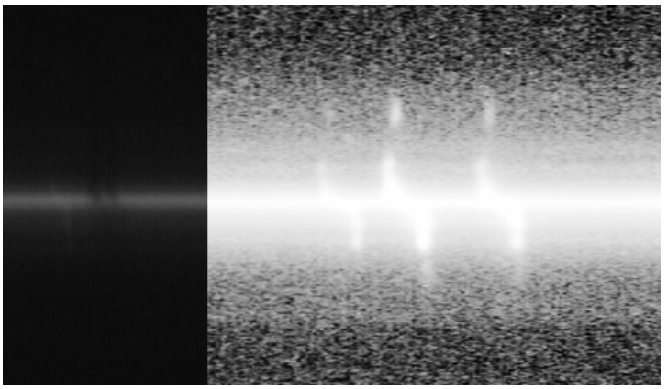

Figure A.46: 2D spectra of ESO267-G030

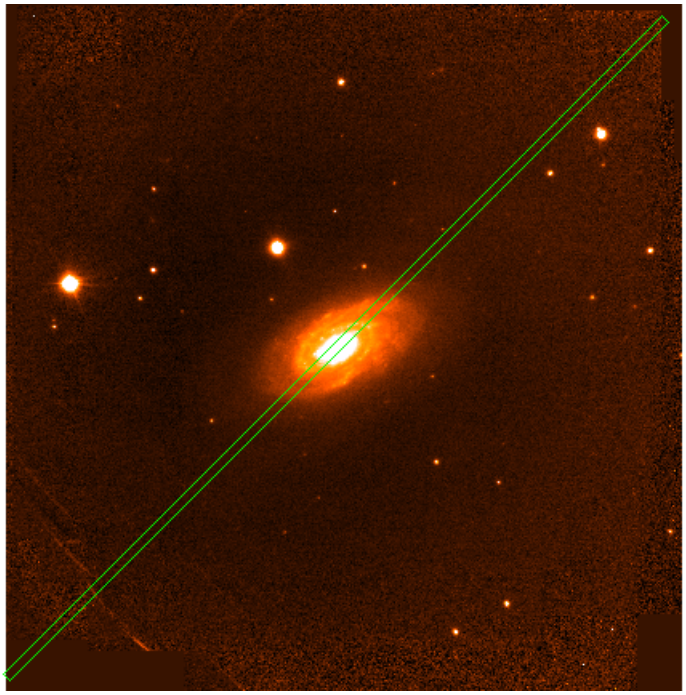

Figure A.47: ESO267-G030[PA=135]

- **NGC4433** is an edge on starburst galaxy and has the least IR luminosity $\log(L_{IR}/L_{\odot}$=10.87) out of our targets at a D_L∼38.6 Mpc. The slit positioned along the major axis at (PA=188°) a bit offset from the center, see A.50. A strong Hα emission which extends up to ∼ 9 Kpc is seen. The rotation of Hα reaches a V_{max} of 200 km s^{-1} and Na follows with some rotation and an offset velocity 36 km s^{-1}, see rotation curve 3.4.4.

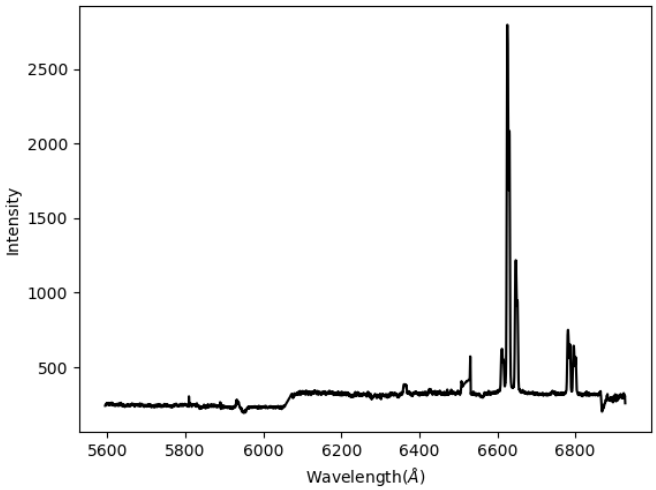

Figure A.48: integrated spectra of NGC4433

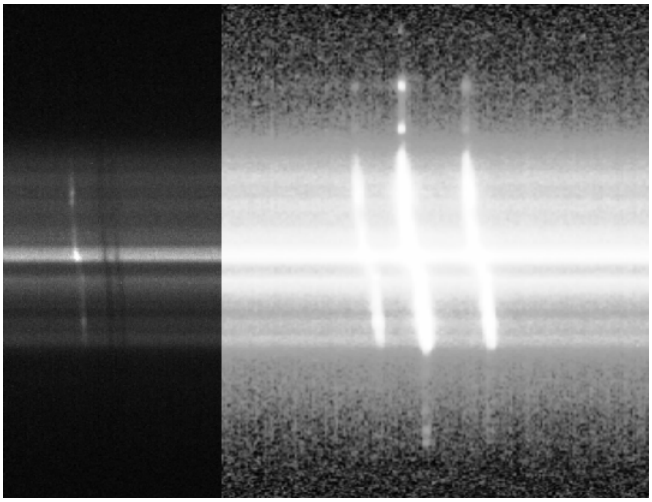

Figure A.49: 2D spectra of NGC4433

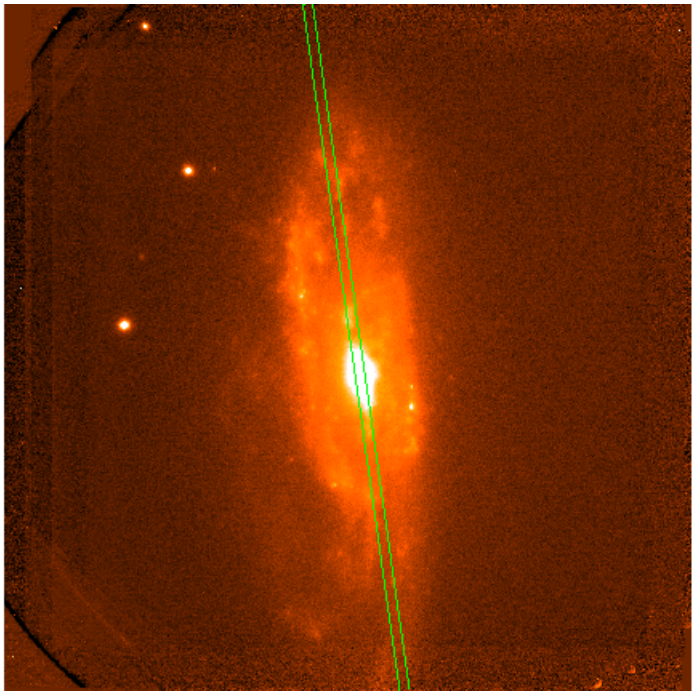

Figure A.50: NGC4433[PA=187.7]

- **MCG-02-33-098** is nearly edge on LIRG with a slit positioned at (PA=246°), see A.53. Na follows Hα with redshifted by -47 km s^{-1} and it covers up to 8 Kpc, see rotation curve 3.4.2.

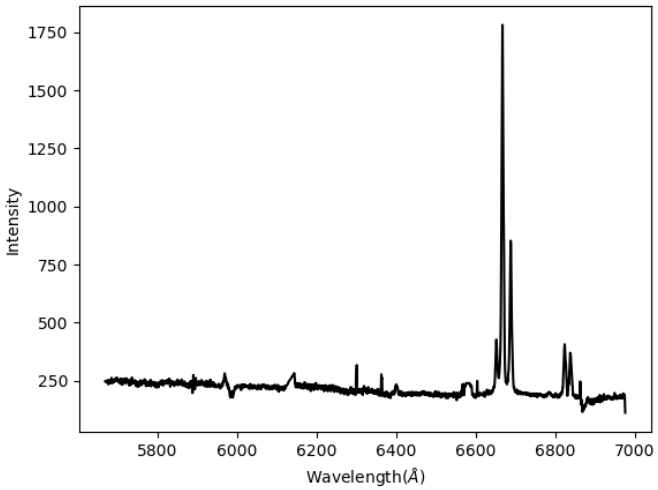

Figure A.51: integrated spectra of MCG-02-33-098

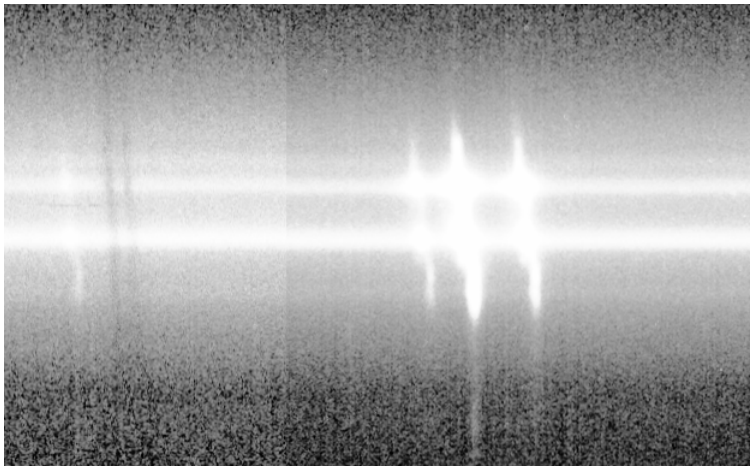

Figure A.52: 2D spectra of MCG-02-33-098

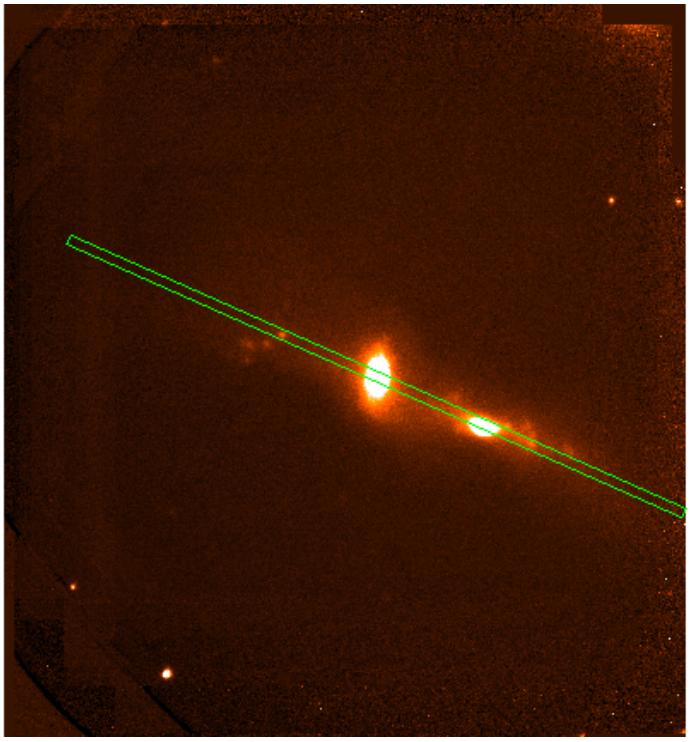

Figure A.53: MCG-02-33-098[PA=246]

- **ESO 154-G010** is an SBa-type barred spiral galaxy where its IR luminosity is not in IRASBG survey from Sanders et al. (2003) unlike the rest of our targets. Also at some point the NII[6583] line dominate over Hα which might be an indication of shock heating. There is rotation of Hα and Na seems to follow it with an offset velocity 48 km s^{-1}, see rotation curve 3.4.9. The V_{max} of Hα reaches 81 km s^{-1}.

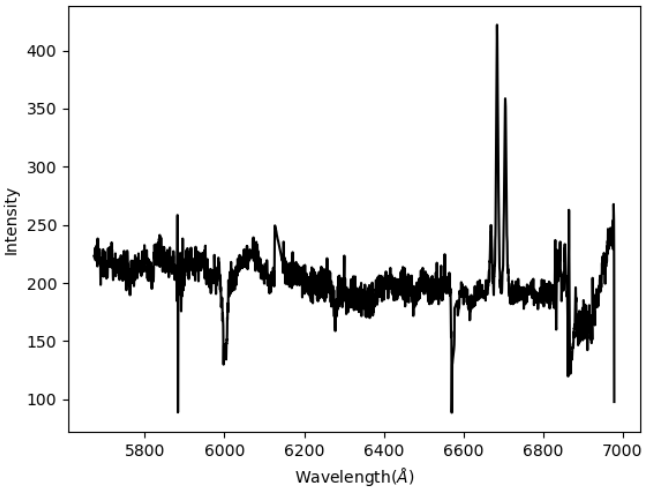

Figure A.54: integrated spectra of ESO 154-G010

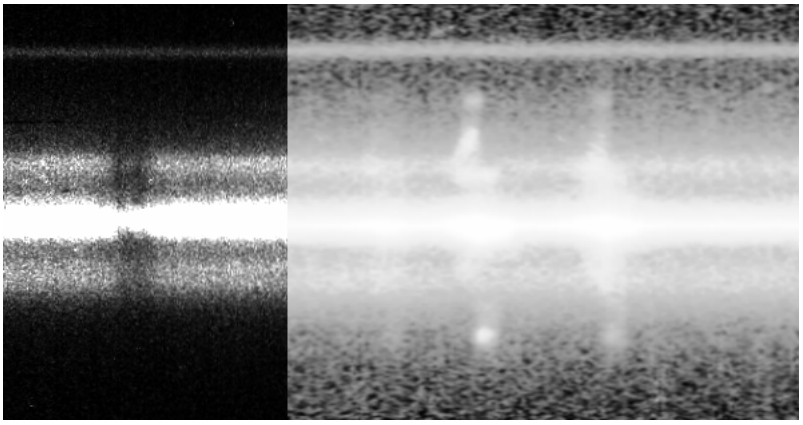

Figure A.55: 2D spectra of ESO 154-G010

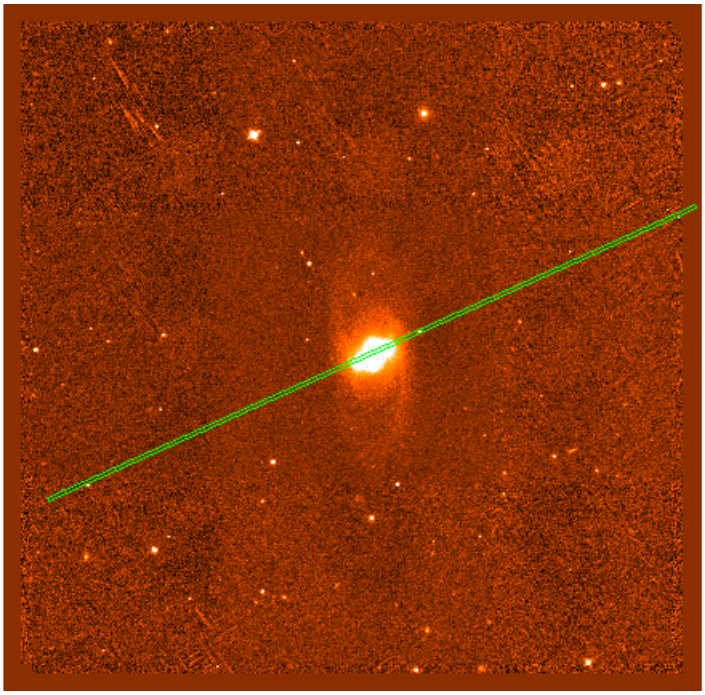

Figure A.56: ESO_154-G010[PA=24.5]

- **IRAS F17138−1017** is spiral galaxy with IR luminosity $\log(L_{IR}/L_{\odot}$=11.75) at a luminosity distance of D_L∼72 Mpc. The slit is positioned almost along the major axis at (PA=0°), see A.59. There is no a clear rotation seen though may be due to uncorrected inclination. As it can be seen on Figure 3.4.1 the Na D line is short due to very weak and short continuum. The Na line red shifted relative to systemic velocity with an offset of -48.8 km s^{-1} and has a maximum velocity of 127 km s^{-1}. As reported by Alonso-Herrero et al. (2006) the central region is obscured since its dominated by gas.

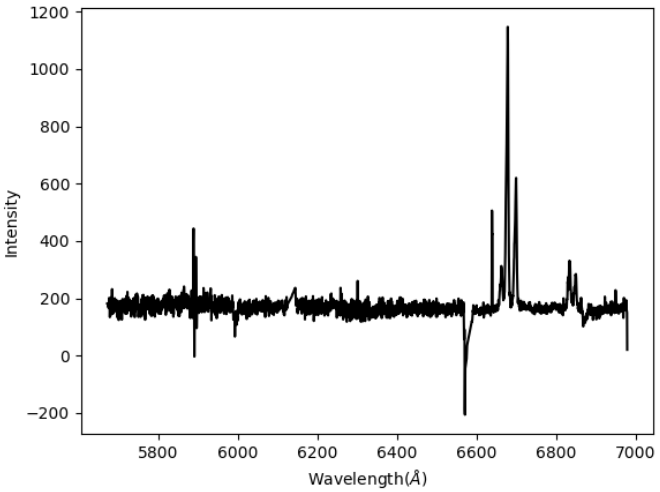

Figure A.57: integrated spectra of IRAS F17138−1017

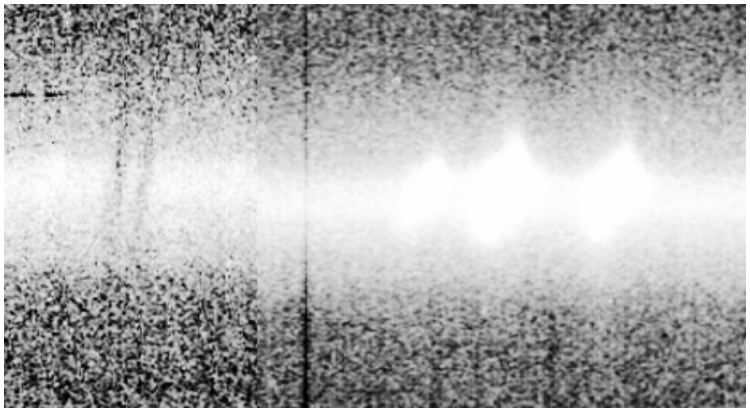

Figure A.58: 2D spectra of IRAS F17138−1017

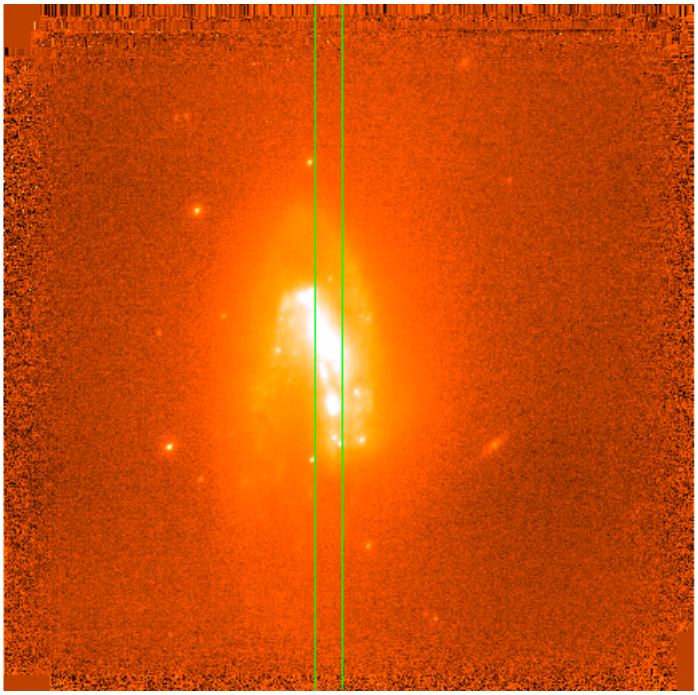

Figure A.59: IRASF17138-1017[PA=0]

- **ESO264-G057** is a starburst galaxy with an IR luminosity $\log(L_{IR}/L_{\odot}$=11.1) at D_L∼72 Mpc. The Na D line is very weak and short, as shown from the rotation curve 3.4.14. Na is blue shifted which indicates outflowing gas.Some rotation of Hα can be seen but no rotation of Na. The offset velocity of Na from Hα is 72 km s^{-1}. The slit positioned (PA=277°) along the minor axis, see A.62.

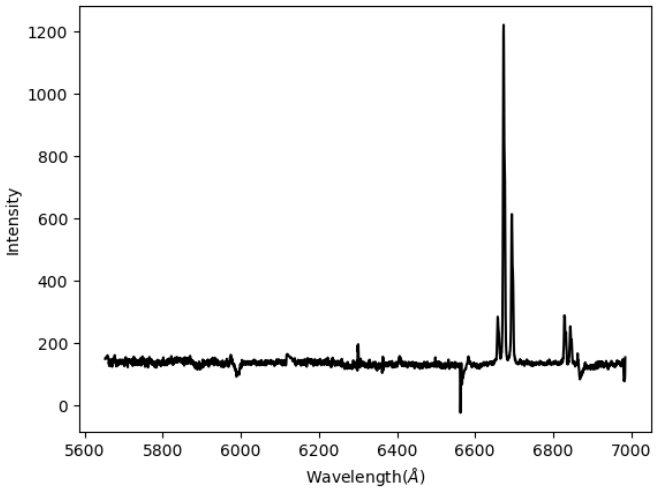

Figure A.60: integrated spectra of ESO264-G057

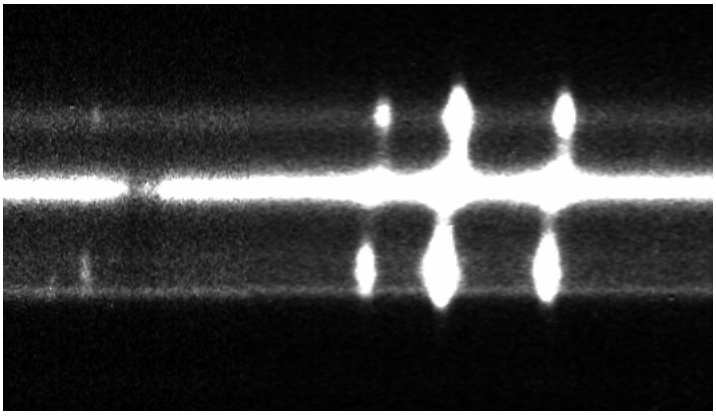

Figure A.61: 2D spectra of ESO264-G057

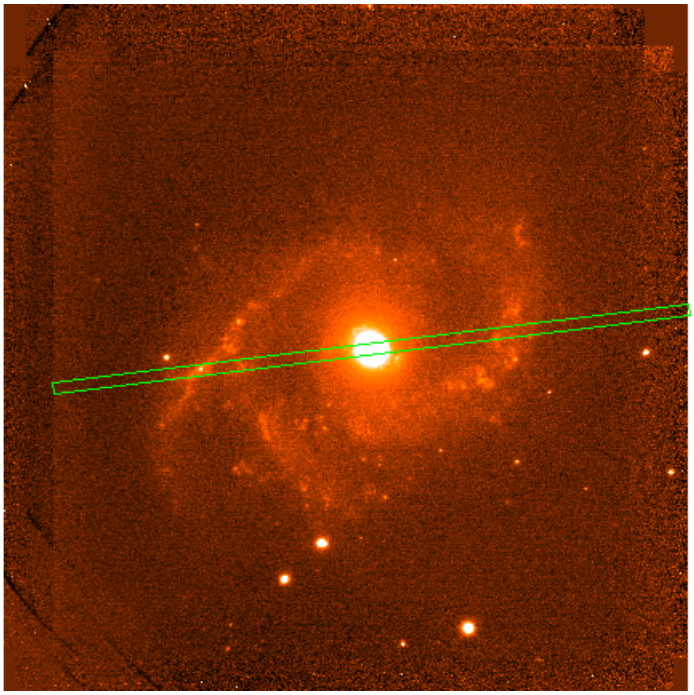

Figure A.62: ESO264G057[PA=277]

- **NGC 3110** is a LIRG which H II regions covering several kpc as pointed by Alonso-Herrero et al. (2006). It has IR luminosity $\log(L_{IR}/L_{\odot}=11)$ at $D_L\sim70$ Mpc. The three different slit positions were at (PA=185°),(PA=43.7°) and (PA=111°) as shown on A.69. As it can be seen Hα emission extends over 13 kpc. Observations at (PA=185°) and (PA=43.7°) are between major and minor axis that is why rotation is seen with an offset velocities of 79 and 95 km s^{-1} respectively, see the rotation curve 3.4.11 and 3.4.8. The minor axis observation(PA=111°) has a big offset 111.5 km s^{-1}, which implies a lot of material is outflowing, see rotation curve 3.4.28.

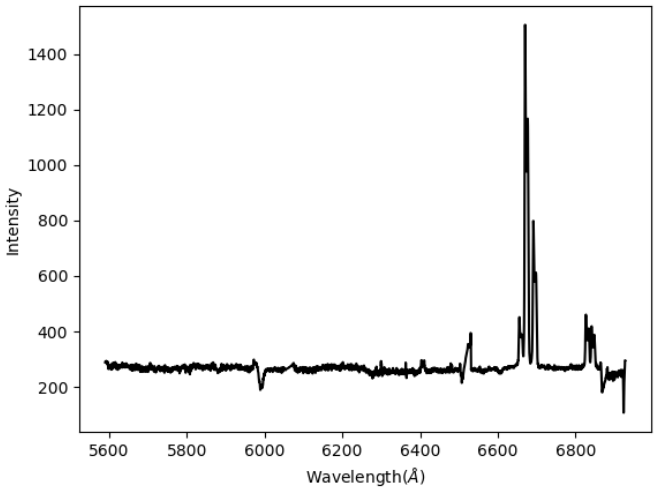

Figure A.63: integrated spectra of NGC 3110[PA=185]

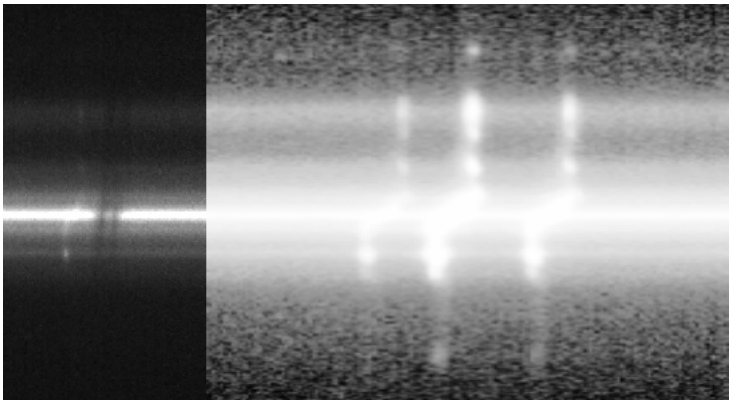

Figure A.64: 2D spectra of NGC 3110[PA=185]

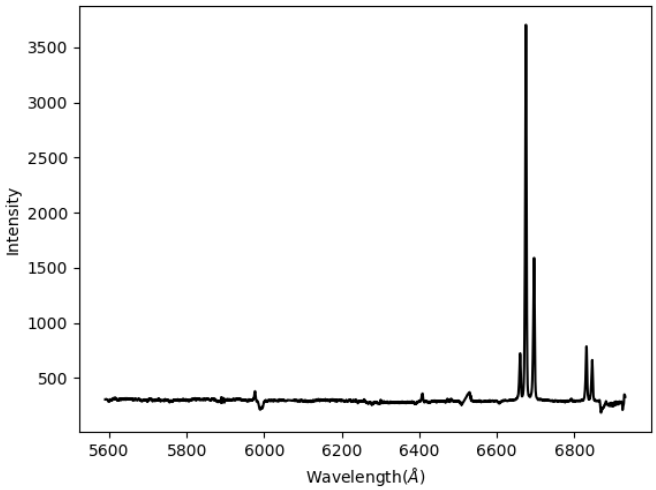

Figure A.65: integrated spectra of NGC 3110[PA=111]

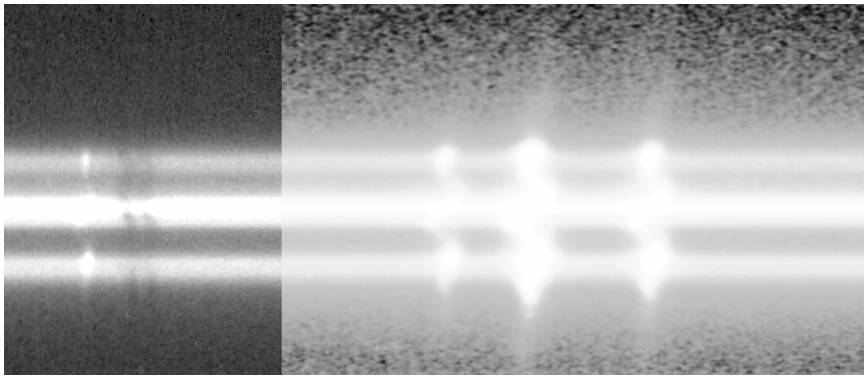

Figure A.66: 2D spectra of NGC 3110[PA=111]

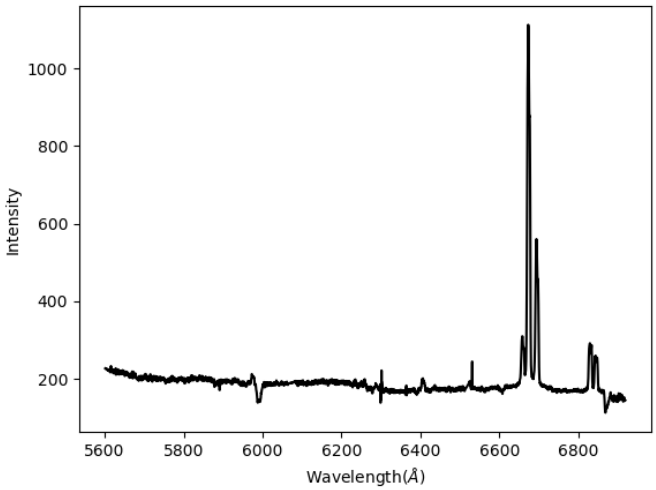

Figure A.67: integrated spectra of NGC 3110[PA=43.7]

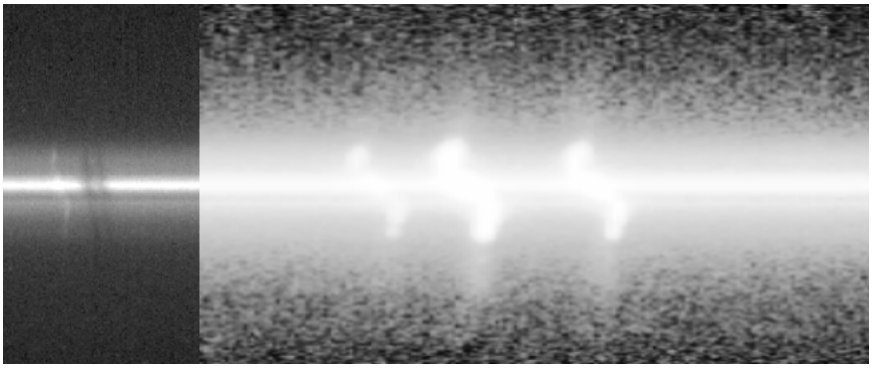

Figure A.68: 2D spectra of NGC 3110[PA=43.7]

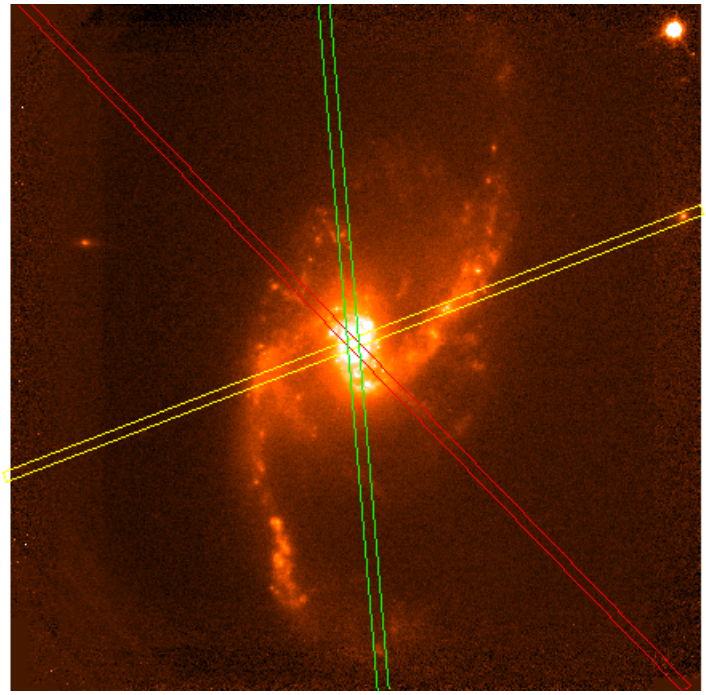

Figure A.69: NGC3110[PA=185](green),NGC3110[44](red) and NGC3110[111](yellow)

- **IC4280** is a starburst galaxy with an IR luminosity $\log(L_{IR}/L_{\odot}$=11.1) at D_L∼68Mpc. As it can be seen from the rotation curve on rotation curve 3.4.25, the Na is following ionized gas Hα, though there is an offset velocity of 88 km s^{-1} between them. The position of the slit was positioned at (PA=29°), see A.72.

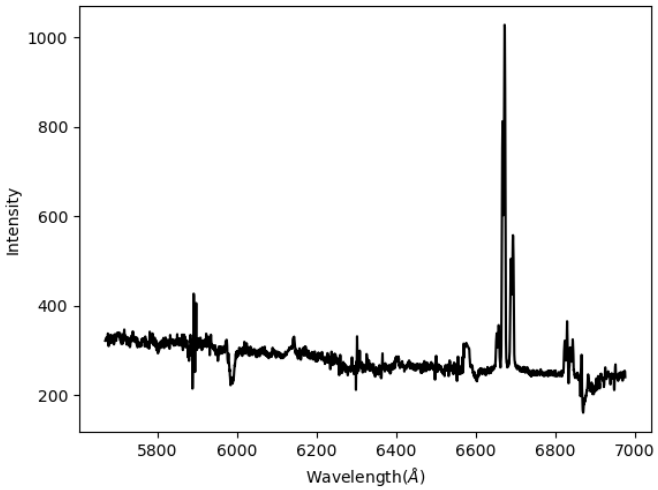

Figure A.70: integrated spectra of IC4280

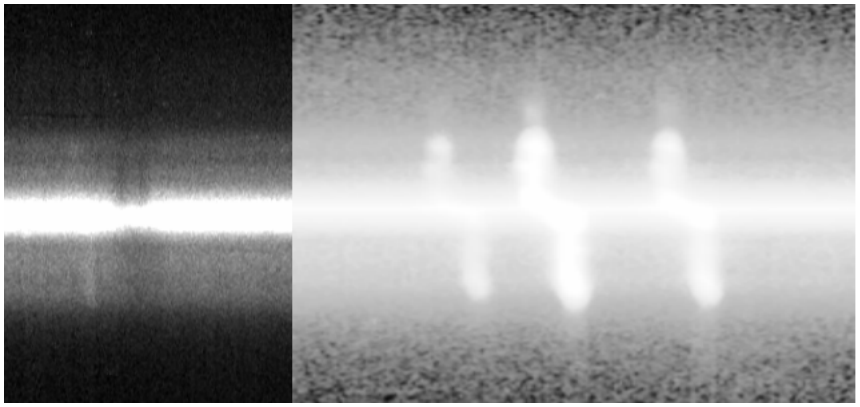

Figure A.71: 2D spectra of IC4280

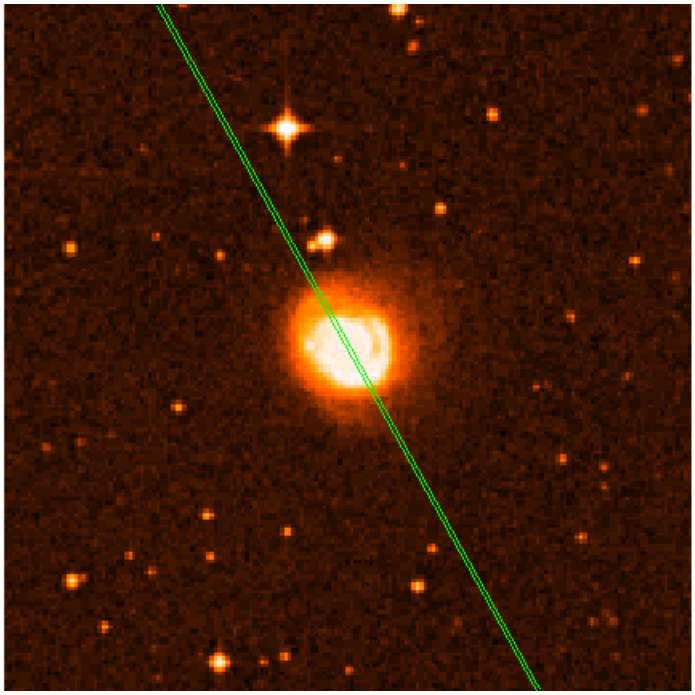

Figure A.72: I42C80[PA=29]

- **NGC1204** is a Seyfert 2 galaxy with $\log(L_{IR}/L_{\odot}$=11.88) and luminosity distance D_L∼64Mpc. There are two data-sets from two dates, 2012 and 2013. Both slits were aligned along the major axis the 2012 data at an angle (PA=73°) and the 2013 data at angle (PA=253°), see A.77. Na shows a sort of following the rotation of Hα but redshifted which indicates inflowing gas. For NGC1204(PA=73) Na is offset from Hα by 99.5 km s^{-1} and the V_{max} of Hα is 190 km s^{-1}. In case of NGC1204(PA=253) Na has an offset of 101kms^{-1} and has a V_{max} of Hα 180 km s^{-1}, see the rotation curve 3.4.5 and 3.4.6

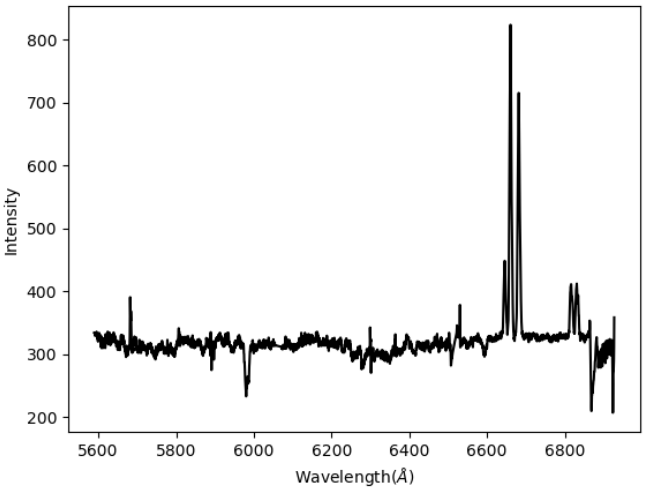

Figure A.73: integrated spectra of NGC1204[PA=73]

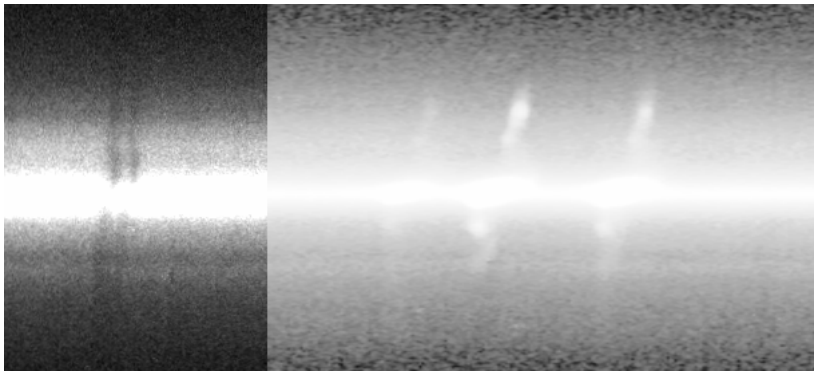

Figure A.74: 2D spectra of NGC1204[PA=73]

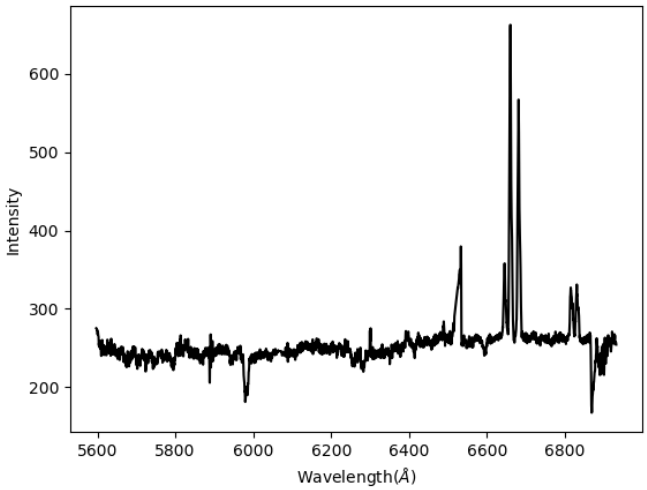

Figure A.75: integrated spectra of NGC1204[PA=253]

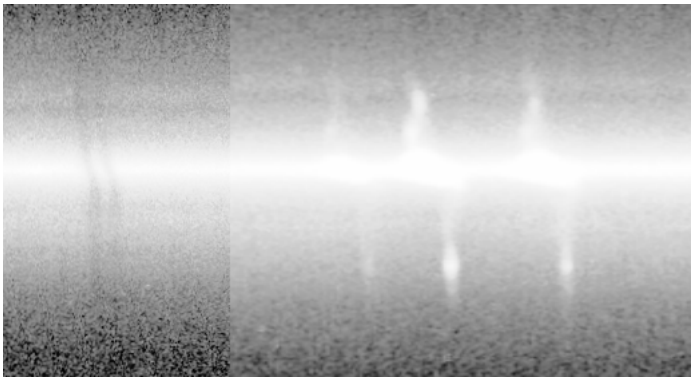

Figure A.76: 2D spectra of NGC1204[PA=253]

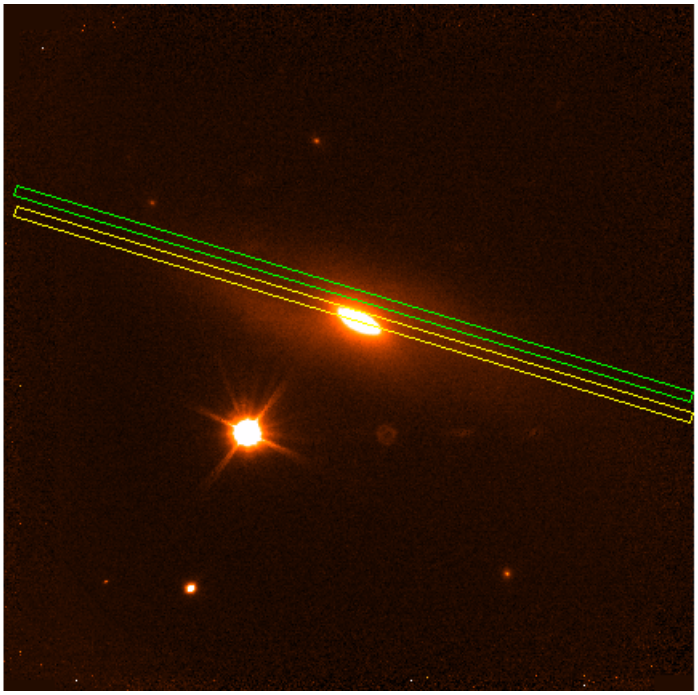

Figure A.77: NGC1204-N[PA=73](green) and NGC1204-S [PA=253](yellow).The offset for NGC1204-S [PA=253] is for clarity to show the two slits separately

- **NGC1819** is SBO type galaxy in group of clusters(GIC) has a lot of star clusters as studied by Sanders et al. (2003). It has an IR luminosity $\log(L_{IR}/L_{\odot}$=10.9) at $D_L\sim$ 61.9 Mpc. There were two observations where the slits positioned along the bar at (PA=125°) and at (PA=225°), see A.82. Here the position angle of the galaxy (PA_{gal}) of 2MASS measurement is 120°. But since our interest is the central region of the galaxy, the major axis from inside of the galaxy is the direct opposite of from the outside, i.e the major axis from the inside is the minor axis to the outer side and vice versa. In both measurements Hα rotation is seen, where NGC1819 (PA=125°) has NaD offset of 128 and NGC1819 (PA=125°) is offset by 111 km s^{-1} relative to V_{sys}. There is an indication NaD co-rotate with the same as Hα. Both have big offset velocities 138 km s^{-1} and 111 km s^{-1} along the major and minor axis respectively shown on it's rotation curve 3.4.6. The major axis observation(PA=125°) showed a NaD offset velocity greater than V_{esc} and reach beyond the potential well to enrich the IGM, see section 4.4, see also the rotation curve 3.4.8.

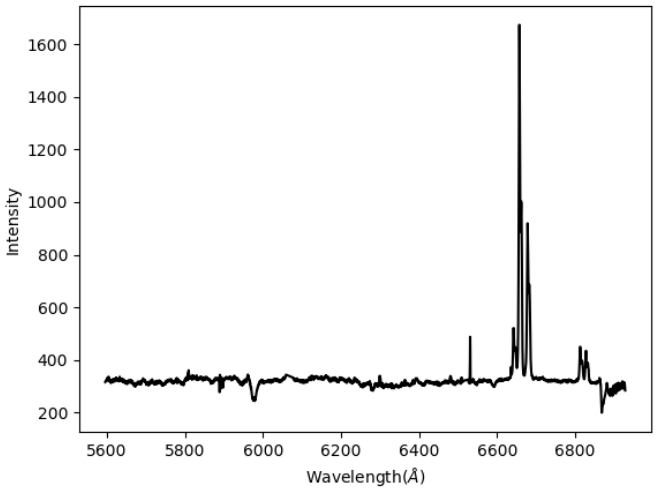

Figure A.78: integrated spectra of NGC1819[PA=225]

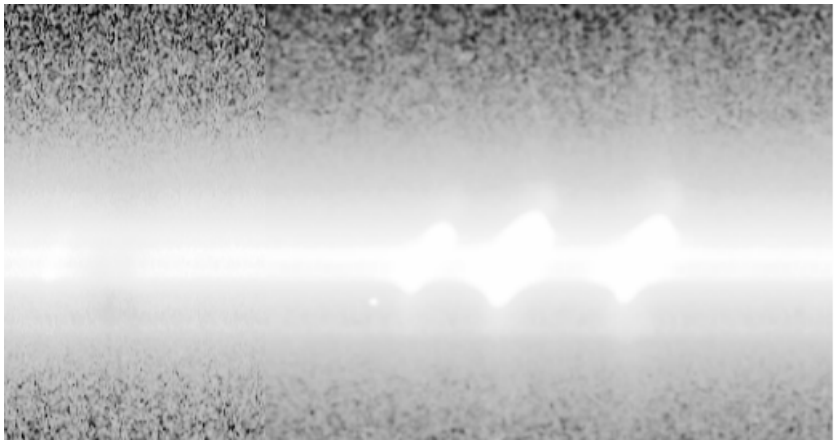

Figure A.79: 2D spectra of NGC1819[PA=225]

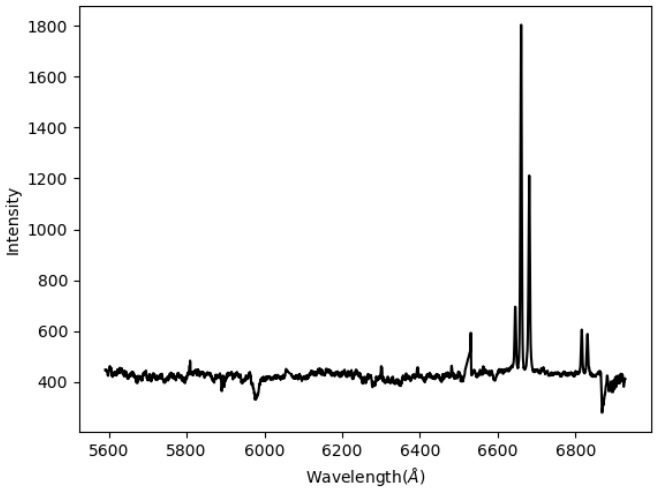

Figure A.80: integrated spectra of NGC1819[PA=125]

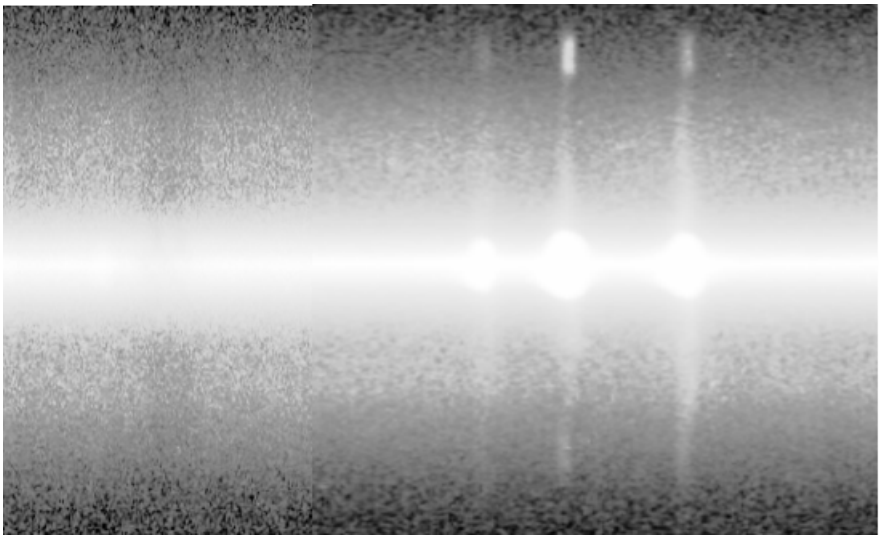

Figure A.81: 2D spectra of NGC1819[PA=125]

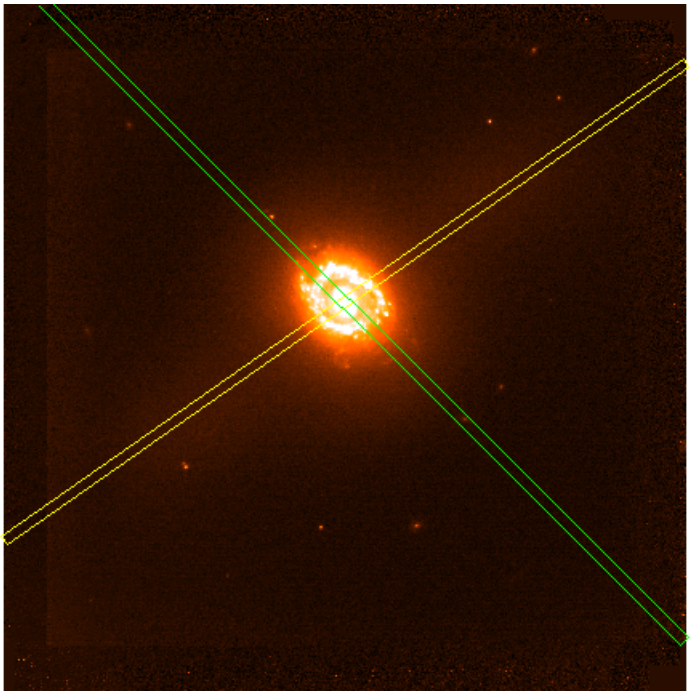

Figure A.82: NGC1819[225](green) and NGC1819[125](yellow)

- **ESO 221-IG010** is a gas-rich spiral galaxy in group of galaxies with $\log(L_{IR}/L_{\odot}$=11.17) at D_L∼42.8 Mpc. It is nearly a major axis observation where the slit position at (PA=150°), see A.85. NaD absorption line is weak compared to Hα, that is why it is short compared to Hα, see rotation curve 3.4.10. There is a rotation of Hα and NaD offset by 129.8 km s^{-1}, see rotation curve 3.4.10. And its V_{max} reaches up to 94.7 km s^{-1}.

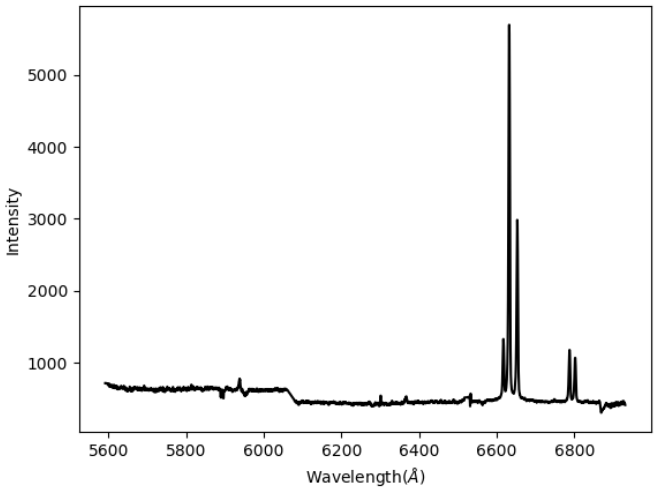

Figure A.83: integrated spectra of ESO 221-IG010

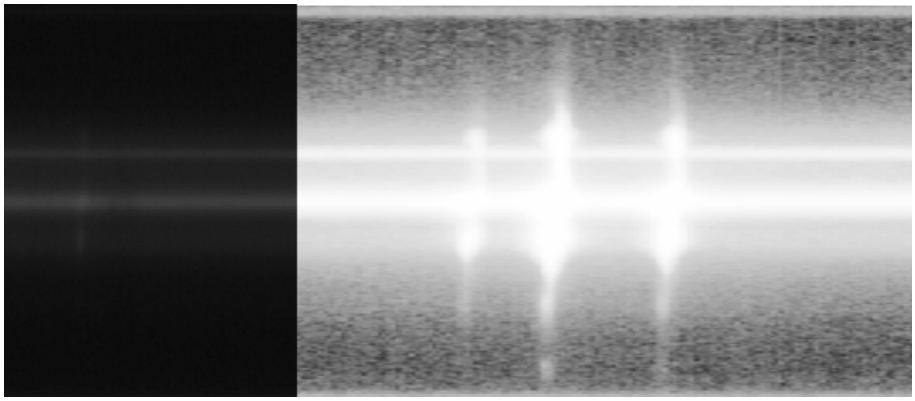

Figure A.84: 2D spectra of ESO 221-IG010

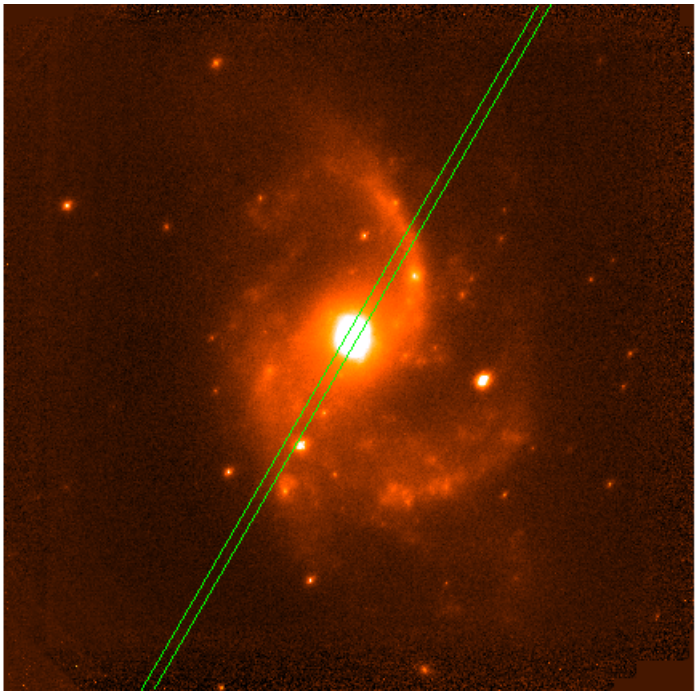

Figure A.85: ESO221-IG010[PA=150]

- **NGC6000** is nearly an edge-on starburst galaxy which has IR luminosity $\log(L_{IR}/L_{\odot}$=10.97) at D_L∼30 Mpc. The slit is aligned along the major axis at (PA=174°) as shown on A.88. Here broad NaD profile is seen. The rotation curve shows Na following Hα with an offset 141 km s^{-1} and maximum velocity of Hα is 200.8 km s^{-1}, see rotation curve 3.4.18.

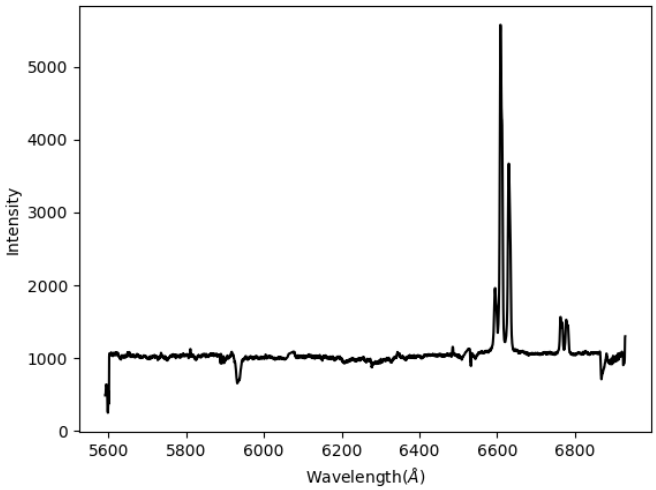

Figure A.86: integrated spectra of NGC6000

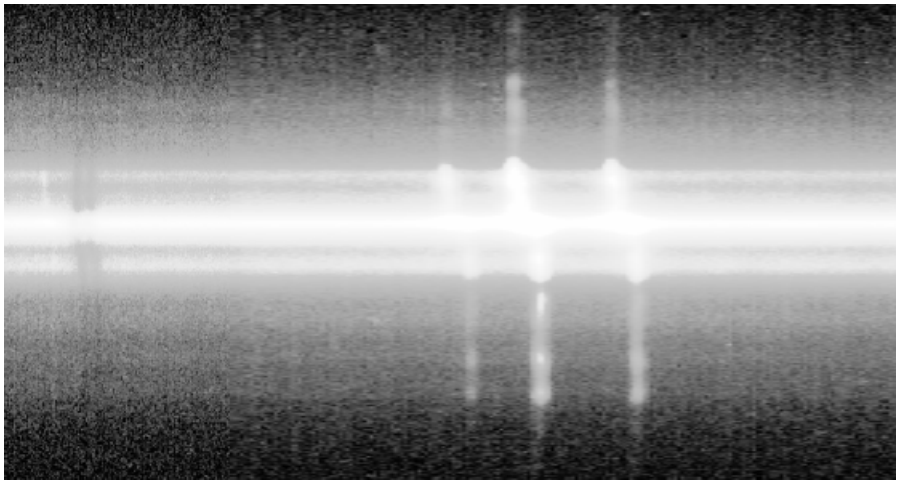

Figure A.87: 2D spectra of NGC6000

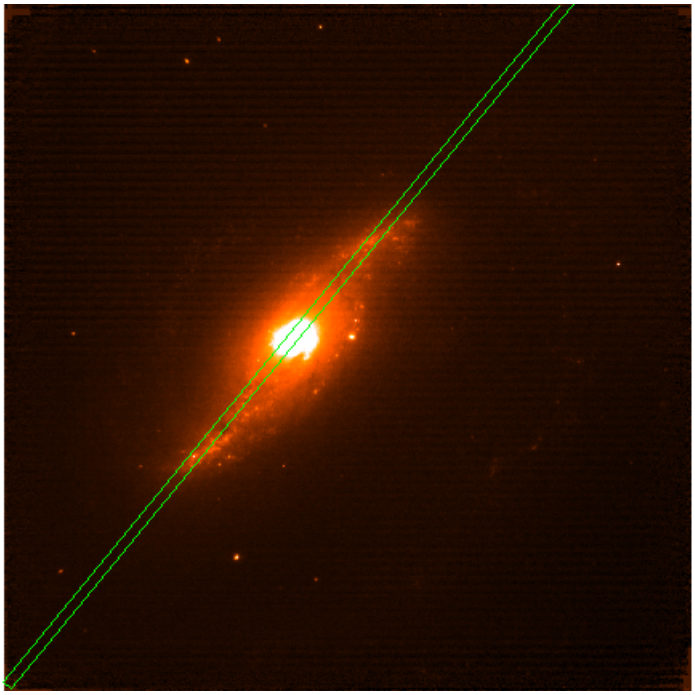

Figure A.88: NGC6000[PA=174]

- **ESO428-G023** is a spiral galaxy with a major axis observation where the slit aligned at (PA=261°), see A.91. The NaD co rotate with Hα with an offset velocity 155 km s^{-1} and H_α also offset from thecurve center by 25 km s^{-1}, see rotation curve 3.4.7. Here the origin of the outflowing gas which in this case coming from the disk is seen. The V_{max} of Hα relative to V_{sys} is $\sim$167 km s^{-1}.

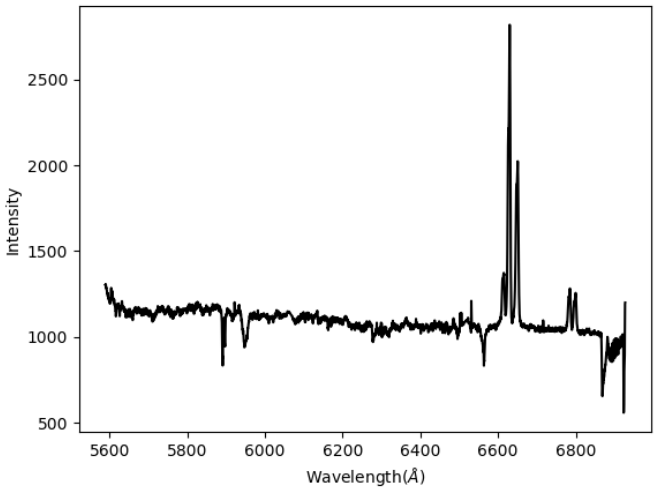

Figure A.89: integrated spectra of ESO428-G023

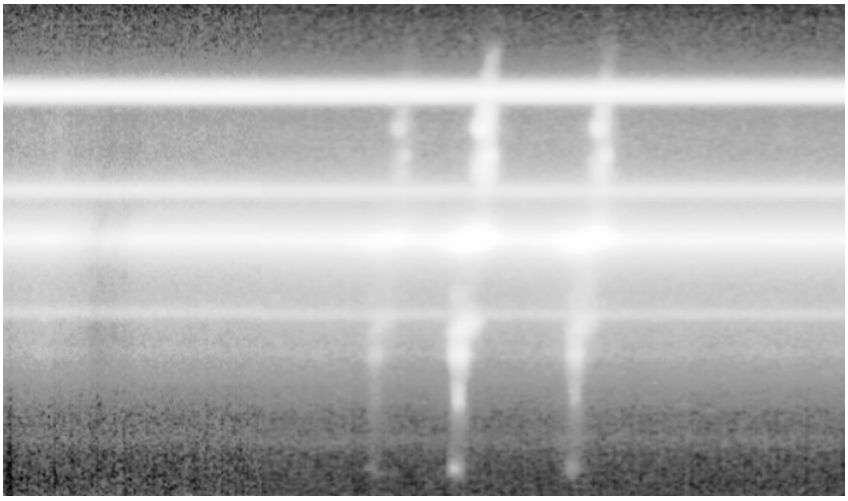

Figure A.90: 2D spectra of ESO428-G023

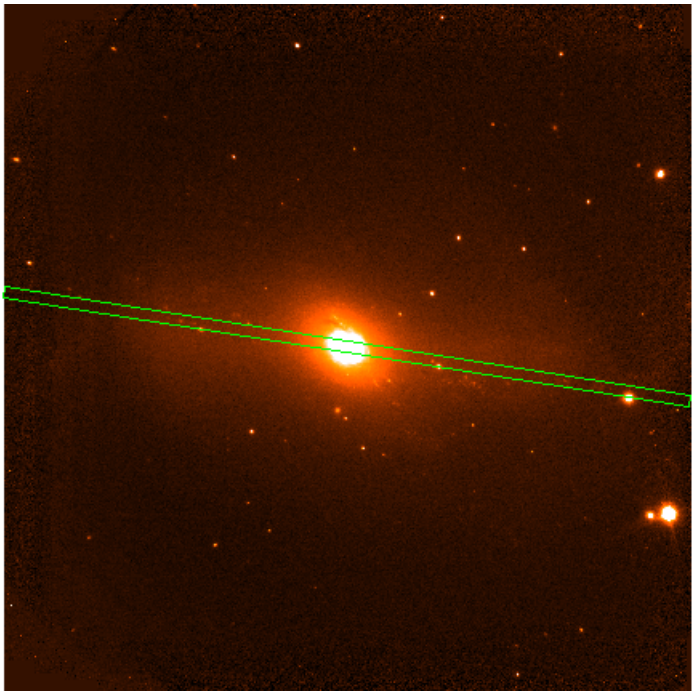

Figure A.91: ESO428-G023[PA=261]

- **IRASF06076-2139** is nearly an edge on starburst galaxy with $\log(L_{IR}/L_{\odot}$=11.6) at D_L∼158.2 Mpc. The slit positioned along the minor axis at (PA=61°), see A.94. It has a weak and short NaD line is Hα (as checked from 2D spectra as well as from the profile fitting). It has offset of NaD 166.8 km s^{-1} and has Hα offset 25 km s^{-1} from the systemic velocity. The maximum Hα velocity reaches up to 264 km s^{-1}, see the rotation curve 3.4.27.

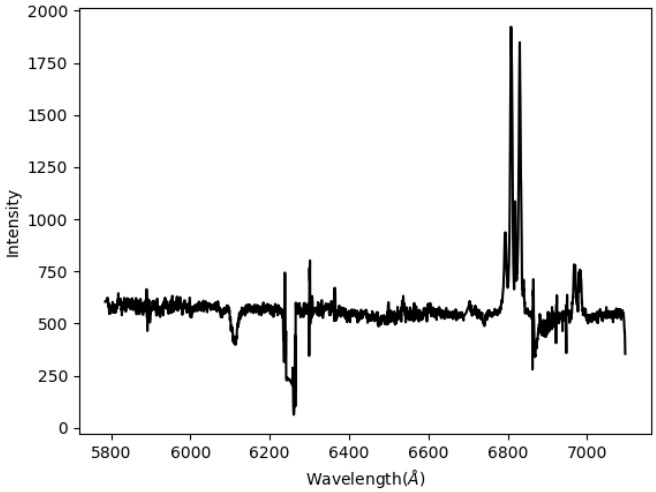

Figure A.92: integrated spectra of IRASF06076-2139

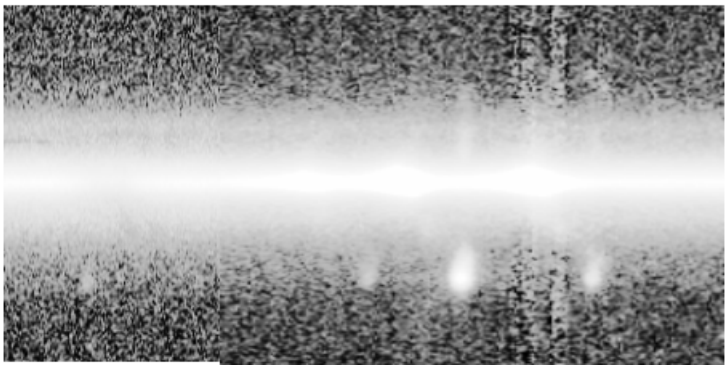

Figure A.93: 2D spectra of IRASF06076-2139

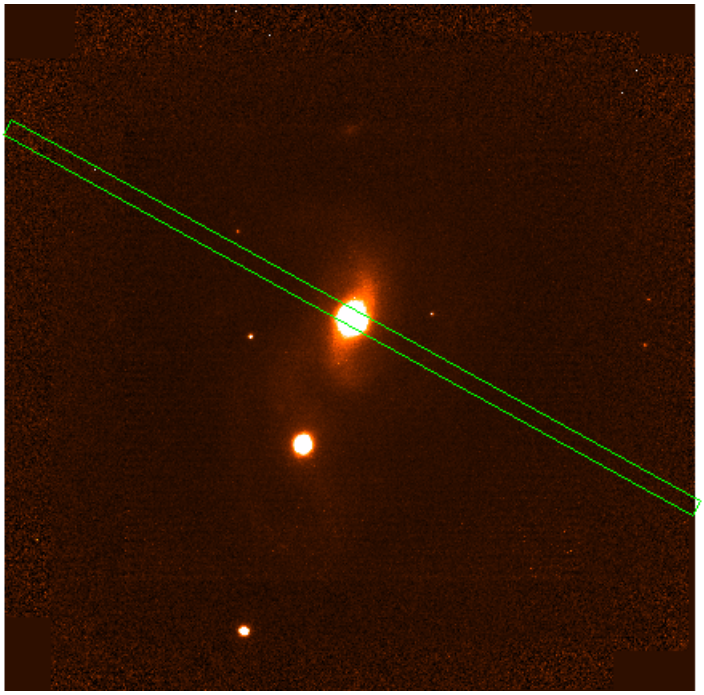

Figure A.94: IRASF06076-2139[PA=61]

- **ESO264-G036** is an edge on starburst galaxy that has IR luminosity of $\log(L_{IR}/L_{\odot}$=11.4) at D_L∼85 Mpc. The slit was aligned along the major axis at an angle (PA=294°), see A.97. The offset velocity of NaD from Hα is 172 km s^{-1} and Hα also offset from the center by -12 km s^{-1}, rotation curve 3.4.17. The V_{max} of Hα is 263.6 km s^{-1}.

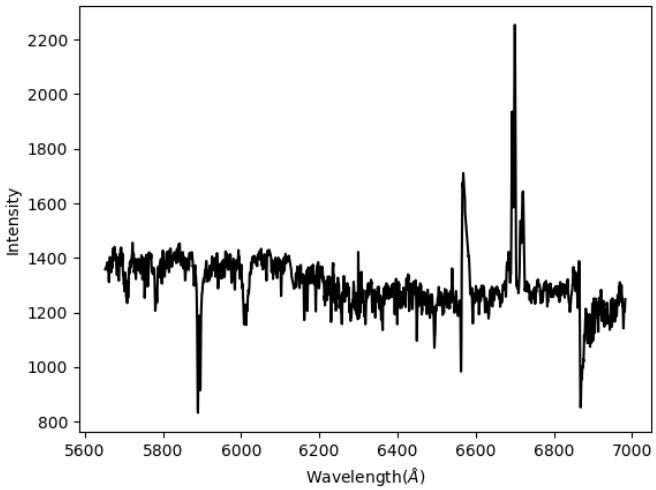

Figure A.95: integrated spectra of ESO264-G036

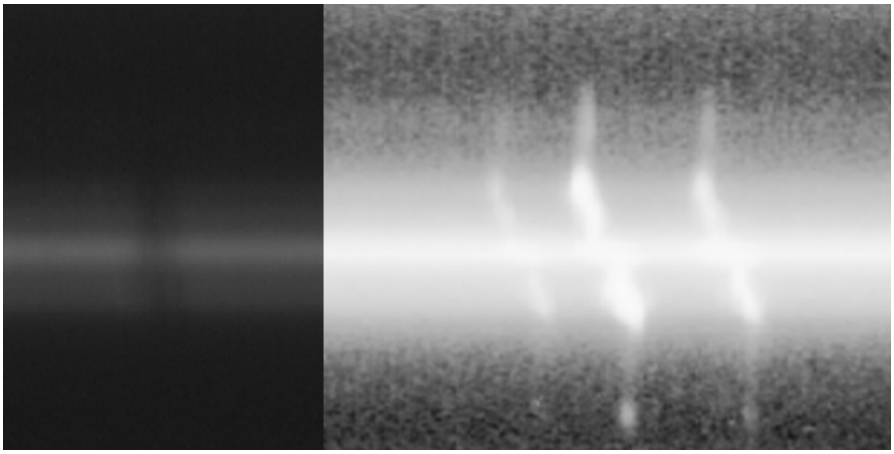

Figure A.96: 2D spectra of ESO264-G036

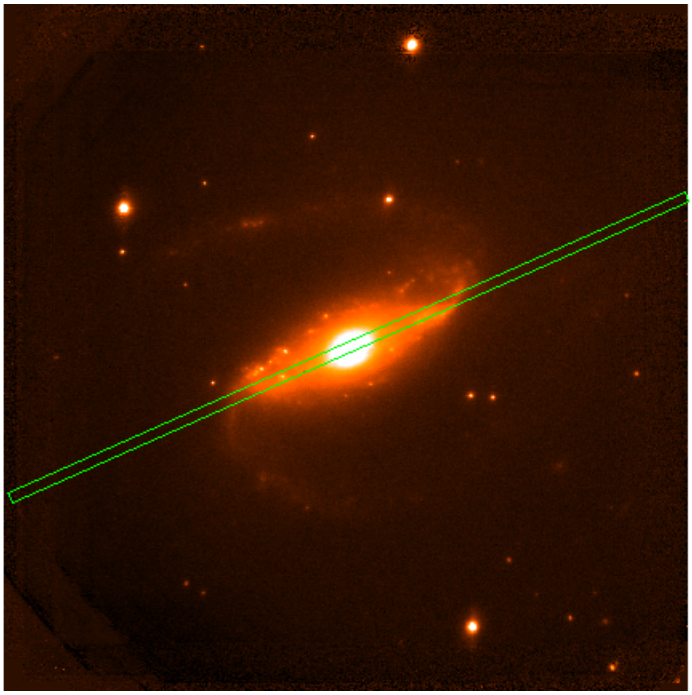

Figure A.97: ESO264-G036[PA=294]

- **ESO319-G022** is a starburst galaxy with IR luminosities $\log(L_{IR}/L_{\odot}=11)$ at $D_L \sim 68$ Mpc. It is a minor axis observation where the slit aligned at (PA=295°), see A.100. NaD is seen offset from Hα by about 186kms^{-1}, thus it can be conclude that this galaxy has a lot of outflowing material mainly from the central region, see rotation curve 3.4.24. I used the nearest value for the offset of Hα from the nuclear region. The V_{max} of Hα is 25 km s^{-1}.

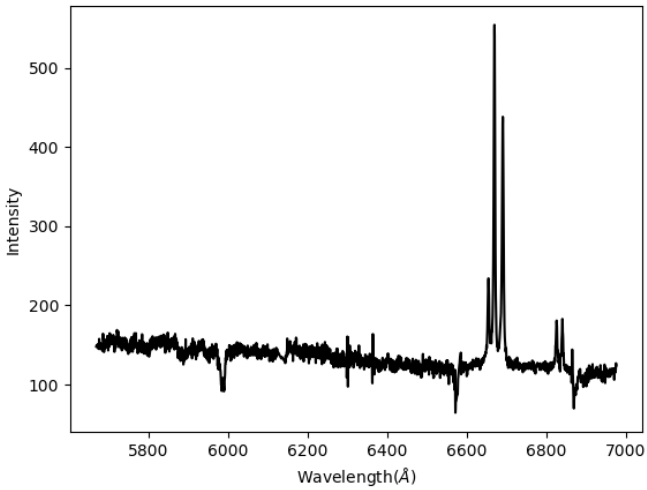

Figure A.98: integrated spectra of ESO319-G022

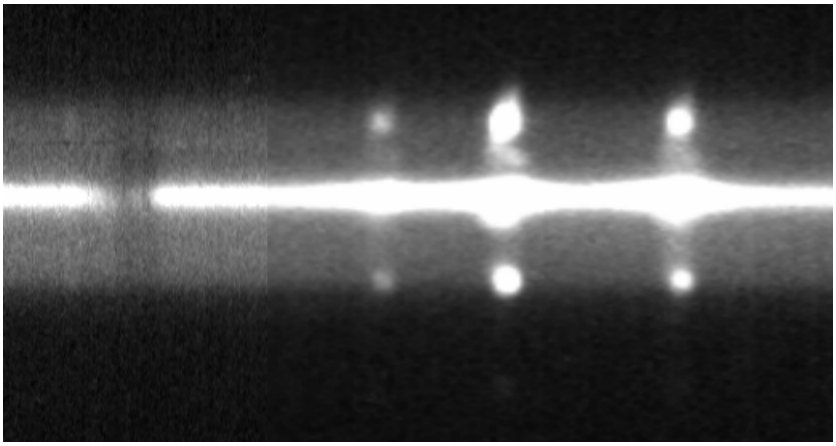

Figure A.99: 2D spectra of ESO319-G022

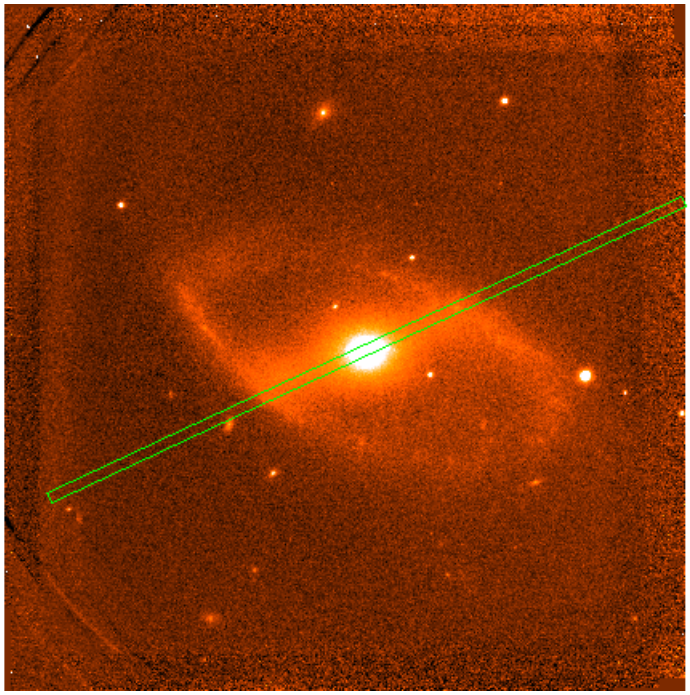

Figure A.100: ESO319-G022[PA=295]

- **IRAS12116-5615** is a face on starburst galaxy with IR luminosity $\log(L_{IR}/L_{\odot}=11.6)$ at $D_L\sim114$ Mpc. Due to the short continuum both Hα and Na D lines are short. NaD is highly blue shifted from Hα by 210 km s^{-1} which is an indicator of strong outflowing gas, see the rotation curve 3.4.7. The slit is positioned at (PA=231°), see A.103. The rotation shape of NaD is opposite to Hα which might indicate the origin of the outflow is from the nuclear region.

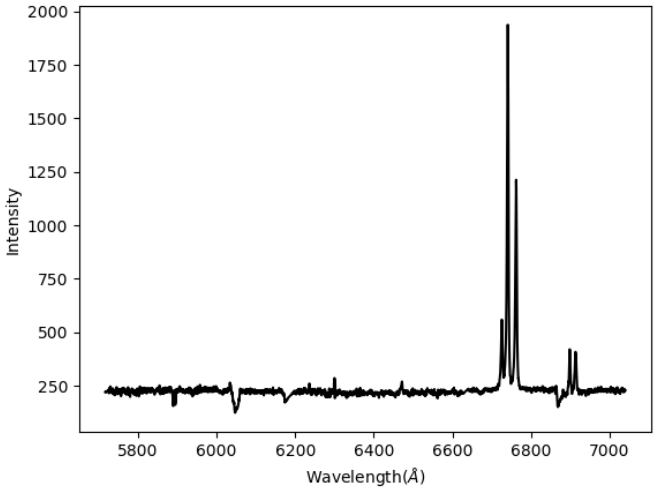

Figure A.101: integrated spectra of IRAS12116-5615

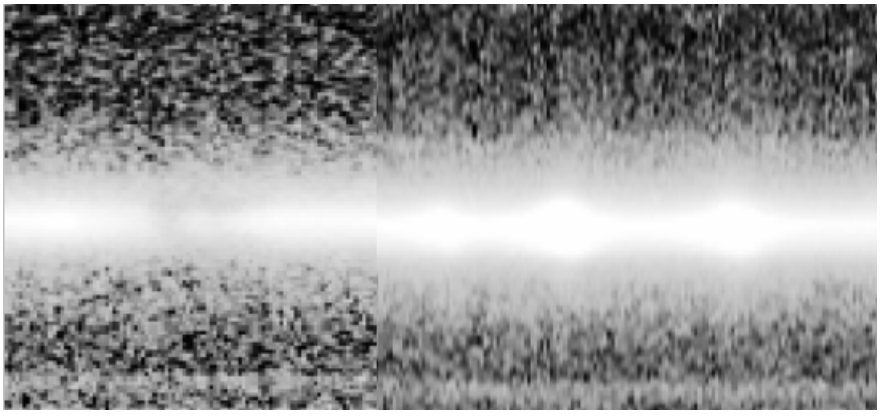

Figure A.102: 2D spectra of IRAS12116-5615

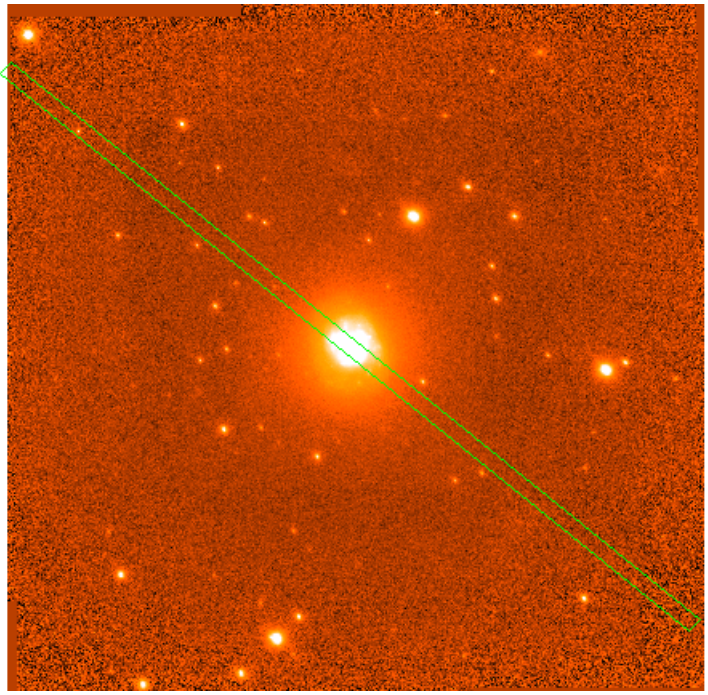

Figure A.103: IRAS12116-5615[PA=231]

- **NGC6240** is a famous well-studied Syfert2 galaxy Veilleux et al. (1995). It has an IR luminosity $\log(L_{IR}/L_{\odot}=11.9)$ at $D_L\sim$99 Mpc. The slits was aligned at (PA=45°) and at (PA=90°), see A.108. For both cases there is no clear shape of rotation curve, see the curve 3.4.3 and 3.4.20. The galaxy has a very broad emission and absorption lines and the domination of [N II]λ6583 line over Hα is seen which is be due to shock. As Hα starts to disappear [N II]λ6583 becomes dominant. The offset velocity shown at (PA=45°) is the biggest in our sample which is 380 km s^{-1} and at (PA=90°) has offset velocity of 192 km s^{-1}. To estimate offset of Hα for (PA=90°) observation, the nearest value was used since there are no NaD data points extend along Hα.

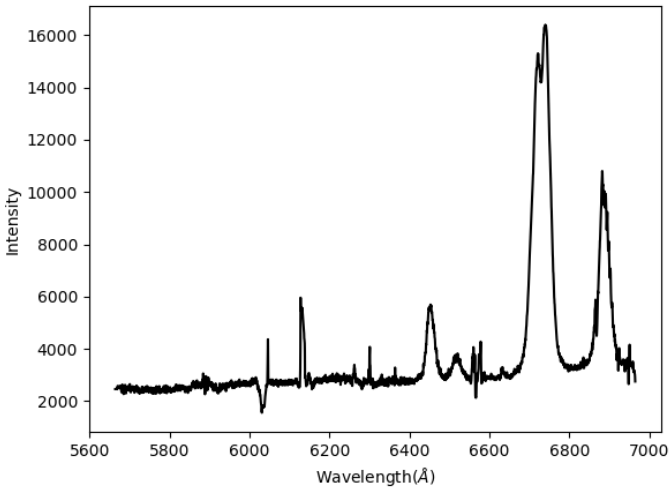

Figure A.104: integrated spectra of NGC6240[PA=90]

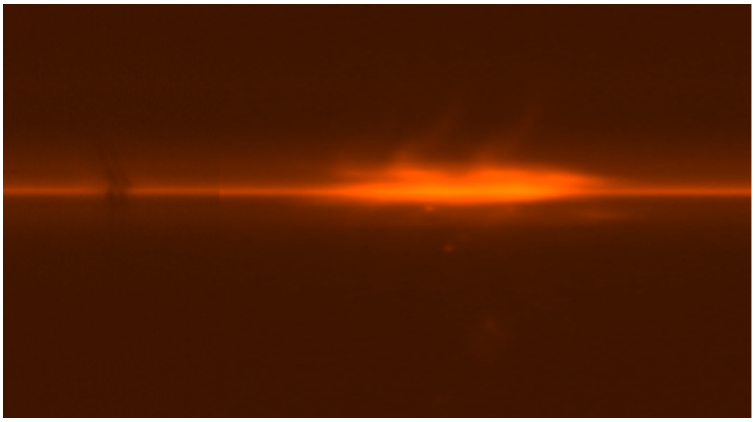

Figure A.105: 2D spectra of NGC6240[PA=90]

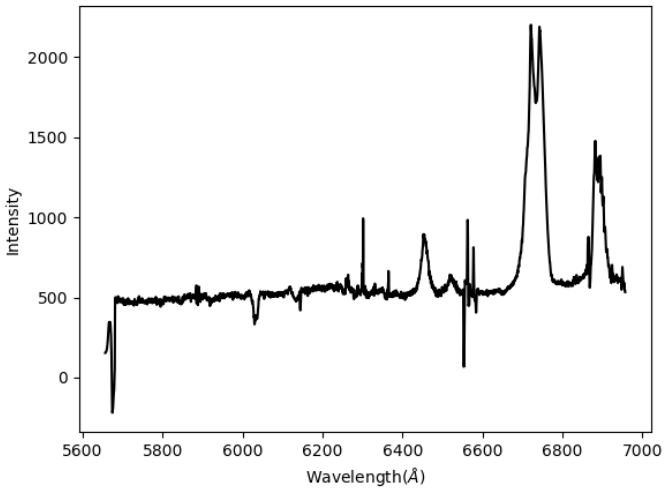

Figure A.106: integrated spectra of NGC6240[PA=45]

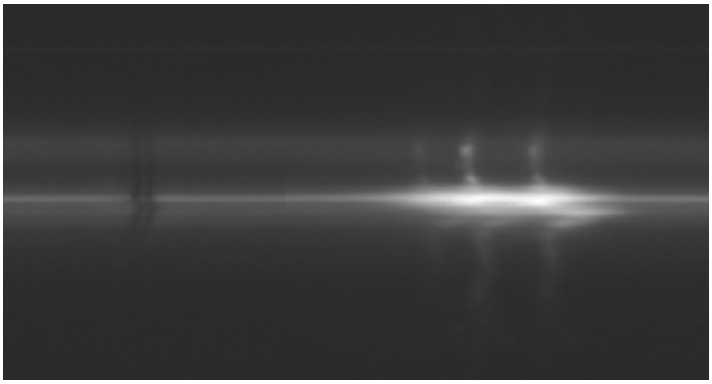

Figure A.107: 2D spectra of NGC6240[PA=45]

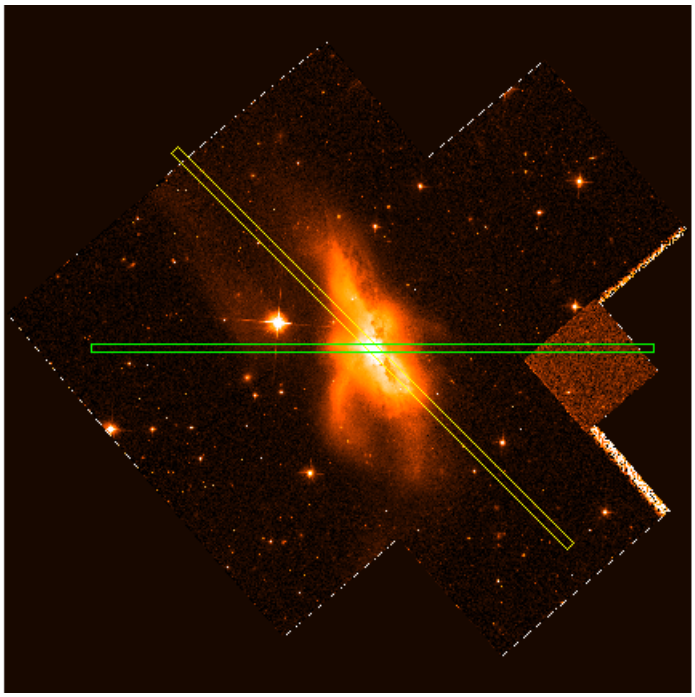

Figure A.108: NGC6240[PA=90](green) and NGC6240[45](yellow)

Bibliography

Agertz, O. and Kravtsov, A. V. (2015). On the Interplay between Star Formation and Feedback in Galaxy Formation Simulations. ApJ, 804:18.

Alonso-Herrero, A., Rieke, G. H., Rieke, M. J., Colina, L., Pérez-González, P. G., and Ryder, S. D. (2006). Near-Infrared and Star-forming Properties of Local Luminous Infrared Galaxies. ApJ, 650:835–849.

Arribas, S., Colina, L., Bellocchi, E., Maiolino, R., and Villar-Martín, M. (2014). Ionized gas outflows and global kinematics of low-z luminous star-forming galaxies. A&A, 568:A14.

Bennett, C. L., Larson, D., Weiland, J. L., and Hinshaw, G. (2014). The 1% Concordance Hubble Constant. ApJ, 794:135.

Booth, C. M. and Schaye, J. (2013). The interaction between feedback from active galactic nuclei and supernovae. *Sci. Rep.*, page 1738.

Croston, J. H., Hardcastle, M. J., Kharb, P., Kraft, R. P., and Hota, A. (2008). Chandra Evidence for AGN Feedback in the Spiral Galaxy NGC 6764. ApJ, 688:190–197.

Fabian, A. C. (2012). Observational Evidence of Active Galactic Nuclei Feedback. ARA&A, 50:455–489.

Gao, Y. and Solomon, P. M. (2004). The Star Formation Rate and Dense Molecular Gas in Galaxies. ApJ, 606:271–290.

Heckman, T. (2000). *Starburst Galaxies*.

Heckman, T. M. and Thompson, T. A. (2017). A Brief Review of Galactic Winds. *ArXiv e-prints*.

Hopkins, P., Kereš, D., Murray, N., Quataert, E., and Hernquist, L. (2012). Stellar feedback and bulge formation in clumpy discs. *mnras*, 427:968–978.

Hubble, E. P. (1926). Extragalactic nebulae. ApJ, 64.

Ishibashi, W. and Fabian, A. C. (2012). Active galactic nucleus feedback and triggering of star formation in galaxies. MNRAS, 427:2998–3005.

Kankare, E., Mattila, S., Ryder, S., Väisänen, P., Alberdi, A., Alonso-Herrero, A., Colina, L., Efstathiou, A., Kotilainen, J., Melinder, J., Pérez-Torres, M.-A., Romero-Cañizales, C., and Takalo, A. (2012). Discovery of Two Supernovae in the Nuclear Regions of the Luminous Infrared Galaxy IC 883. ApJ, 744:L19.

Kennicutt, Jr., R. C. (1998). Star Formation in Galaxies Along the Hubble Sequence. ARA&A, 36:189–232.

Kimm, T. and Cen, R. (2014). Escape Fraction of Ionizing Photons during Reionization: Effects due to Supernova Feedback and Runaway OB Stars. ApJ, 788:121.

Larsen, S. S. (2010). Young and intermediate-age massive star clusters. *Philosophical Transactions of the Royal Society of London Series A*, 368:867–887.

Lehnert, M. D. (1999). Superwinds and the nature of starburst galaxies. In van der Hucht, K. A., Koenigsberger, G., and Eenens, P. R. J., editors, *Wolf-Rayet Phenomena in Massive Stars and Starburst Galaxies*, volume 193 of *IAU Symposium*, page 645.

Lonsdale, C. J., Persson, S. E., and Matthews, K. (1984). Infrared observations of interacting/merging galaxies. ApJ, 287:95–107.

Martin, C. L. (2003). Properties of Galactic Winds and Their Impact on the IGM. In Rosenberg, J. L. and Putman, M. E., editors, *The IGM/Galaxy Connection. The Distribution of Baryons at z=0*, volume 281 of *Astrophysics and Space Science Library*, page 205.

Martin, C. L. (2005). Mapping Large-Scale Gaseous Outflows in Ultraluminous Galaxies with Keck II ESI Spectra: Variations in Outflow Velocity with Galactic Mass. ApJ, 621:227–245.

Mas-Hesse, J. M., Otí-Floranes, H., and Cerviño, M. (2008). Soft X-ray to far infrared luminosities ratio in star-forming galaxies: predictions from synthesis models. A&A, 483:71–78.

McCarthy, I. G., Schaye, J., Ponman, T. J., Bower, R. G., Booth, C. M., Dalla Vecchia, C., Crain, R. A., Springel, V., Theuns, T., and Wiersma, R. P. C. (2010). The case for AGN feedback in galaxy groups. MNRAS, 406:822–839.

Neugebauer, G., Habing, H. J., van Duinen, R., Aumann, H. H., Baud, B., Beichman, C. A., Beintema, D. A., Boggess, N., Clegg, P. E., de Jong, T., Emerson, J. P., Gautier, T. N., Gillett, F. C., Harris, S., Hauser, M. G., Houck, J. R., Jennings, R. E., Low, F. J., Marsden, P. L., Miley, G., Olnon, F. M., Pottasch, S. R., Raimond, E., Rowan-Robinson, M., Soifer,

B. T., Walker, R. G., Wesselius, P. R., and Young, E. (1984). The Infrared Astronomical Satellite (IRAS) mission. ApJ, 278:L1–L6.

Pizagno, J., Vavilkin, T., Evans, A., Mazzarella, J., Howell, J., Armus, L., Surace, J., Chan, B., and Barnes, J. (2008). Morphology of Luminous Infrared Galaxies. In Funes, J. G. and Corsini, E. M., editors, *Formation and Evolution of Galaxy Disks*, volume 396 of *Astronomical Society of the Pacific Conference Series*, page 247.

Randriamanakoto, Z., Escala, A., Väisänen, P., Kankare, E., Kotilainen, J., Mattila, S., and Ryder, S. (2013). Near-infrared Adaptive Optics Imaging of Infrared Luminous Galaxies: The Brightest Cluster Magnitude-Star Formation Rate Relation. ApJ, 775:L38.

Rupke, D. S. and Veilleux, S. (2005). Keck High-Resolution Spectroscopy of Outflows in Infrared-luminous Galaxies. ApJ, 631:L37–L40.

Rupke, D. S., Veilleux, S., and Sanders, D. B. (2002). Keck Absorption-Line Spectroscopy of Galactic Winds in Ultraluminous Infrared Galaxies. ApJ, 570:588–609.

Sanders, D. and Ishida, C. (2004). Luminous Infrared Galaxies: Optical Morphology and Photometry, Molecular Gas Masses, and Starburst/AGN Activity versus Infrared Luminosity. In Aalto, S., Huttemeister, S., and Pedlar, A., editors, *The Neutral ISM in Starburst Galaxies*, volume 320 of *Astronomical Society of the Pacific Conference Series*, page 230.

Sanders, D. B., Kartaltepe, J. S., Kewley, L. J., U, V., Yuan, T., Evans, A. S., Armus, L., and Mazzarella, J. M. (2009). Luminous Infrared Galaxies and the "Starburst-AGN Connection". In Wang, W., Yang, Z., Luo, Z., and Chen, Z., editors, *The Starburst-AGN Connection*, volume 408 of *Astronomical Society of the Pacific Conference Series*, page 3.

Sanders, D. B., Mazzarella, J. M., Kim, D.-C., Surace, J. A., and Soifer, B. T. (2003). The IRAS Revised Bright Galaxy Sample. AJ, 126:1607–1664.

Sanders, D. B. and Mirabel, I. F. (1996). Luminous Infrared Galaxies. ARA&A, 34:749.

Santini, P., Maiolino, R., Magnelli, B., Lutz, D., Lamastra, A., Li Causi, G., Eales, S., Andreani, P., Berta, S., Buat, V., Cooray, A., Cresci, G., Daddi, E., Farrah, D., Fontana, A., Franceschini, A., Genzel, R., Granato, G., Grazian, A., Le Floc'h, E., Magdis, G., Magliocchetti, M., Mannucci, F., Menci, N., Nordon, R., Oliver, S., Popesso, P., Pozzi, F., Riguccini, L., Rodighiero, G., Rosario, D. J., Salvato, M., Scott, D., Silva, L., Tacconi, L., Viero, M., Wang, L., Wuyts, S., and Xu, K. (2014). The evolution of the dust and gas content in galaxies. A&A, 562:A30.

Schechter, P. (1976). An analytic expression for the luminosity function for galaxies. *apj*, 203:297–306.

Schnorr-Müller, A., Storchi-Bergmann, T., Nagar, N., Robinson, A., Lena, D., Riffel, R., and Couto, G. (2014). Feeding and feedback in the inner kiloparsec of the active galaxy NGC 2110. *MNRAS*, 437:1708–1724.

Soifer, B. T., Neugebauer, G., and Houck, J. R. (1987). The IRAS view of the extragalactic sky. ARA&A, 25:187–230.

Sugahara, Y., Ouchi, M., Lin, L., Martin, C. L., Ono, Y., Harikane, Y., Shibuya, T., and Yan, R. (2017). Evolution of Galactic Outflows at z\sim 0{–}2 Revealed with SDSS, DEEP2, and Keck Spectra. ApJ, 850:51.

Väisänen, P., Mattila, S., Kniazev, A., Adamo, A., Efstathiou, A., Farrah, D., Johansson, P. H., Östlin, G., Buckley, D. A. H., Burgh, E. B., Crause, L., Hashimoto, Y., Lira, P., Loaring, N., Nordsieck, K., Romero-Colmenero, E., Ryder, S., Still, M., and Zijlstra, A. (2008a). Adaptive optics imaging and optical spectroscopy of a multiple merger in a luminous infrared galaxy. MNRAS, 384:886–906.

Väisänen, P., Randriamanakoto, Z., Escala, A., Kankare, E., Kniazev, A., Kotilainen, J. K., Mattila, S., Ramphul, R., Ryder, S., and Tekola, A. (2014). Super Star Clusters in Luminous Infrared Galaxies: the SUNBIRD Survey. In *Massive Young Star Clusters Near and Far: From the Milky Way to Reionization*, pages 185–189.

Väisänen, P., Ryder, S., Mattila, S., and Kotilainen, J. (2008b). A Pair of Leading Spiral Arms in a Luminous Infrared Galaxy? ApJ, 689:L37.

Van Eymeren, J., Koribalski, B. S., López-Sánchez, Á. R., Dettmar, R. J., and Bomans, D. J. (2010). A kinematic study of the neutral and ionized gas in the irregular dwarf galaxies IC 4662 and NGC 5408. *Mon. Not. R. Astron. Soc.*, 407(1):113–132.

Veilleux, S., Cecil, G., and Bland-Hawthorn, J. (2005). Galactic Winds. ARA&A, 43:769–826.

Veilleux, S., Kim, D.-C., Sanders, D. B., Mazzarella, J. M., and Soifer, B. T. (1995). Optical Spectroscopy of Luminous Infrared Galaxies. II. Analysis of the Nuclear and Long-Slit Data. ApJS, 98:171.

Wang, J. L., Xia, X. Y., Mao, S., Cao, C., Wu, H., and Deng, Z. G. (2006). Luminous Infrared Galaxies in the Local Universe. ApJ, 649:722–729.

Weedman et al., F. (1981). NGC 7714 - The prototype star-burst galactic nucleus. *Apj*, 248:105–112.

Zubovas, K. and King, A. R. (2014). Galaxy-wide outflows: cold gas and star formation at high speeds. MNRAS, 439:400–406.